Ph.D. thesis

Development of intense beam of ultracold antiprotons

大強度極低温反陽子ビームの開発

Thesis Adviser : Prof. YAMAZAKI Yasunori

Student ID : 77901

ICHIOKA Toshiyasu

September 27, 2000

Contents

Overview

The objective of the work reported here is to produce intense beam of ultracold antiprotons. It is known that antiprotons can be cooled in Penning traps using electron cooling technique. Our scheme is to capture antiprotons into a trap and to cool them by this technique, then to extract cooled antiprotons as a monoenergetic beam for collision and spectroscopy experiments. When a collection of charged particle is cooled, it behaves as a nonneutral plasma. Thus for the realization of ultracold antiprotons, considerations from nonneutral plasma physics side were essential. The construction of this thesis is as follows:

The first chapter is dedicated to historical backgrounds, the first section (Sec.1.1) for antiproton physics and the following Sec.1.2 for nonneutral plasmas. Chapter 2 describes the project in which this work is involved (ASACUSA project). After the introduction to AD, the machine which produces antiprotons, a scheme to produce slower antiprotons is presented. Then, it follows a description of particle clouds in electric+magnetic field (Chapter 3). When the Debye length of a cloud consists of cold charged particles becomes smaller than the size of the electrodes, it can be treated as a nonneutral plasma. Based on the knowledge of particle traps and nonneutral plasmas, a trap was constructed for ASACUSA project. In Chapter 4, depicted are design criteria and system specifications of the ASACUSA antiproton trap. Then, Chapter 5 deals with experimental results. Reviews on measured properties of the ASACUSA trap are given. Future works and results of preparatory experiments etc. are summarized in the Appendices. Notations and useful formulae are also given there.

Chapter 1

Introduction

1.1 Historical background of physics with antiprotons

1.1.1 At the dawning

The story of our protagonist started in 1955 when Segrè and Chamberlain identified antiprotons among a number of mesons[1]. Earliest works are chiefly on antiparticle formation[2, 3] or on cross section measurements (annihilation cross section etc.)[4].

1.1.2 The LEAR era

The advent of Low Energy Antiproton Ring (LEAR)[1] opened a brand new era of antiprotonic experiments. Low energy antiprotons produced by four machines, *i.e.*, Proton Synchrotron(PS), Antiproton Cooler(AC), Antiproton Accumulator(AA), and LEAR were delivered as 200 nsec-pulsed or continuous beams. At first, it can be noted that all through the period the research on symmetry were active, like CP violation, T non-conservation, etc.[5].

PS196 collaboration pursued mass spectroscopy and finally achieved the precision of 9 parts in 10^{11} in the comparison of charge-to-mass ratio of an antiproton with that of a proton[6]. In the due course, they developed techniques of trapping[7] and electron cooling[8] of antiprotons in a Penning trap. In PS200 collaboration, initially aimed at the experiments of antimatter gravity, trial of capturing a number of antiprotons was successful[9, 10]. Extraction of cooled antiprotons was also tried[11].

A series of atomic collision experiments by PS194 collaboration which compares antiprotons and protons -*e.g.* ionization of atoms and molecules by proton and antiproton

[1] First $\overline{\mathrm{p}}$ was injected in 1982.

impact- revealed the significant disagreement between the theory and experiments, some of which still remain to be investigated[12, 13, 14]. Especially, it is remarkable that proton impact and antiproton impact lead to disagreement in ratios of double- to single-ionization cross sections in the relatively high energy region where the Born approximation is considered to be valid[15, 16, 17]. It was also at LEAR where an interesting state of wake riding electrons was studied (PS204 collaboration)[18].

The discovery that an antiproton captured by a helium atom can form a metastable state opened a new field in researches of few-body systems, precision laser spectroscopy, etc.(PS205 collaboration)[19]. The precision of the measurements of resonance lines in successive experiments became as high as can be used to determine fundamental constants[20]. To find a resonance with narrow band lasers, the accuracy of theoretical calculations were essential and in turn, supported by precise measurements with lasers, three-body calculations became much more reliable.

Antihydrogen, as the simplest antimatter has been quested. The first realization of antihydrogen by PS210 collaboration, though they were eleven and with high energy, added one more glory at the end of LEAR's life[21].

LEAR was shut down in December 1996 and is now used for heavy ion accumulation as a part of LHC project.

1.1.3 Inauguration of AD

Responding to the strong request from the user's community of LEAR, CERN took a step forward to modify AC into a new machine, that is what we now call the Antiproton Decelerator (AD). Details will be given in the next chapter.

1.2 Historical background of physics of nonneutral plasmas

The word "nonneutral plasma" designates a cloud of charged particles where there is not overall charge neutrality. However as in a neutral plasma, lots of plasma phenomena like collective oscillation modes, particle or heat transports are observed.

It was in the period from the late 60's to the early 70's when certain amount of attention was paid in such systems. Early works were on the microwave devices like magnetrons or vacuum tube diodes, etc. Practical interests on charged particle beams were the main motivation. There also existed interests in trapping a number of electrons for the construction of charged particle accelerators[22].

Around 1970 thermal equilibria of trapped nonneutral plasmas were examined and it was shown that a nonneutral plasma trapped in a Penning trap rotates as a rigid rotor

when it is in thermal equilibrium[23, 24]. Later, theoretical studies on electrostatic normal modes of nonneutral plasmas[25, 26] and experimental works on them[27] were elaborated in 90's.

Since the 80's, containment of charged particles became objectives and nonneutral plasmas consist of trapped electrons[28, 29], positrons[30, 31], and ions[32, 33] have been extensively studied. One-component electron plasmas, which we would regard as deuteragonist, were intensively studied at the University of California at San Diego (UCSD). It was found that, in the case of cylindrical electron plasmas, confinement time scales as $\left(\frac{B}{L}\right)^2$ where L is the length of the plasma and B is the magnetic field[34]. Similar, but also length-dependent lifetime scaling is also proposed[35]. After the theoretical elaboration of electrostatic modes, they were experimentally identified and used as diagnostics of plasmas[36, 37].

Also an impressive invention of a trap with large harmonic potential was done by Mohri at Kyoto University[38]. The feature of this type is that the multi-ring structure enables the flexible formation of trapping potentials. Even the correction for image charge effect is possible. These features of Multi-ring traps will be fully described in the Section 3.5.

Chapter 2

AD and ASACUSA project

2.1 The Antiproton Decelerator (AD)

Responding to the strong request from the user's community of LEAR, CERN took a step forward to modify AC into a new machine, that is what we now call the Antiproton Decelerator(AD). The location of AD is shown in Fig.2.1 together with other machines.

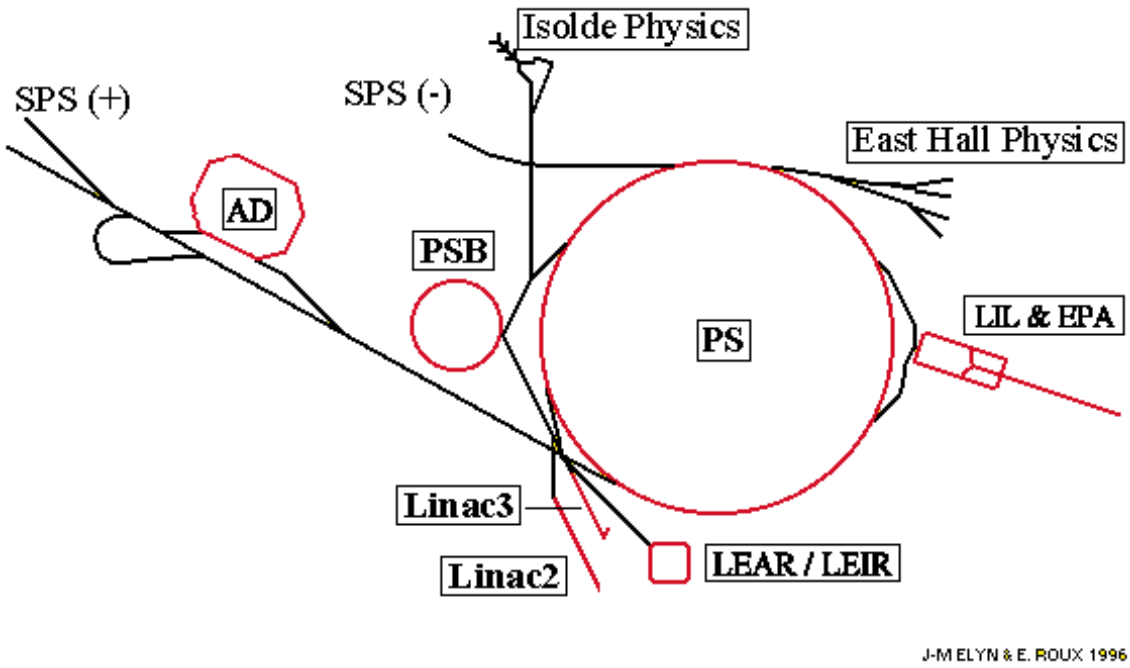

Figure 2.1: PS complex.

Let us here summarize how antiprotons are provided at AD. What is completely different from LEAR is that the whole procedure of collection,cooling and deceleration is

done within the same machine. For example, PS is only used for the proton injection into AD, while it was also used to decelerate antiprotons at LEAR. Below are the details[39].

1. A production beam of 26 GeV/c protons comes from PS. Typical number is 10^{13} per pulse.

2. The beam hits the copper target[1] and produced antiprotons are collected at 3.57 GeV/c. About 5×10^7 antiprotons are injected to AD, thus the production and collection efficiency is about 2×10^{-5}.

3. Since the PS bunch has a rather short width compared to its spacing, by rotating it in a phase plane longitudinal to the beam direction, the momentum spread can be made narrower. Namely, the bunch will be more monochromatic in momentum at the cost of extending in the circumference[40]. By applying this bunch rotation, momentum spread ($\frac{\Delta p}{p}$) of antiprotons are reduced from $\pm$ 3% to $\pm$ 1.5%.

4. Preparation for the deceleration : Stochastic cooling makes the emittance (initially 200π mm $\cdot$ mrad) to be 5π mm $\cdot$ mrad and $\frac{\Delta p}{p}$ to be 0.1%

5. Antiprotons are decelerated to 2 GeV/c.

6. They are further decelerated in several steps to 300MeV/c where electron cooling is available.

7. Deceleration to 100 MeV/c takes place and beams are ejected from the machine. Estimated overall deceleration efficiency is 25% and thus 1.2×10^7 antiprotons will be delivered. In contrast to LEAR, there will be no slow extraction mode.

[1] At LEAR, Ir target was used. In any cases, the production target should be compatible with the enormous heat load.

In Fig.2.2, these designed scheme of AD deceleration cycle is sketched with time scale[2].

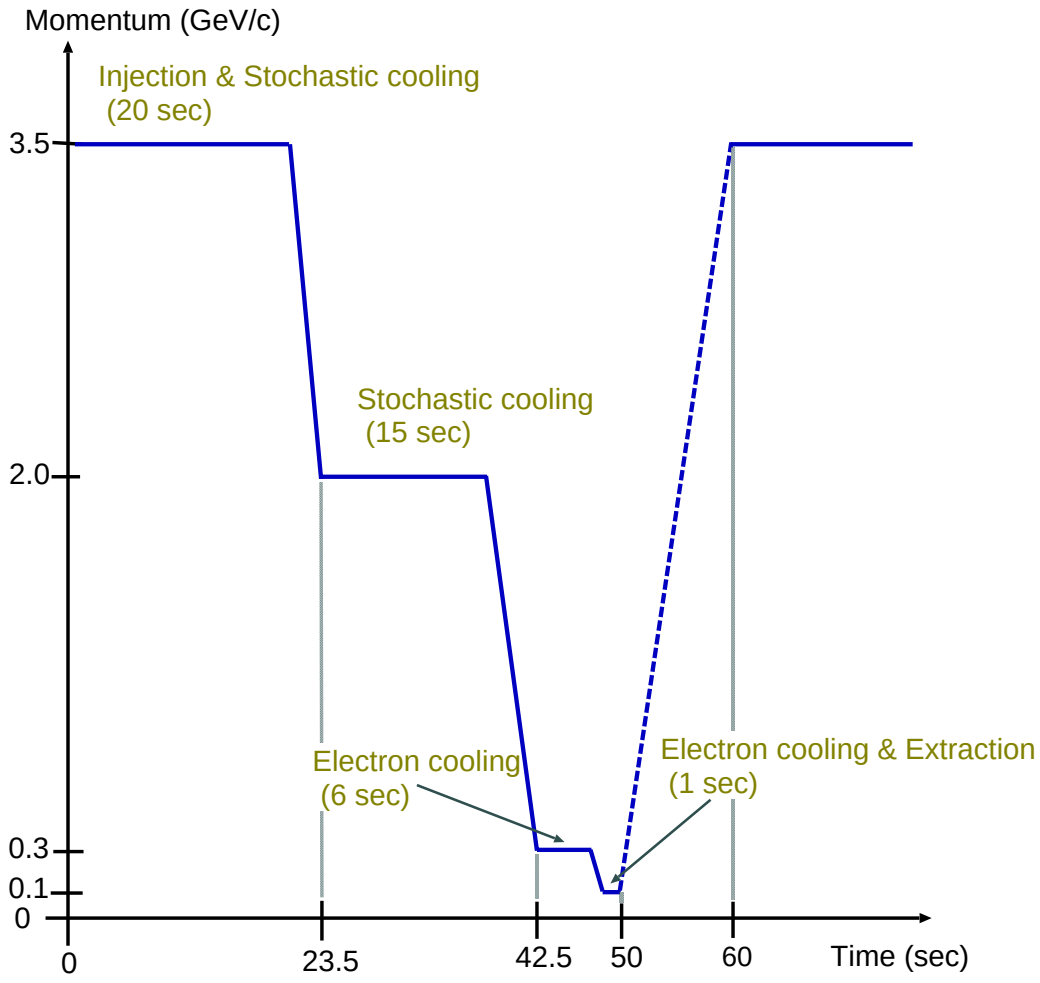

Figure 2.2: Basic deceleration scheme of AD.

[2]Stacking option inside the machine is also being considered.

Fig.2.3 shows the structure and experimental areas inside AD.

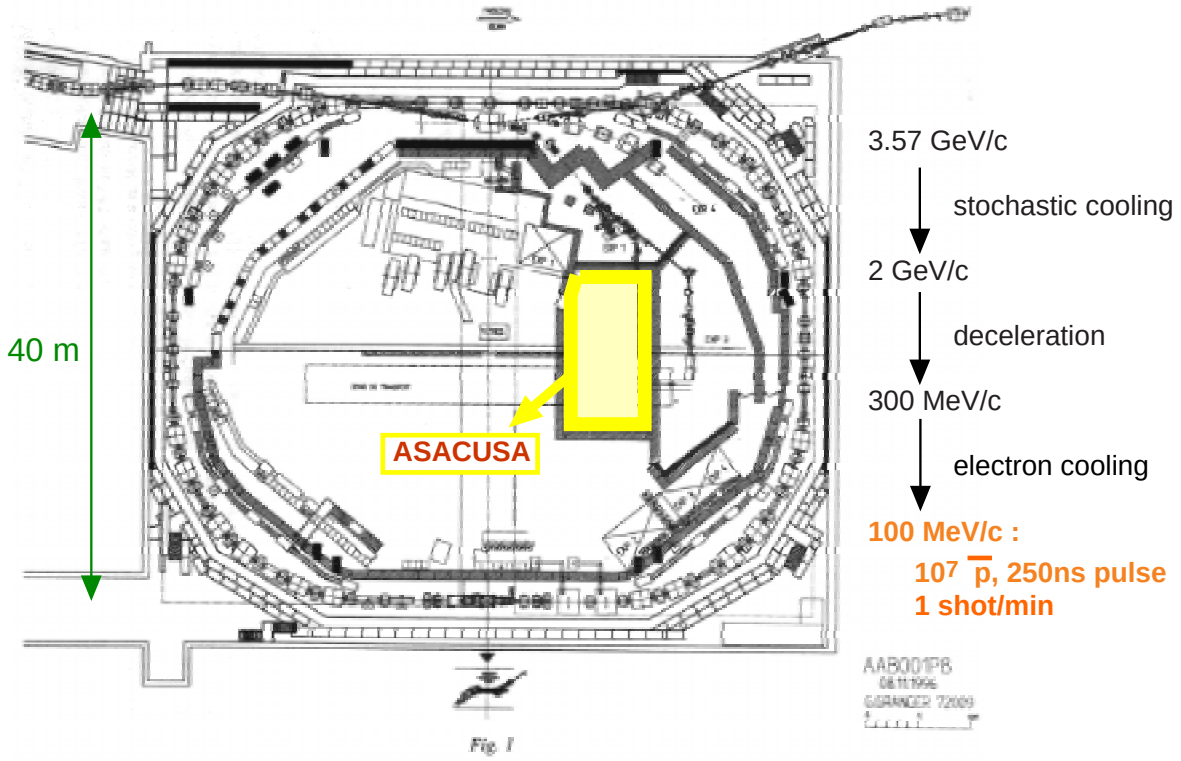

Figure 2.3: AD and hall layout. Correction of created antiprotons, cooling, and deceleration are performed in the same ring.

There are three experiments running at AD. All of them use traps located in superconducting solenoids.

ATHENA

Aiming at the spectroscopy of 1S-2S transition of antihydrogen with their AnTiHydrogEN Apparatus. Catching of energetic antiprotons, accumulation of positrons, recombination and spectroscopy will be done in an aggregation of three traps located in magnetic fields.

ATRAP

Antihydrogen TRAP Collaboration is aiming at trapping cold antihydrogen and trying to compare them with hydrogens.

The one in which this work is involved. Different from the others, various experiments which cover wide area in atomic physics are being performed. Detailed description will be given in the following section.

2.2 ASACUSA project - Physics motivation and experimental plans

Following the decision to construct AD, to have more complete, systematic knowledge on the atomic processes was desired and it stood a fair chance. A collaboration lead by Japanese researchers was formed to that effect. The name of the group **ASACUSA** is the abbreviation of "Atomic Spectroscopy And Collisions Using Slow Antiprotons", which most briefly describes the project. In the rest of this Chapter, an outline of the ASACUSA experiments is given. Details of the proposed experiments and physics goals can be found elsewhere[41, 42].

In ASACUSA project, experiments are planned to investigate initial processes of antiprotonic atom formation, interaction between antimatter and matter etc., most of which require ultra-low energy antiproton beams[41, 43, 42]. As can be seen from a review in the previous chapter, preparation of ultracold antiprotons which can be used as a beam requires the cooperation of particle physics, atomic physics, and plasma physics.

At AD, 10^7 antiprotons of 5.3 MeV will be at hand as a pulse of 250 ns with a repetition period of one minute[3]. In our scheme, we will let MeV-energy antiprotons pass through an RFQ, post decelerator. Reduced energy will be 10-120 keV. Then, those antiprotons enter a Multi-Ring Electrode(MRE) trap described in the later section. Electron cooling technique will be applied. Dense cloud of antiprotons, together with electrons, are supposed to behave as a nonneutral plasma. Techniques of nonneutral plasma physics will be applied to manipulate antiproton clouds. Extracted beam will be transported using electrostatic lenses and finally reaches the collision chamber. Expected beam energy lies in a range 10 eV - 1 keV. Energy change during these stages is schematically summarized in Fig.2.4.

To clarify the necessity of low energy antiprotons, let us consider a collision of antiprotons with atomic hydrogens. When an antiproton is captured in an atomic hydrogen, a resultant bound state $\overline{\mathrm{p}}\mathrm{p}$ is called protonium. Since the protonium is a Coulombic two-body system which is theoretically well understood, it is especially suitable for the research of initial capture process of antiprotons into matter. To perform this kind of experiment,

[3] As of August 2000, a bunch of 2×10^7 antiprotons per two minutes is delivered.

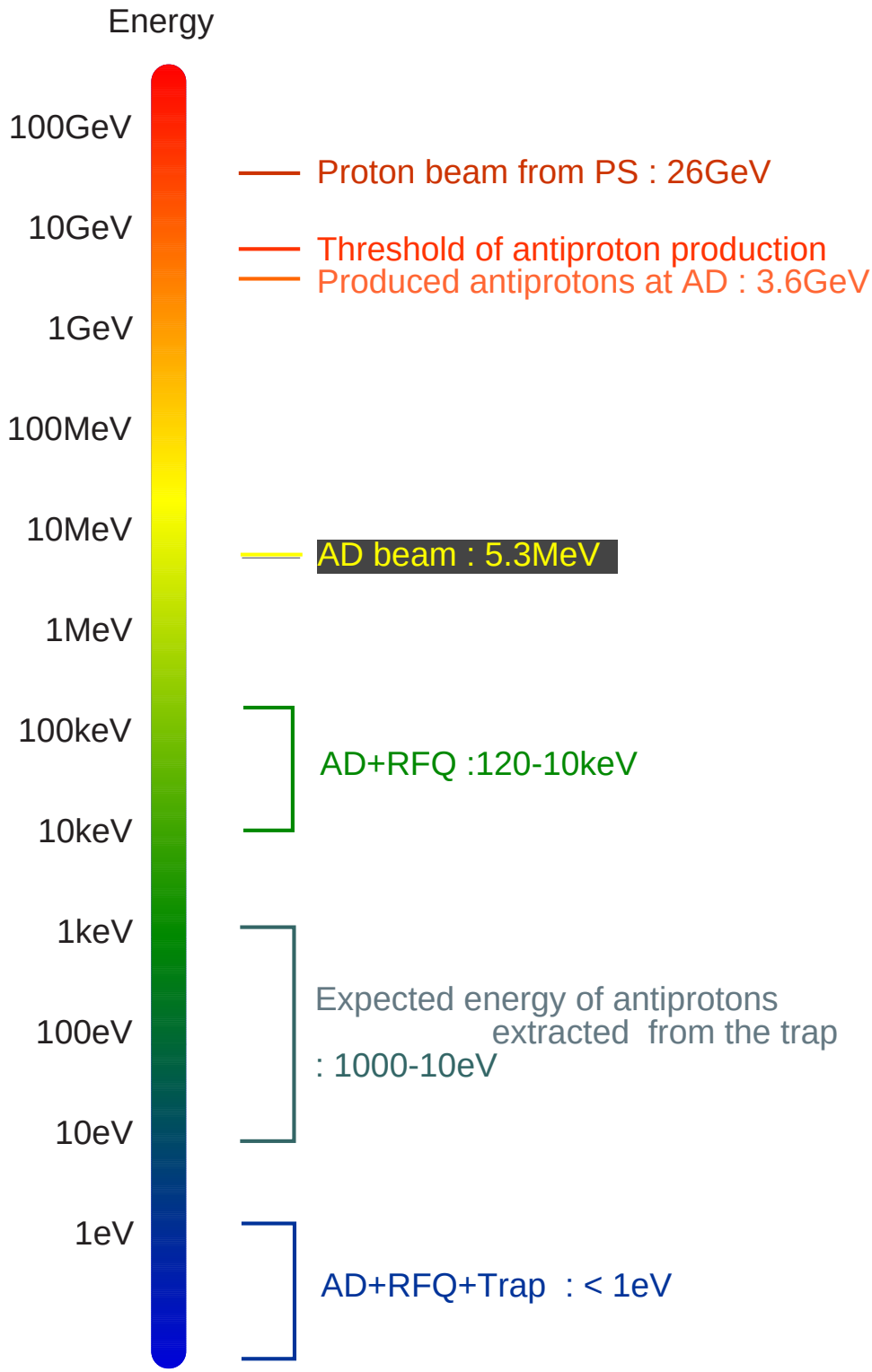

Figure 2.4: Energy scale illustrating the different steps used to slow down the antiprotons.

we need to collide antiprotons with gaseous target under the single collision condition. So far, experimental researches on exotic atoms[4] have been done only in dense media[44].

Unfortunately, to date there are only a few calculations of formation cross sections of $\overline{\mathrm{p}}$p[45]. Shown in Fig.2.5 are formation cross sections of $\overline{\mathrm{p}}$p vs. collision energy in the center of mass system, calculated by Classical Trajectory Monte Carlo (CTMC) method[46]. Two processes are shown : $\overline{\mathrm{p}} + \mathrm{H} \rightarrow \overline{\mathrm{p}}\mathrm{p} + \mathrm{e}^-$ and $\overline{\mathrm{p}} + \mathrm{H}_2 \rightarrow \overline{\mathrm{p}}\mathrm{p} + \mathrm{H} + \mathrm{e}^-$. In the case of $\overline{\mathrm{p}}$ on atomic hydrogen, since the outgoing electron should take care of the excess energy, cross section drops off rapidly at the ionization threshold.

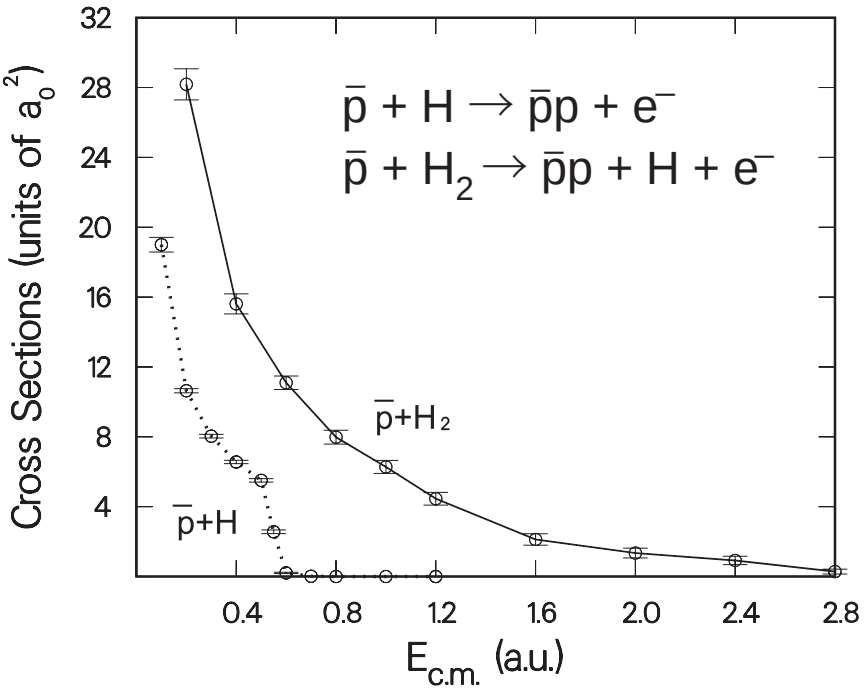

Figure 2.5: CTMC simulation of formation cross sections of protonium[46].

As is easily seen, to determine the formation cross section, we need to have monoenergetic, slow antiproton beams. In addition, other bound states formed in vacuo like $\overline{\mathrm{p}}\mathrm{He}^+$, $\overline{\mathrm{p}}\mathrm{Li}^+$, etc. will all be of interest[47] for a systematic understanding.

Fig.2.6 shows a comparison of measured and theoretical cross section of ionization of atomic deuterium by antiprotons. There are significant differences among theories in the lower energy region where there is no experimental data available. To elucidate, we need to have low energy beam of antiprotons.

[4]Here, we define an exotic atom as an atom in which one of the electrons is replaced by a heavier negatively charged particle like μ^-, π^-, K^-, $\overline{\mathrm{p}}$, etc.

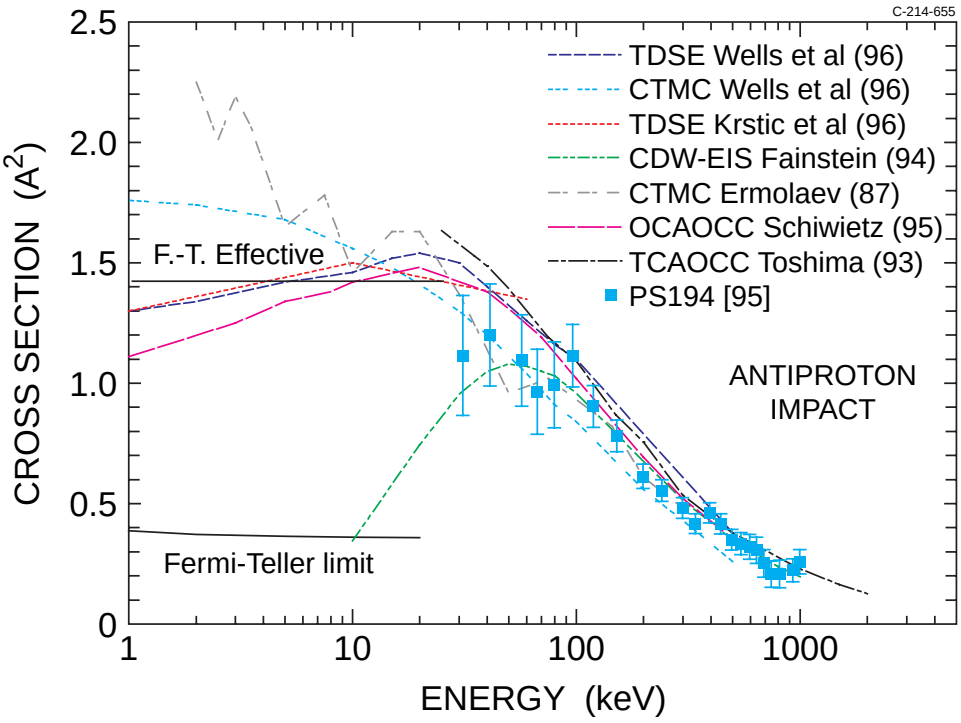

Figure 2.6: Ionization cross section of atomic deuterium with antiproton impact[48].

Hydrogen is a matter with the simplest atomic structure and serves as a starting point of atomic physics. Deuteron, which contains one proton and one neutron, is the most basic material to understand the nuclear force. Positronium has been a matter of question for precision tests of QED theory. In the same manner, $p\overline{p}$ will be of great importance as the elementary composite of matter and antimatter.

Furthermore, by elucidating the interactions of antiprotons with matters, we would be able to use antiprotons as a probe. For example, in the case of positron, by using their nature to produce two photons in opposite direction at the annihilation they can be used as a probe like PET. It is possible only after we understand the interaction.

That is how we were motivated to produce ultracold antiproton beam.

2.2.1 Summary of planned experiments

Table 2.1 summarizes the scope of the ASACUSA proposal in comparison with the PS200, PS205, and PS194 experiments at LEAR.

Table 2.1: The scope of the ASACUSA proposal in comparison with previous LEAR experiments[41].

	At LEAR	Present proposal	Keywords
Mode	Parasitic beam	Dedicated	
$\overline{\mathrm{p}}$ energy	5.3 - 21 MeV	5.3 MeV	
($\overline{\mathrm{p}}$ intensity)	(10^{8-9}/pulse, 1 pulse/10min)	(10^{7}/pulse, 1 pulse/min)	
	(10^{4-5}/sec, continuous)	10 - 130 keV with RFQ	High energy regime
		($\sim 10^{7}$/pulse, 1 pulse/min)	→ Low energy regime
		10 eV - 10 keV DC from Trap	
Laser wavelength accuracy	5 ppm	0.2 ppm	$\overline{\mathrm{p}}\mathrm{He}^{+}$ confirmation
			→ High-precision test of 3-body theory
High resolution spectroscopy	Resolved by laser	Microwave-laser triple resonance	Level schemes established
	(3% accuracy)	(10^{-7} accuracy)	→ Improve antiprotonic Rydberg constant
			Hyperfine splitting observed
			→ QED test of the hyperfine structure
			Initial population and lifetimes
			→ "Primordial" population
			Interaction with H_2
			→ Systematic study of quenching by H_2, D_2 and other atoms/molecules.
$\overline{\mathrm{p}}$ energy loss	$30 - 3000$ keV	$10 - 130$ keV from RFQ	High energy regime
			→ Low energy regime
	Solid targets	Si and He	
	TOF measurements	Electrostatic energy selection and analysis	
$\overline{\mathrm{p}}$ channeling	1.4 MeV	$\sim$ 100 keV from RFQ	High energy regime
			→ Low energy regime
$\overline{\mathrm{p}}$ ionization	$13 - 3000$ keV	$1 - 10$ keV from Trap	Fast collisions
			→ Adiabatic collisions of few-body systems
	Atomic hydrogen	Atomic hydrogen	
	Noble gases	Noble gases	
	Molecules		
	Single and multiple ionization	Single and double ionization	
$\overline{\mathrm{p}}$ capture	———	50 keV from RFQ	→ $\overline{\mathrm{p}}$ drift in dense media
		10 - 100 eV from Trap	→ Initial stage of $\overline{\mathrm{p}}$ atom formation
			→ Search for stable $\overline{\mathrm{p}}$ atoms in vacuum

2.3 ASACUSA project - Preparation of ultracold antiprotons

To perform the experiments which requires ultraslow antiprotons, two steps will be taken to further decelerate antiprotons from AD. In Table 2.2, production scheme of ultracold antiprotons is given.

Machine	Energy of antiprotons
AD	5.3 MeV
↓	
RFQD	$\sim$ 50 keV
↓	
Trap	$<$ 10 eV
↓	
Extraction beamline	1 keV - 10 eV

Table 2.2: Production scheme of ultraslow antiprotons.

A radio frequency quadrupole decelerator(RFQD) was designed for the ASACUSA project by a specially organized work group at CERN[49][5]. Ejected antiprotons from AD have energy of 5.3 MeV. In other experiments (ATHENA, ATRAP ; See Section 2.1), degrader foils are located in their path so that a certain fraction of antiprotons will have axial energy below the catching wall potential, whose height is limited by a power supply. Thus, the trapping efficiency are extremely low (It was $\sim$ 0.1 % in the case of PS200.). In our case, for the sake of RFQD, we can expect trapping efficiency of the order of several tens of percent, more than two order of magnitude higher than other trapping experiments, which is essential for the *beam* generation.

The RF electrodes are floatable so that the output energy is variable within the range 10keV - 120keV.

After the RFQD, low energy beam transport part comes. Its function is to transport the decelerated beam and focus it at the trap (or other target). As focusing elements, two normal conducting solenoids are used. Drawing of the low energy transport part is shown in Fig.2.8.

[5]Also at LEAR, usage of RFQ as a post decelerator was considered around 1992 but the tests were not successful.

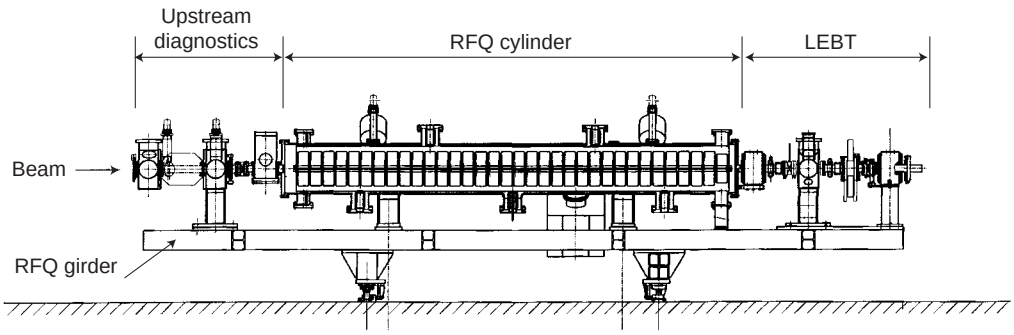

Figure 2.7: Structure of RFQD together with beam transport sections.

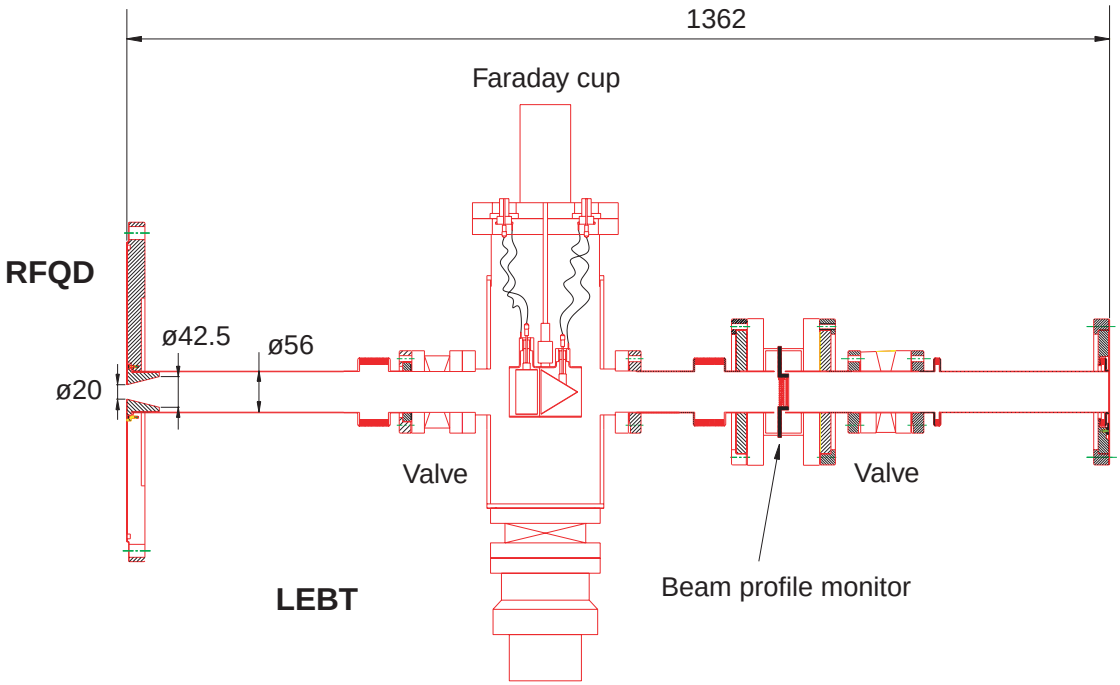

Figure 2.8: Details of Low Energy Beam Transport (LEBT) section.

Simulations of the low energy beam transport through RFQD and LEBT to the trap located in the middle of a superconducting solenoid were performed[50]. The results are shown through Fig.2.9 to Fig.2.12. In Fig.2.9, geometries are given. By optimizing the field strength of the solenoid, the diameter of antiproton beam was reduced down to 5 mm at the trap center (Fig.2.10) Fig.2.11) shows the transversal beam characteristics. In the simulation, 503 particles were used. Moreover, 34% of the particles coming from AD can be delivered within a square of 1 mm $\times$ 1 mm in a plane perpendicular to the beam direction.

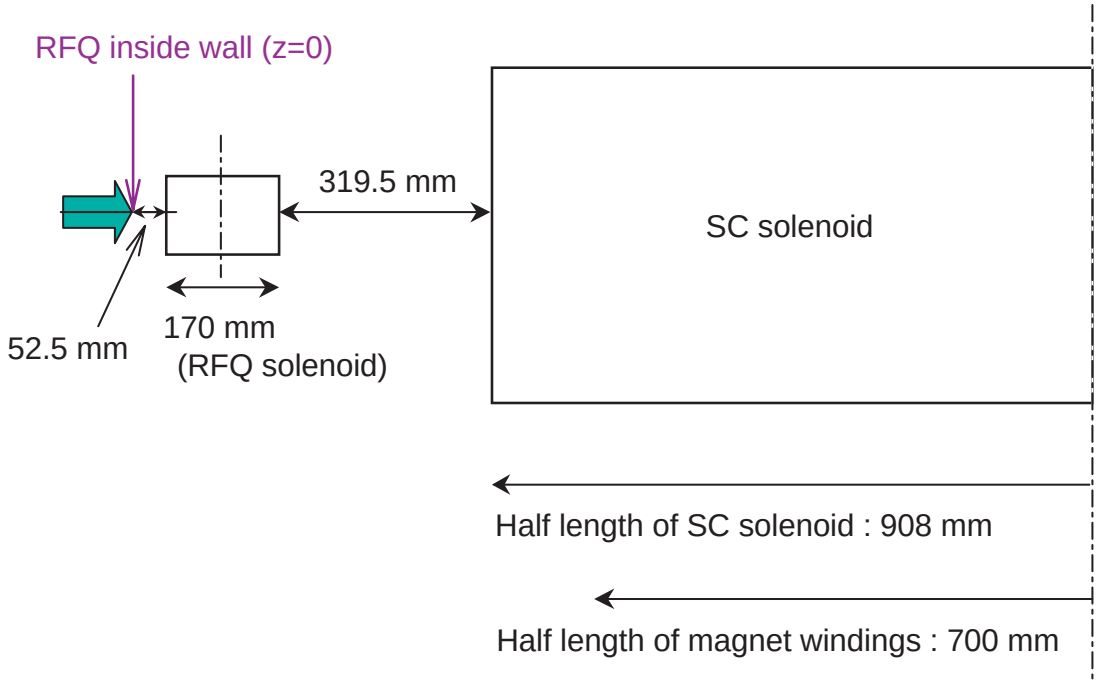

Figure 2.9: Geometry for the simulation of beam transport from the RFQD to the trap. The z-axis is taken along the axis of azimuthal symmetry with its origin at the RFQ inside wall.

For the augmentation of trapping efficiency[6], to put a degrader foil is considered. Fig.2.12 shows the result including the foil. The ratio of the antiprotons which has its position inside a square of 1 mm $\times$ 1 mm will be 36%, slightly better than the case

[6]We are planning to inject antiprotons at 60 keV into the trap while designed stopping potential is 10 kV. Without the degrader foil, practically no antiprotons will be captured in the trap. We can expect to increase the trapping efficiency by applying a voltage on the foil so that the incoming particles are accelerated before the foil because energy struggling will be smaller.

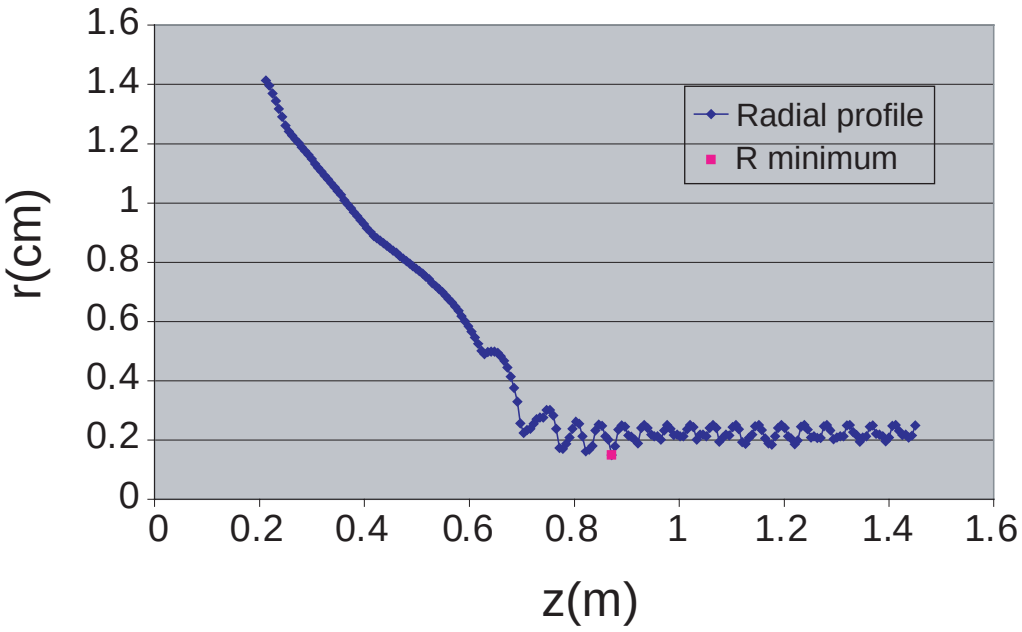

Figure 2.10: Simulated beam envelope. Total diameter of about 5 mm is achieved.

without the foil. Although the drawback like an increase in the beam divergence and the particle loss might occur, no negative effect has been found in the simulation.

Once antiprotons are caught in the trap, reduction of their energy will proceed as shown in Fig.2.13. First of all, electrons are preloaded in the trap and they cool themselves via synchrotron radiation. Then, antiprotons with a few tens of keV are injected and caught by rapid switching of the entrance high voltage. Antiprotons give part of their energy to electrons by Coulomb collisions and electrons radiates. Eventually, both electrons and antiprotons will be cooled. Extraction will be done by changing the potential.

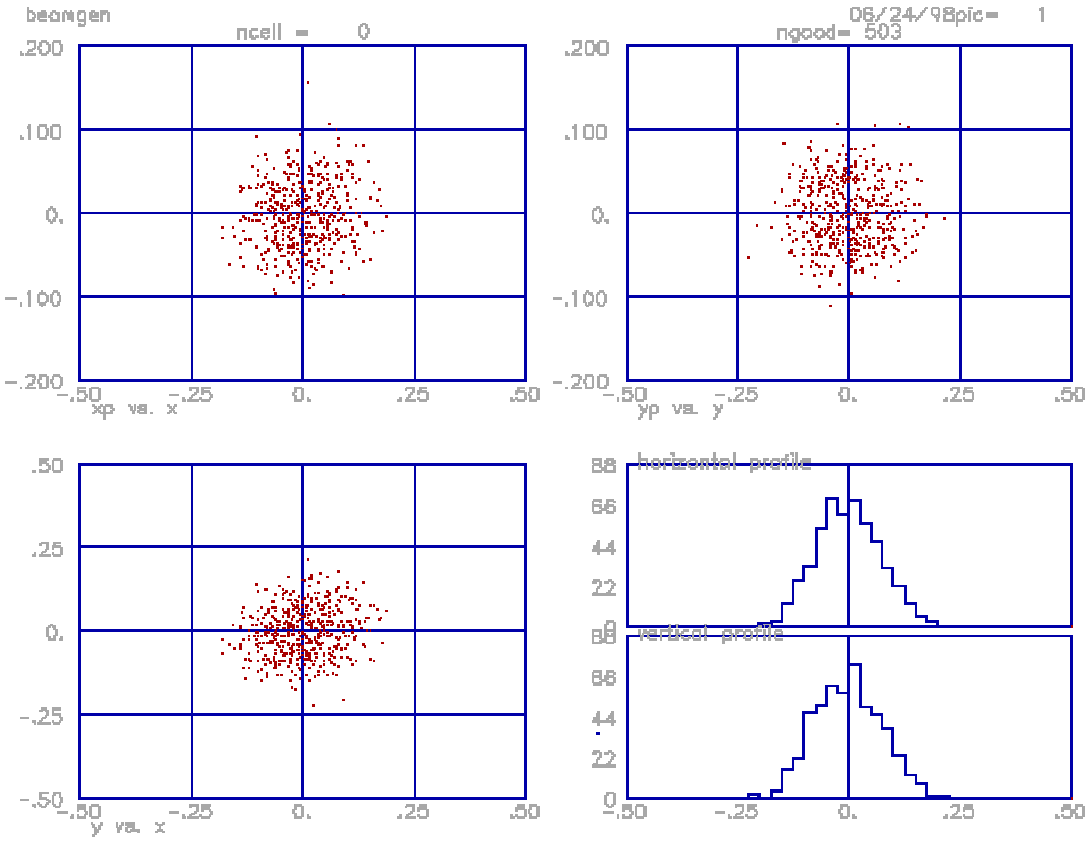

Figure 2.11: Transversal beam characteristics at z = 1.45 m. 503 particles are used in the simulation.

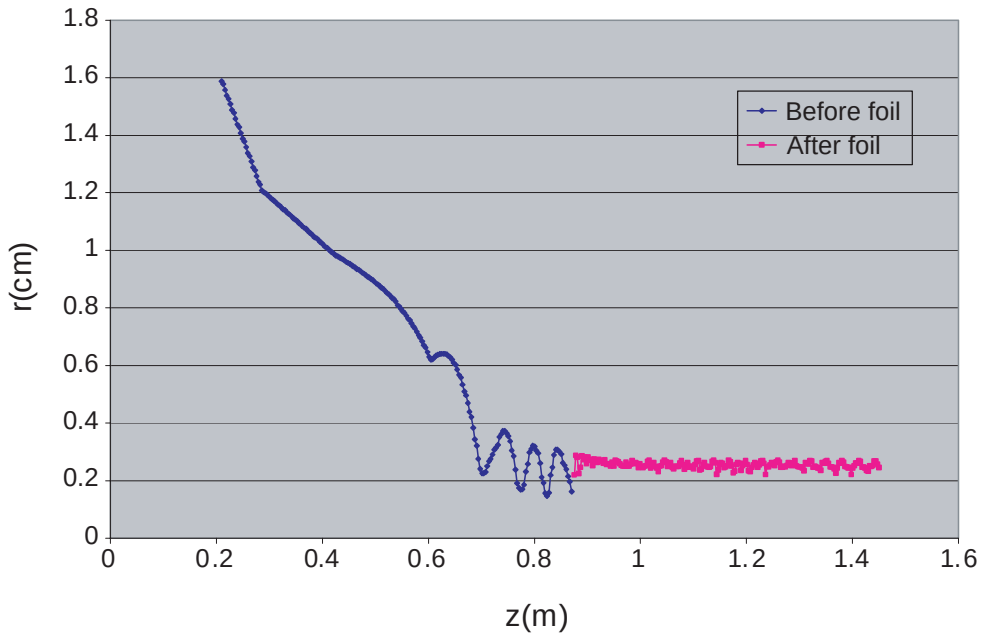

Figure 2.12: Beam transport simulation including a degrader foil.

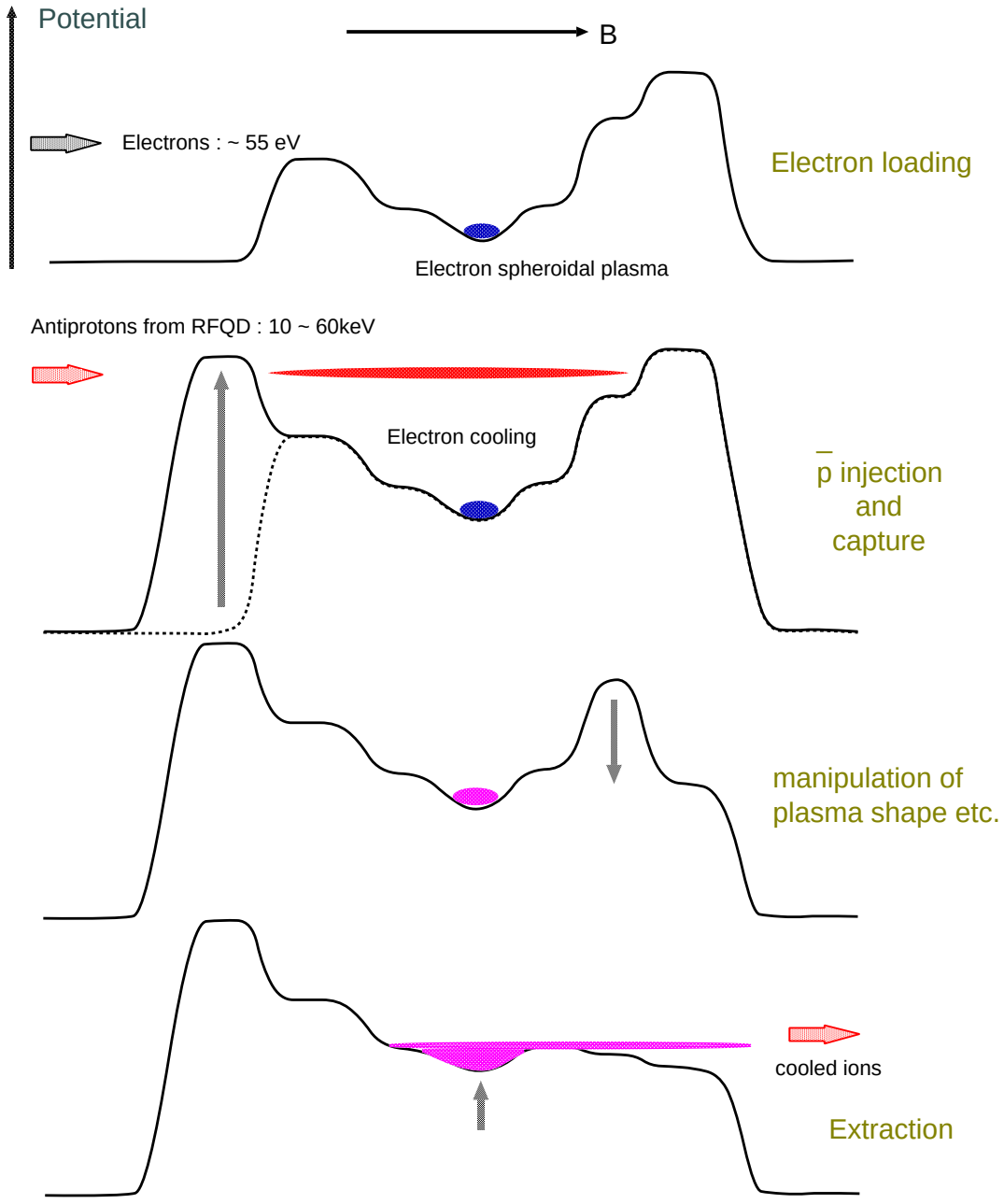

Figure 2.13: Capture and cooling of antiprotons from RFQD. Antiprotons captured by rapid change in the entrance potential lose their energy via Coulomb interactions with preloaded electrons. After diagnoses and centering, cooled antiprotons will be extracted as a beam.

Chapter 3

Properties of plasmas

3.1 Plasma oscillation

For easiness, suppose that ions and electrons coexist with the same density n_0. If the density of electrons becomes $n_e = n_0 + \delta n$,

$$\frac{\partial n_e}{\partial t} + \nabla n_e \mathbf{v}_e = 0 \text{ (Equation of continuity)} \tag{3.1}$$

$$n_e m_e \left\{ \frac{\partial \mathbf{v}_e}{\partial t} + (\mathbf{v}_e \cdot \nabla)\mathbf{v}_e \right\} = -n_e e \mathbf{E} \text{ (Equation of motion)} \tag{3.2}$$

$$\nabla \cdot \mathbf{E} = \frac{e}{\epsilon_0}(n_i - n_e) \text{ (Poisson's equation)} \tag{3.3}$$

Let it be supposed that $\delta n, \mathbf{v}_e, and \mathbf{E}$ are small. Finding a solution to δn neglecting the quantities smaller than $(\delta n)^2$,

$$\frac{\partial^2 \delta n}{\partial t^2} + \frac{n_0 e^2}{m_e \epsilon_0} \delta n = 0. \tag{3.4}$$

This shows that δn oscillates at the frequency

$$\omega_p = \sqrt{\frac{n_0 e^2}{m_e \epsilon_0}}, \tag{3.5}$$

which is called the plasma frequency.

3.2 Debye length and plasma shielding

Let us take a spherical coordinate with its origin on a charged particle inside a cloud of charged particles. To investigate the potential around this test charge, we can start by the Possion's equation,

$$\nabla^2\phi = \frac{e}{\epsilon_0}(n_i - n_e). \tag{3.6}$$

Assuming (1)that heavy ions do not move significantly and (2)that electron's distribution function is Maxwellian, we can write

$$\begin{aligned} n_i &= n_\infty \\ n_e &= n_\infty \mathrm{e}^{\frac{e\phi}{k_B T_e}} \end{aligned} \tag{3.7}$$

Substituting n_i and n_e for the Eq.(3.6),

$$\epsilon_0 \frac{1}{r^2}\frac{\partial}{\partial r}\left\{ r^2 \frac{\partial \phi(r)}{\partial r} \right\} = e n_\infty \left[\mathrm{e}^{\frac{e\phi}{k_B T_e}} - 1 \right] \tag{3.8}$$

Assuming that the relation $e\phi(r) \ll k_B T$ holds, we can find a solution of Eq.(3.8)

$$\phi(r) = \pm \frac{e\,\mathrm{e}^{-\frac{r}{\lambda_D}}}{4\pi\epsilon_0 r}. \tag{3.9}$$

Here we defined the Debye length : $\lambda_D \equiv \sqrt{\frac{\epsilon_0 k_B T}{n_0 e^2}}$. It can be seen that the field of the test charge is screened out by surrounding charges with a characteristic length of λ_D. When the size of the charged particle clouds is larger than λ_D, since individual particle beyond the Debye length cannot be identified from the test charge, collective phenomena will be important. We can define that system as a plasma.

As we assumed that the motion of ions does not take an important role, the property of the plasma is considered to be mainly determined by electrons. Thus it is possible to extend the notion to the whole system consists of electrons. Further more, since the definition of the Debye length is also valid for ions, we can generally define plasmas without charge neutrality.

3.3 Basic equations

3.3.1 Boltzmann equation

Assuming a distribution function depends on space, momentum and time, we can generally write its time derivative as

$$\frac{df}{dt} = \frac{\partial f}{\partial t} + \frac{\partial f}{\partial x}\frac{dx}{dt} + \frac{\partial f}{\partial y}\frac{dy}{dt} + \frac{\partial f}{\partial z}\frac{dz}{dt} + \frac{\partial f}{\partial v_x}\frac{dv_x}{dt} + \frac{\partial f}{\partial v_y}\frac{dv_y}{dt} + \frac{\partial f}{\partial v_z}\frac{dv_z}{dt}. \tag{3.10}$$

From Newton's third law,

$$m\frac{d\mathbf{v}}{dt} = \mathbf{F}. \tag{3.11}$$

Then, we can rewrite the last three terms as follows.

$$\begin{aligned} \frac{\partial f}{\partial v_x}\frac{dv_x}{dt} + \frac{\partial f}{\partial v_y}\frac{dv_y}{dt} + \frac{\partial f}{\partial v_z}\frac{dv_z}{dt} &= \frac{\mathbf{F}}{m}\cdot\frac{\partial f}{\partial \mathbf{v}} \\ &= \mathbf{F}\cdot\frac{\partial f}{\partial \mathbf{p}}. \end{aligned} \tag{3.12}$$

By further assuming that the net change of f is only caused by collisions, we have

$$\frac{\partial f}{\partial t} + \mathbf{v}\cdot\nabla f + \mathbf{F}\cdot\frac{\partial f}{\partial \mathbf{p}} = \left(\frac{df}{dt}\right)_{coll}. \tag{3.13}$$

Eq.(3.13) gives the Boltzmann equation. Here, the meaning of the word "collision" needs to be explained. In most of the case, electromagnetic force is so important to treat plasmas that we can write the external force on a particle in a plasma as $\mathbf{f} = q(\mathbf{E}+\mathbf{v}\times\mathbf{B})$. Of course the Coulomb force is long-range, that means for $\mathbf{E}$ or $\mathbf{B}$ at a certain point in space, contribution from distant charged particles is not negligible. Nevertheless, these contributions from particles farther than the Debye length can be renormalized into global parameters $\mathbf{E}$ and $\mathbf{B}$. Hence the right-hand side of Eq.(3.13) represents actions by charged particles in the vicinity of a position in consideration. This is what is meant by "collision".

3.3.2 Vlasov equation

When we can neglect the effect of collisions, Boltzmann equation reduces to

$$\frac{\partial f}{\partial t} + \mathbf{v}\cdot\nabla f + \mathbf{F}\cdot\frac{\partial f}{\partial \mathbf{p}} = 0 \tag{3.14}$$

This is the so-called Vlasov equation (= collision-less Boltzmann equation). As an inter-particle interaction, it only contains the one from collective motion of particles. In turn, it is suitable for the description of plasmas where collective motions is the main characteristics. Normally, to solve Eq.(3.14) we need to know $\mathbf{E}$ and $\mathbf{B}$, which are determined by the distribution function f. Thus, it is necessary to solve Eq.(3.14) with a set of Maxwell equations simultaneously.

3.4 Spheroidal non-neutral plasma

3.4.1 Rigid-rotor equilibria

When we can neglect the transport of the particles, ionization, recombination etc., the system can be said to be collisionless and we can examine the equilibrium with Vlasov-

Maxwell equations. Let us further assume that the particles are non-relativistic and the self magnetic field created by their motion is negligible. Let us write the distribution function with the constants of motion, especially in the form

$$f^0 = f^0\left(H_\perp - \omega_r L_z, p_z\right). \tag{3.15}$$

Here, superscript "0" means that the system is in the thermal equilibrium and

$$H_\perp = \frac{m}{2}\left(v_x^2 + v_y^2\right) - q\phi(r). \tag{3.16}$$

Supposing a uniform magnetic field in z-direction, we can calculate the canonical angular momentum from Eq.(A.5),

$$L_z = \hat{\mathbf{z}} \cdot \mathbf{r} \times \mathbf{p} = m(x\dot{y} - y\dot{x}) + \frac{qB}{2}\left(x^2 + y^2\right). \tag{3.17}$$

Thus

$$\begin{aligned} H_\perp - \omega_r L_z &= \frac{m}{2}\left(v_x^2 + v_y^2\right) - q\phi(r) - m\omega_r(x\dot{y} - y\dot{x}) + \frac{qB\omega_r}{2}\left(x^2 + y^2\right) \\ &= \frac{m}{2}\left(v_x + \omega_r y\right)^2 + \frac{m}{2}\left(v_y - \omega_r x\right)^2 - q\phi(r) - \frac{m}{2}\left(x^2 + y^2\right)\left(\omega_r^2 + \omega_c\omega_r\right). \end{aligned} \tag{3.18}$$

Note that the mean velocities at each space point are given by

$$\begin{aligned} \overline{v_x} &\equiv \frac{\int dv_x dv_y dv_z\, v_x f^0}{\int dv_x dv_y dv_z\, f^0} \\ &= \frac{\int dv_x dv_y dv_z\, \left\{(v_x + \omega_r y) f^0 - \omega_r y f^0\right\}}{\int dv_x dv_y dv_z f^0} \\ &= -\omega_r y \end{aligned} \tag{3.19}$$

and

$$\overline{v_y} = \omega_r x. \tag{3.20}$$

These relations describe a plasma rigidly rotating around z-axis with a frequency of $\boldsymbol{\omega_r} \times \hat{\mathbf{r}}$ (See Fig.3.1).

Then from the condition on radial confinement of the plasma, $n \overset{r\to\infty}{\to} 0$, we can find the parameter region of stable confinement (Fig. 3.2).

In the cold, uniform density limit, either ω_+ or ω_- will be realized depending on the initial formation condition of the plasmas[24, 51].

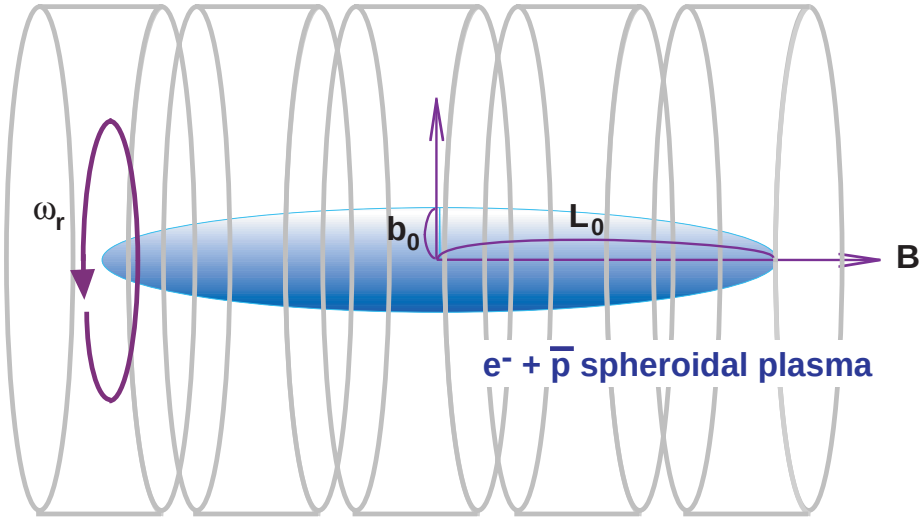

Figure 3.1: Rigid rotation of a plasma in a trap with cylindrical electrodes.

The lower hybrid of rigid rotation frequency is given by[52]

$$\omega_r = \frac{\omega_c}{2}\left\{1 - \left(1 - \frac{2\omega_p^2}{\omega_c^2}\right)^{\frac{1}{2}}\right\}. \tag{3.21}$$

If the plasma contain j different species, Eq.(3.21) takes the form of

$$\omega_{rj} = -\frac{\varepsilon_j \omega_{cj}}{2}\left\{1 - \left(1 - \sum_l \frac{2\omega_{pl}^2}{\omega_{cl}^2}\right)^{\frac{1}{2}}\right\}, \tag{3.22}$$

where $\varepsilon_j \equiv sgn(q_j)$. Especially, in the case of an antiproton + electron plasma, the rotation frequency of an antiproton (ω_{rp}) is given by

$$\omega_{rp} = \frac{\omega_{cp}}{2}\left\{1 - \left(1 - \frac{2}{\omega_{cp}^2}\left(\omega_{pp}^2 + \omega_{pe}^2 \frac{m_e}{m_p}\right)\right)^{\frac{1}{2}}\right\}. \tag{3.23}$$

Here, ω_{cp} and ω_{pp} are cyclotron and plasma frequency of antiprotons respectively and ω_{pe} is the electron plasma frequency. In Fig.3.3 below, contribution of this rotation to the energy, namely $\frac{1}{2}m_p(r\omega_{rp})^2$, of an outermost antiproton is shown for various combination of n_e and n_p.

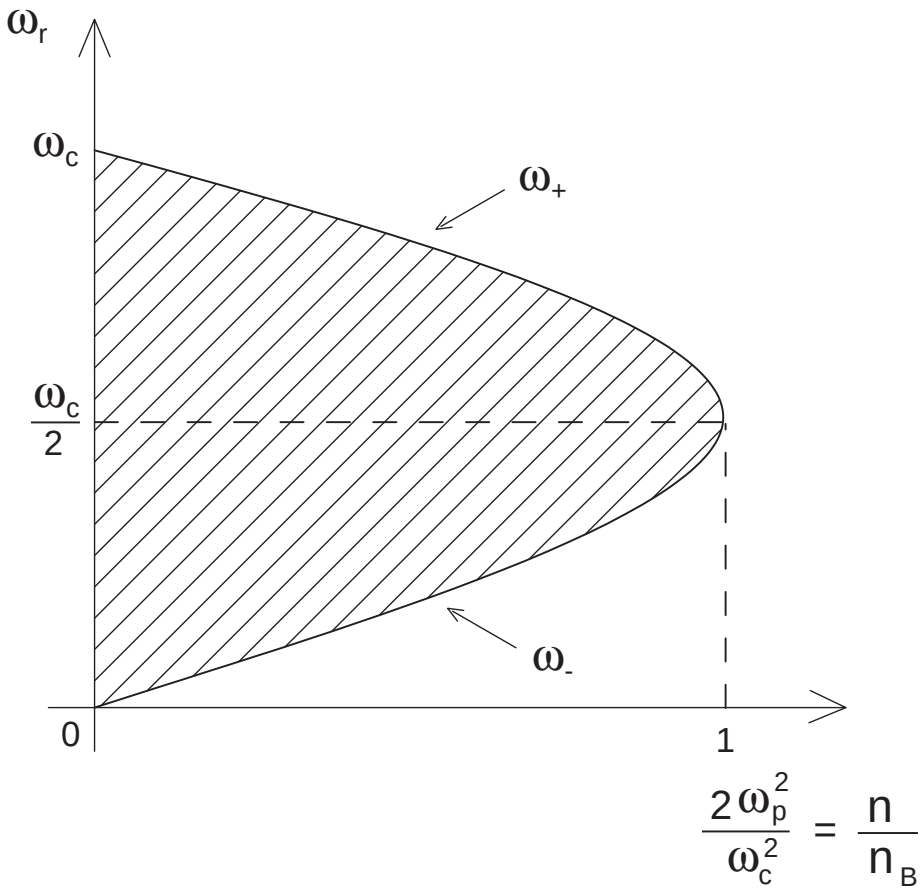

Figure 3.2: The hatched area in the figure represents a region where plasmas are radially confined. The parameter $\frac{2\omega_p^2}{\omega_c^2} = \frac{n}{n_B}$ is sometimes referred to as a self field parameter s_e. The quantity n_B is called the Brillouin density limit, defined in Sec.3.4.2.

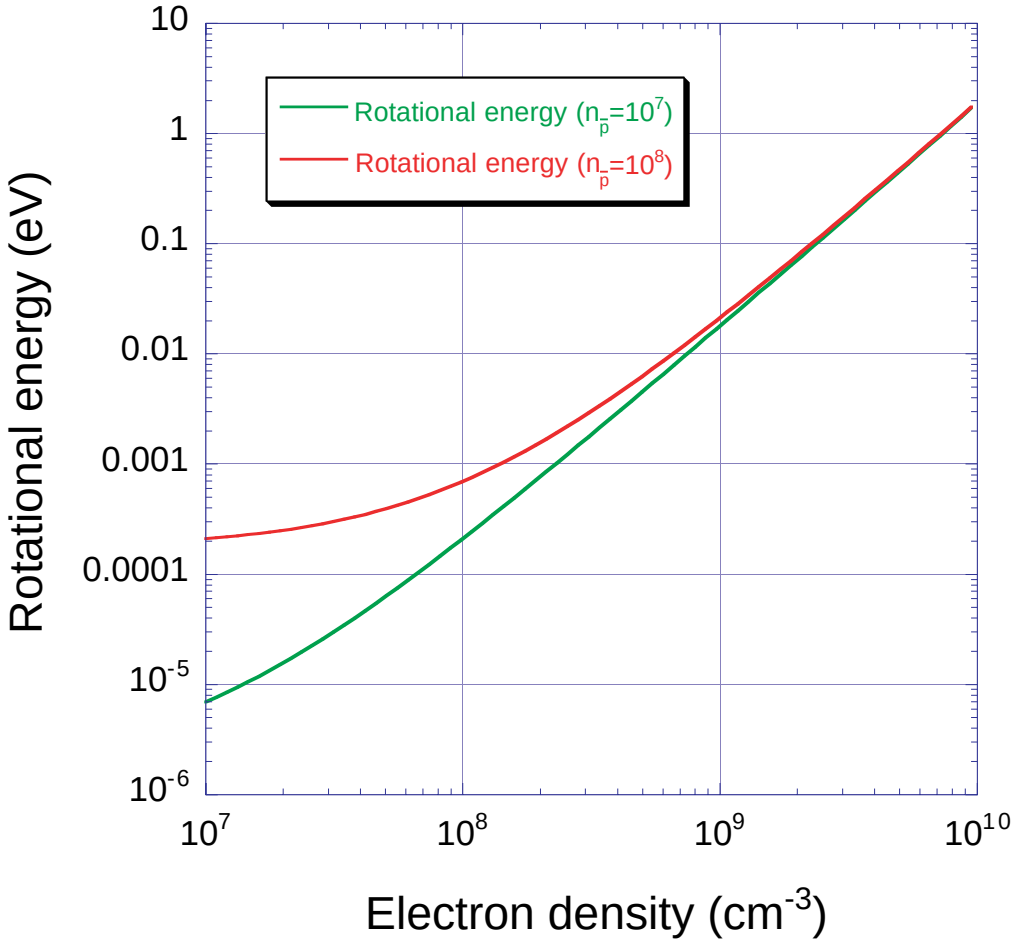

Figure 3.3: Rotational energy associated with the azimuthal rotation of the plasma. Plasma radius (b_0) was assumed to be 1 mm, and calculation was done for an antiproton at $r = 1$ mm).

We should memorize that the energy associated with the azimuthal rotation can be large even if the temperature of the plasma is low. Note also that under an equilibrium condition, heavier particles rotate faster than lighter ones. Putting the value of $n_p = 10^8$ [cm^{-3}], $n_e = 10^8$ [cm^{-3}], and $B = 5$ [T], rotation frequency becomes $\omega_{rp} = 390$ kHz for antiprotons and $\omega_{re} = 360$ kHz for electrons.

In addition, if there are more than two species with different mass or charge, centrifugal separation will occur. In experiments on systems which allow the sympathetic cooling[53, 54], the phenomena are actually observed. Since electron cooling is a kind of sympathetic cooling, it can also occur. So far, no reliable estimation is obtained on the time scale for it to happen.

3.4.2 The Brillouin limit

The radial force balance for a particle inside the plasma requires

$$-\frac{mv^2}{r} = -eE + evB. \tag{3.24}$$

$$\tag{3.25}$$

In the case of cylindrical plasma, Eq.(3.25) becomes

$$-\left(\frac{v}{r}\right)^2 = -\frac{1}{2}\frac{e^2 n}{m\epsilon_0} + \frac{eB}{m}\frac{v}{r}. \tag{3.26}$$

$$\tag{3.27}$$

Using characteristic frequencies, we can write Eq.(3.27) as

$$\omega_r^2 + \frac{1}{2}\omega_p^2 - \omega_c\omega_r = 0. \tag{3.28}$$

Here, $\omega_r \equiv \frac{v}{r}$ is the rigid rotation frequency of the plasma, described in Section 3.4.1. Eq.(3.28) has a solution when the relation

$$n \leq \frac{\epsilon_0 B^2}{2m} \equiv n_B \tag{3.29}$$

is satisfied. The equal sign in the Eq.(3.29) gives the Brillouin limit[55]. If the density of the plasma reaches this limit, canonical angular momentum becomes zero and the magnetic field has effectively no influence on the plasma[56], namely the flow can be regarded as free.

It is important to note that, in the case of electron + antiproton plasma, the electron density should not exceed the Brillouin limit of antiprotons. For example, in the magnetic field of 5 T, it cannot be larger than 6.6 $\times 10^{10}$ [cm^{-3}] for the coexistence of two species.

3.4.3 Electrostatic modes

The first formulation of plasma modes of spheroidal non-neutral plasmas was done by Dubin[25], assuming that the plasma is in $T = 0$ cold fluid thermal equilibrium[1].

According to his theory, the problem is reduced to solve Maxwell's equation inside and outside the plasma, and by connecting the solutions at the boundary, we can find a relation :

$$\epsilon_3 + m\alpha\left(\alpha^2 - \frac{\epsilon_3}{\epsilon_1}\right)^{\frac{1}{2}}\frac{P_l^m}{P_l^{m\prime}}\epsilon_2 = -\left(\frac{\alpha^2 - \frac{\epsilon_3}{\epsilon_1}}{\alpha^2 - 1}\right)^{\frac{1}{2}}\frac{P_l^m(k_1)Q_l^{m\prime}(k_2)}{P_l^{m\prime}(k_1)Q_l^m(k_2)}. \tag{3.30}$$

[1] In the case of infinitely long cylindrical plasmas, the dispersion relation is given by Trivelpiece-Gould modes[57].

Here P_l^m and Q_l^m are respectively associated Legendre functions of the first and the second kind with arguments $k_1 = \frac{\alpha}{\left(\alpha^2 - \frac{\epsilon_3}{\epsilon_1}\right)^{\frac{1}{2}}}$, $k_2 = \frac{\alpha}{(\alpha^2-1)^{\frac{1}{2}}}$, and l is a non-negative integer ($l \geq |m|$). Other factors are given by $\epsilon_1 = 1 - \frac{\omega_p^2}{(\omega^2-\omega_v^2)}$, $\epsilon_2 = \frac{\omega_v \omega_p^2}{\omega(\omega^2-\omega_v^2)}$, $\epsilon_3 = 1 - \frac{\omega_p^2}{\omega^2}$ and $\omega_v = \omega_c - 2\omega_r$ (cyclotron frequency seen on the frame rotating with the plasma). $\alpha \equiv \frac{L_0}{b_0}$ is the aspect ratio of the plasma, where L_0 and b_0 are defined in Fig.3.1.

This equation relates a mode number (l, m) to a frequency ω. The index m denotes an azimuthal dependence on the plasma modes.

In the limit of strongly magnetized plasmas ($\omega_p \ll \omega_c$), the cold fluid dispersion relation (Eq.(3.30)) for low order modes ($\omega \ll \omega_c$) with azimuthal symmetry reduces to[36]

$$\epsilon_3 - \frac{k_2}{k_1} \frac{P_l(k_1) Q_l'(k_2)}{P_l'(k_1) Q_l(k_2)} = 0. \tag{3.31}$$

In Table 3.1, some of modes with lower mode numbers are listed with schematic drawing of motion.

Mode number	Frequency	Schematic drawing
(l,m)=(1,0)	10.6 MHz	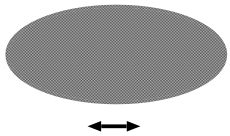
(1,1)		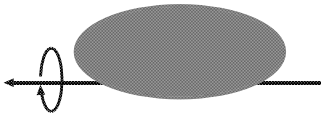
(2,0)	17.4 MHz	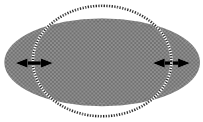
(2,1)		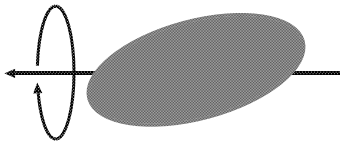

Table 3.1: Normal modes of spheroidal nonneutral plasmas. Frequencies are calculated for $b_0 = 1$ mm, $N_e = 1.0 \times 10^8$, $B = 1$ T, $V_{trap} = 50$ V.

Frequencies are calculated by numerically solving Eq.(3.31), assuming these parameters: plasma radius $b_0 = 1$ mm, total number of constituent particles $N_e = 1.0 \times 10^8$,

magnetic field strength $B = 1$ T, and trap depth $V_{trap} = 50$ V. Under these condition, α becomes 38.6.

Now let us consider the density profile. It is given by

$$n(\alpha) = \frac{2V_{trap}}{\pi e(2L_0^2 + b_0^2)\beta(\alpha)} \tag{3.32}$$

where

$$\beta(\alpha) = -\frac{2\left(\frac{1}{\alpha}\right)^2}{1-\left(\frac{1}{\alpha}\right)^2} + \frac{\left(\frac{1}{\alpha}\right)^2}{\left(1-\left(\frac{1}{\alpha}\right)^2\right)^{\frac{3}{2}}} \log\left|\frac{1+\sqrt{1-\left(\frac{1}{\alpha}\right)^2}}{1-\sqrt{1-\left(\frac{1}{\alpha}\right)^2}}\right|. \tag{3.33}$$

When the distribution function is of the form

$$f(r, \mathbf{p}) = \frac{n_0}{2\pi m k_B T} \mathrm{e}^{-\frac{H-\omega_r P_\theta}{k_B T}}, \tag{3.34}$$

namely when the plasma has a finite temperature, the density in the equilibrium is given by

$$n(r) = n_0 \mathrm{e}^{\frac{m}{2k_B T}\left[r^2(\omega_r\omega_c - \omega_r^2) - \frac{2e}{m}\phi(0)\right]}. \tag{3.35}$$

When the existence of the electrode cannot be neglected, in other words, when we cannot assume that the electrode wall is far from the plasma, frequencies will differ from calculated values above because of the image charge[38].

3.5 Multi-ring electrode trap

When a Penning type trap is dedicated to the confinement of plasmas with electrodes consist of cylinders , it is often called Malmberg (- Penning) trap. Combination of rectangular potential well and magnetic field is used. This is widely used in the studies of trapped nonneutral plasmas.

Multi-ring electrode trap[38, 58] was originally developed at the Kyoto University, which can be considered to be an axially elongated Penning trap of a plasma version. Electrodes consists of a number of cylinders, which facilitates, for example, compensation of an image charge created by a trapped plasma. In the case of cylindrical plasma, confinement property depends on the length of the plasma(Section 1.2), while multi-ring structure assures longer lifetime with little dependence on the plasma length. This new apparatus has opened a new area of research like the survey of various plasma modes[59], voteces[60, 61, 62], etc. It is also planned to use this type of trap for the generation of cold positron plasmas[63].

Chapter 4

ASACUSA Trap - Design and Construction

4.1 Selection of the cooling method and the type of the trap

For the production of cold antiprotons, cooling is necessary. What we need to do is to reduce the energy from negatively charged antimatter that has no atomic level. Table 4.1 compares three major cooling methods. Laser cooling is the method with which one can achieve the lowest energy, but only when appropriate energy levels for laser irradiation are available. It is not the case for antiprotons. Buffer gas cooling is known as one of the best cooling method for positrons. However, cooled antiprotons will form exotic atoms with coolant molecules, and eventually annihilates. Unlike others, electron cooling is suitable for the purpose. Antiprotons can coexist with electrons which radiate their energy in the strong magnetic field. At LEAR, this technique was actually applied to the relatively small number ($< 10^5$) of antiprotons trapped in Penning traps.

Cooling method	Laser cooling	Buffer gas cooling	Electron cooling
Availability	×	×	◯
	No atomic level	Annihilation with materials	In Penning traps etc.

Table 4.1: Selection of cooling methods.

Though the consideration above leads us to the usage of a Penning trap for the cooling, if we are to store a number of particles in the trap, the size will be huge. On the other hand, cooled antiprotons will behave like a nonneutral plasma. For example, for a cloud of antiprotons with 100 K, density at 10^8 cm^{-3}, the Debye length will become about

100 μm, which will be much smaller than the trap size. As a container of nonneutral plasmas, Penning-Malmberg trap is known, which unfortunately has a length-dependent confinement property (Sec.(1.2). This seems to be at least partly because of the fact that longer well potential creates longer field free region where only self-field of the plasma exist. Multi-ring trap can realize a large trapping volume as well as a field anywhere inside the trap.

4.2 Design concepts

In designing the trap, following three requirements are especially considered :

1. The number of trapped particles will be 10^{7-9}, for 10^{6-8} antiprotons cooled by electrons.

2. Preparation of antiprotons with sub-eV energy within one minute (the value of which comes from the pulse interval at AD).

3. For the extraction of cooled antiprotons from the trap which is located in the strong magnetic field, it is necessary to manipulate the shape of plasmas.

As low energy charged particles tend to follow the field line, it is essential to make the position of the particles as close to the axis as possible for their extraction as a beam. One solution is the application of a rotational electric field, known as a "rotating wall method". Such a field can exert a torque on the plasma so that the plasma shape can be changed[64, 65]. This method is thought to be effective in our application and one of the electrodes is segmented for the radial compression of the plasma.

When the plasma composed of electrons and antiprotons is axially compressed in this way, it stretches in the harmonic region. It can be noted that the square potential does not allow such an axial expansion that the space charge can be higher. To reduce the space potential while keeping the cooling power high enough, central harmonic region is elongated in the axial direction so that the density will be optimum. Multi-ring structure[38, 58] is exploited to generate such a harmonic potential. Within a family of Penning-type trap, that is a unique apparatus which can contain charged particles in a large harmonic potential.

Advantages to have axially long harmonic potential region are :

(a) It ensures longer lifetime of plasmas than in the case of square potential (See Section 5.2).

(b) When the plasma radii are reduced, plasmas can freely accommodate themselves so that their axial lengths are longer, which can reduce a space charge.

(c) It defines a frequency of the plasma CM motion ((1,0) frequency) which can be used for diagnoses and controls. For example, sideband cooling of plasma by coupling the (1,0) mode and rigid rotation becomes possible.

(d) Image charge can be compensated, if necessary. When the existence of the wall is not negligible, plasma mode frequencies will differ from the value calculated without image charge effect, which prevents the precise determination of densities and aspect ration etc.

4.2.1 Electrodes of the harmonic region

Electrodes in the central harmonic region are designed so that they create a potential as shown in Fig.4.1. In cylindrical coordinates, the potential inside the electrode can be expressed as

$$\phi(r, z) = \sum_{n=1} A_n I_0(nkr) \cos(nkz). \tag{4.1}$$

Here, I_0 is a modified Bessel function of the first kind. Calculation was done by connecting the Fourier expansion of the potential at the electrode (one hundred terms in Fourier series were used) to the potential inside (Eq.(4.1)). In Fig.4.1, the graph on top (a) shows the potential applied on the electrode, which form a potential at $r = 1$ cm as in (b) and on the center axis as in (c). The superposition of a quadrupole function onto the potential distribution along the center axis (d) shows a fairly well agreement. Their difference is shown in (e). We emphasize that the trapping region is much larger than any other traps for spectroscopy. Practically, the truly quadratic potential for the high precision spectroscopy can be realized only in a limited volume[66]. The point is that we have quadratic trapping region of the size comparable to the one of nonneutral plasma apparatus (Malmberg-Penning traps) which can only produce square potential.

4.2.2 Effect of error fields

The existence of asymmetries in the electrode structure or in magnetic field distribution can cause a drag on the plasma so that the plasma would radially expand[67, 68, 69]. Transport can be caused either by electric field asymmetry (due to the $\mathbf{E} \times \mathbf{B}$ drift) or by magnetic field asymmetry (due to the $\nabla \mathbf{B}$ drift). When the pressure around the trap is less than 10^{-8} Torr, particle loss due to field asymmetry can be dominant[29, 70].

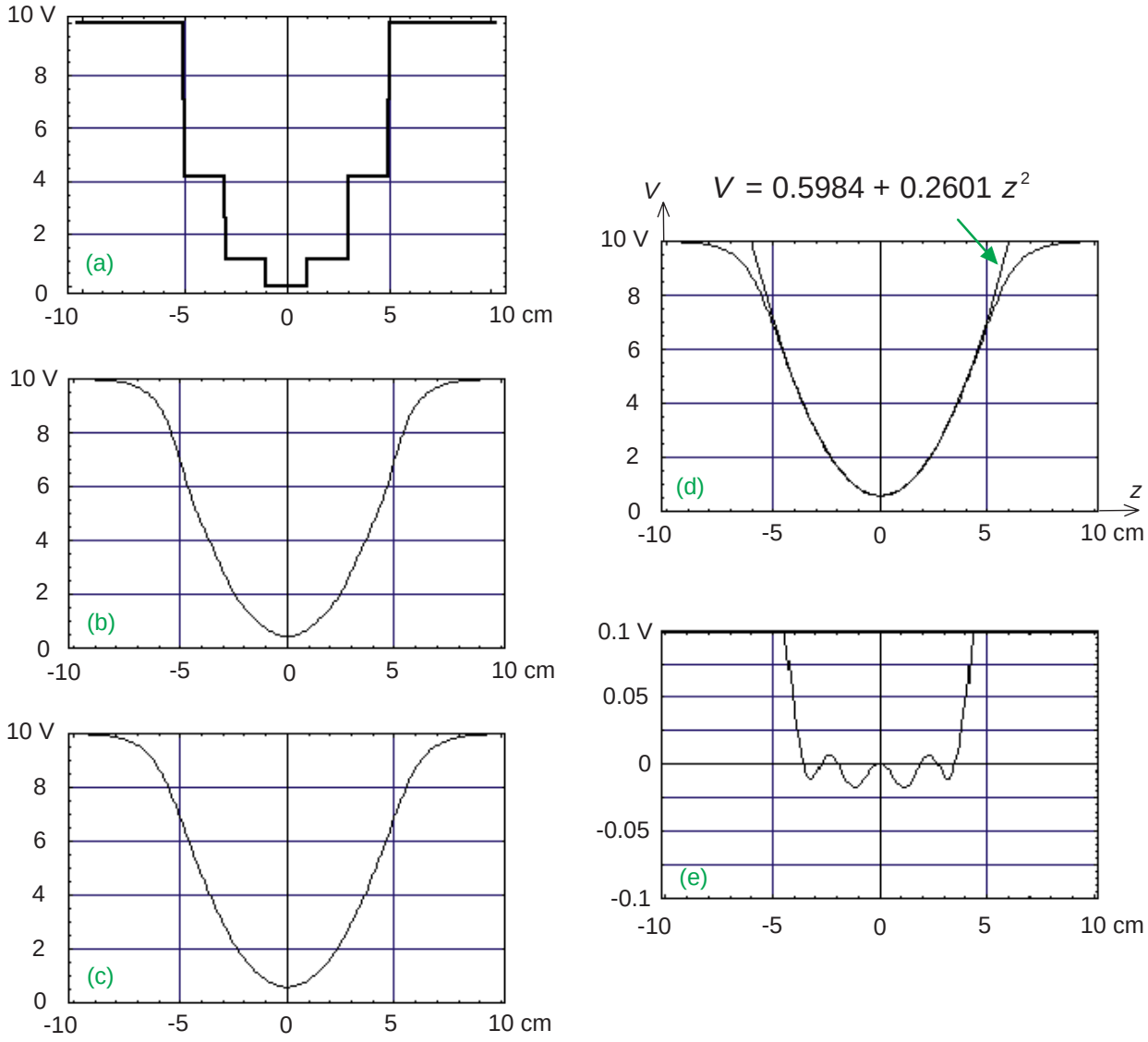

Figure 4.1: Calculation of the potential. (a) Potential given at the electrode surfaces ($r = 2$ cm). (b) Potential along z-axis, at $r = 1$ cm. (c) Potential along the center axis. (d) Superposition of quadratic function on (c). (e) Difference between the quadratic function and the potential along the center axis.

4.2.3 On the extraction of stored particles

As was previously experienced[11], extraction of ultracold antiprotons from a Penning trap would be extremely difficult primarily because :

1. Slow antiprotons tend to follow the magnetic field line which is diverging at the end of the solenoid.

2. Experiments with gaseous targets are planned. Several apertures with small diameters are necessary to make the effective differential pumping.

Simulation of beam extraction is being performed[71]. Extraction energy of 1keV is assumed. If antiprotons are radially located within 1mm in radius, it seems possible to transport them from the trap to the chamber a few meter apart from it. This results coincides with the former simulation[11]. Just before the target, beam energy will be reduced. As an example of low energy beam generation from initially hot particles, we note that so far, cold positron beam was obtained in the magnetic field[72].

4.3 Calculation of the time constant of electron cooling of antiprotons

Supposing that an antiproton cloud (density n_p, temperature T_p[K]) and an electron cloud (density n_e, temperature T_e[K]) are uniformly mixed at a time $t = 0$, numerical calculations were done to estimate the time necessary for the electron cooling of antiprotons. Time evolution of T_p and T_e were determined by following set of equations

$$\frac{dT_p}{dt} = \nu_{pe}(T_e - T_p) \tag{4.2}$$

$$\frac{dT_e}{dt} = \nu_{ep}(T_p - T_e) - T_e A \tag{4.3}$$

where $A \simeq \frac{8}{B[\mathrm{T}]^2}$ is a synchrotron radiation cooling rate found experimentally[58]. Electrode walls are assumed to be sufficiently cold. Using Boltzmann constant(k_B), electronic charge(e), electron mass(m_e) and antiproton mass(m_p), equilibration rates (ν_{pe}, ν_{ep}) are given by

$$\nu_{pe} = \frac{e^4}{3\sqrt{2}\pi^{\frac{3}{2}}\varepsilon_0^2 k_B^{\frac{3}{2}}} n_e \lambda_{pe} \frac{m_p^{\frac{1}{2}} m_e^{\frac{1}{2}}}{(m_p T_e + m_e T_p)^{\frac{3}{2}}} \tag{4.4}$$

$$\nu_{ep} = \frac{e^4}{3\sqrt{2}\pi^{\frac{3}{2}}\varepsilon_0^2 k_B^{\frac{3}{2}}} n_p \lambda_{ep} \frac{m_p^{\frac{1}{2}} m_e^{\frac{1}{2}}}{(m_p T_e + m_e T_p)^{\frac{3}{2}}} \tag{4.5}$$

Fig.4.2 and Fig.4.3 are examples of calculations. Realistic experimental conditions are assumed : $B = 5$[T], $T_p(0) = 5.8 \times 10^7$[K](= 5000[eV]), $T_e(0) = 4$[K] , Coulomb logarithm[1] $\lambda_{ep} = \lambda_{pe} \sim 30$. For the calculation in Fig.4.2, $n_p = 10^8[\mathrm{cm}^{-3}]$, $n_e = 10^8[\mathrm{cm}^{-3}]$ were inputted and in Fig.4.3, $n_p = 10^8[\mathrm{cm}^{-3}]$, $n_e = 10^9[\mathrm{cm}^{-3}]$ were used.

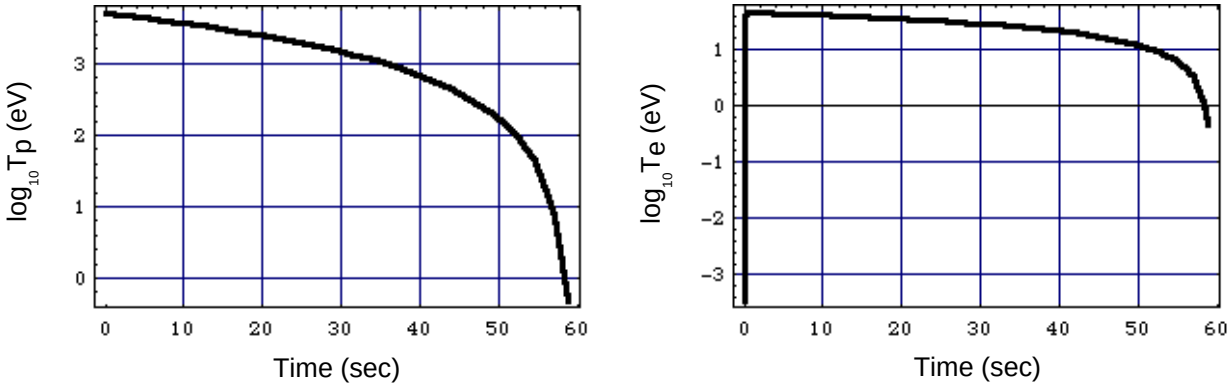

Figure 4.2: Calculation of electron cooling rate. ; $n_p = 10^8[\mathrm{cm}^{-3}]$, $n_e = 10^8[\mathrm{cm}^{-3}]$ are assumed.

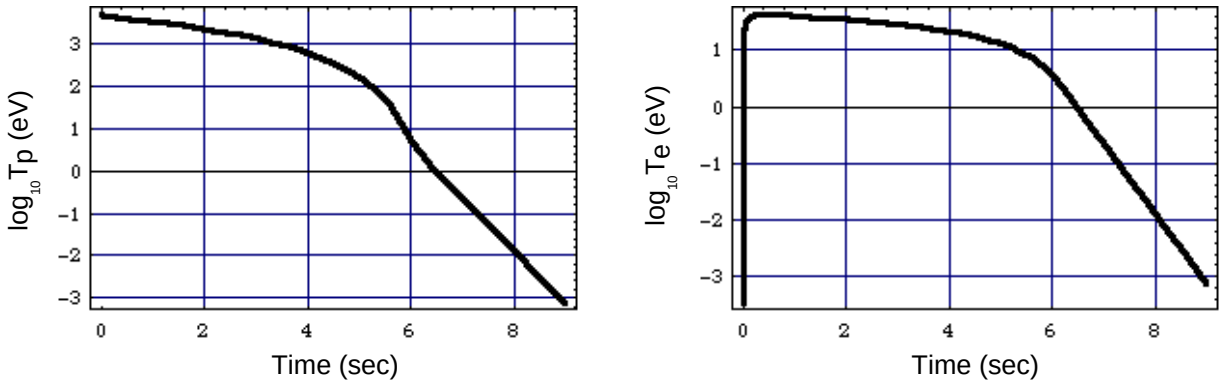

Figure 4.3: Calculation of electron cooling rate. ; $n_p = 10^8[\mathrm{cm}^{-3}]$, $n_e = 10^9[\mathrm{cm}^{-3}]$

[1]The definition is

$$\lambda = \ln \frac{\lambda_D}{a},$$

with the quantity a defined as $a \equiv \frac{e^2}{4\pi\epsilon_0 T}$ It is known that the collision frequency $\nu \sim n\pi a^2 v$ (n is the density of the collision partner.) multiplied by $\ln\Lambda$ approximately describes the effect of collisions that take place at a position farther than a (distant collisions)[73].

It can be seen that just after the injection, electrons are abruptly heated up by incoming hot antiprotons, and lose their energy via synchrotron radiation. Eventually both antiprotons and electrons will be cooled below 1 eV within one minute. We may note that the cooling time will be longer if we consider the anisotropy on the space and the temperature. Cooling time is thought to be optimized by adjusting the densities of two species.

4.3.1 Centrifugal separation of the cooled electron + antiproton plasma

As described in the Section 3.4.1, when multi species are contained in the same trap and cooled by some means, centrifugal separation would eventually occur[74]. Our main interest is the time scale for it to happen, which is still under study, by way of MD simulations, for example[75, 76].

4.4 Technical considerations

There were lots of challenges in the construction of the trap which should be located in an extreme environment like high magnetic field, low temperature, ultra-high vacuum. It is described in this section how those requirements were fulfilled.

4.4.1 Heat conduction

First, let us calculate the heat exchange by radiation. Suppose that there are two surfaces with different temperatures(T_H for higher and T_L for lower). For the surface with higher temperature and lower respectively, we can define the areas (A_H and A_L) and emissivities[2] ($\epsilon_H(T)$ and $\epsilon_L(T)$). Then the energy carried by radiation per unit time is given by the Stefan-Boltzmann's law :

[2]An emissivity is defined at a frequency ν as the ratio of a emissive power from a surface of an object with temperature T to the one from the surface of a black body of the same temperature :

$$\epsilon_\nu(T) \equiv \frac{e_\nu(T)}{e_{b\nu}(T)},$$

which is called a monochromatic emissivity. When it is not necessary to specify the frequency, we have

$$\epsilon(T) \equiv \frac{e(T)}{e_b(T)}.$$

Generally speaking, emissivity is a decreasing function of temperature and a smooth surfaces has a smaller emissivity.

$$\frac{dQ}{dt} = \sigma A_L E \left(T_H^4 - T_L^4\right) \tag{4.6}$$

Here, σ is Stephan-Boltzmann constant. E is a net emissivity defined as

$$E = \frac{1}{\left(\frac{1}{\epsilon_L(T_L)}\right) + \left(\frac{A_L}{A_H}\right)\left\{\left(\frac{1}{\epsilon_H(T_H)}\right) - 1\right\}} \tag{4.7}$$

and we took the grey surface approximation, *viz*, the emissivities were assumed to be independent of both frequency and direction.

Now take an outer surface of the trap to be at T_H and the inner surface of the bore tube at T_L as an example. By further assuming that the heat capacitance of the electrode, C, is constant in the temperature range of interest, we may write the Eq. (4.6) as

$$\frac{dT_H}{T_H^4 - T_L^4} = \frac{\sigma A_L E}{C} dt. \tag{4.8}$$

Integrating Eq.(4.8) we have

$$-\int_{T_H}^{T_L} \frac{dT_H}{T_H^4 - T_L^4} = \frac{\sigma A_L E}{C} \int dt. \tag{4.9}$$

Taking the values $T_H = 300$ K, $T_L = 4$ K, $\sigma = 5.7 \times 10^{-12}$ [W cm^{-2} K^{-4}], we can estimate the time for T_H to be 10 K is in the order of 10^{11} sec, which means that the temperature change due to radiation is negligible. Using the trap geometry shown in Fig.4.4, we can thus neglect Q_2. For initially hot electrodes to be cooled down to the ambient cryogenic temperature, thermal contact is necessary.

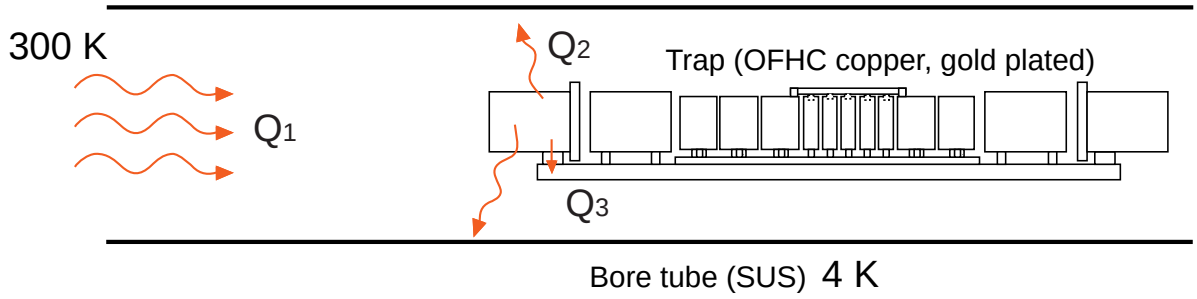

Figure 4.4: Geometry of trap electrode in a cylindrical bore tube.

On the other hand, suppose that the electrodes are initially cooled. Using Stefan-Boltzmann's law, we can also estimate the heating effect (Q_1 in Fig.4.4) by the radiation from outside. The most serious part is the outermost GND electrode since others are

shielded by this. We now know that radiation from the surface of the electrode does not help, heat flow through the base plate (Q_3) should compete with heat from outside. Assuming that there is a 300 K radiator at the end of the bore tube[3] and the heat capacitance of the bore tube (4 K) is infinitely large. From Eq.4.6, Q_1 is estimated to be in the order of 10^{-2} W, while Q_3 is approximately given by $10^{-4}A$ W/K. Here, A cm^2 is the contacting area between the GND electrode and the base plate. Making A to be about 10 cm^2, temperature rise below 10 K can be realized. The contact area was designed to be about 9 cm^2 For all the other electrodes, there yet exist another heat source, which is cables. Their effect are given in Sec.4.6.1, which is also tolerable.

4.4.2 Material selection

The material used in the trap should be : (1) ultra-high vacuum compatible, (2) usable in cryo temperature, (3) bakable, and (4) non-magnetic.

As a non-magnetic, ultra-high vacuum compatible material, we decided to use copper to make electrodes. All the electrodes are made of OFHC copper (C1020), which is known to be usable in cryogenic environment, with the machining precision of 20 μm and gold plated with the thickness enough to improve the surface property, namely to prevent the oxidation, while the precision is tolerable. Machining was done after the removal of stress by annealing. They are aligned on a base plate which is machined with the same precision. Especially great care was taken for the base and the segmented electrode so as not to introduce field asymmetry.

Aluminum nitride (AlN ; Tokuyama SH10) used as insulators has high thermal conductivity, higher than normal AlN and, *e.g.*, a few times more than that of deoxidized copper. It was ideal to have as much heat conduction as possible while keeping electric insulation. In other places where only insulation is necessary, Macerite HSP(Mitsui Mining Material Co.,Ltd.) was used. Its thermal conductivity is two order of magnitude smaller than that of AlN as listed in Table 4.2.

In Table 4.2, thermal properties of various materials are summarized.

[3]since thermal shield exists at the end, this is an over estimation.

Material	Specific heat [J·g^{-1}·K^{-1}]	Thermal conductivity [W·m^{-1}·K^{-1}]	Coefficient of linear expansion [K^{-1}]	Emissivity
OFHC copper (C1020)	0.385 (RT) 0.195 (77K)	391 (RT) 482 (100K) 16200 (4K)	17.7 $\times 10^{-6}$ (RT) 18.3 $\times 10^{-6}$ (RT $\rightarrow$ 1273K)	0.02 (50 - 100K)
Deoxidized copper		220 (RT) 120 (77K) 7.5 (4K)		0.038 - 0.06 (RT)
Phosphor bronze			17.0 $\times 10^{-6}$ (RT)	
Beryllium copper 98% Cu, 2% Be		90 (273K) 36 (77K) 2 (4K)		
SUS304	0.555 (RT)	14 (273K) 8 (77K) 0.3 (4K)	11.4-14.7 $\times 10^{-6}$ (RT)	0.35(500K)
SUS316		16.3 (373K)		
Al	1.00 (RT) 0.336 (77K)	237 (RT) 302 (100K) 15700 (4K)	23.1 $\times 10^{-6}$ (RT) 12.2 $\times 10^{-6}$ (100K)	0.01 - 0.06 (RT)
Au	0.135 (RT) 0.097 (77K)	317 (RT) 327 (100K) 209 (4K)	14.2 $\times 10^{-6}$ (RT) 11.8 $\times 10^{-6}$ (100K)	0.01 - 0.03 (foil;RT)
Ag	0.249 (RT) 0.162 (77K)	429 (RT) 450 (100K) 14700 (4K)	18.9 $\times 10^{-6}$ (RT) 14.2 $\times 10^{-6}$ (100K)	0.02 - 0.03
Macerite HSP	0.80 (RT)	1.7 (RT)	9.8 $\times 10^{-6}$ (RT $\rightarrow$ 473 K)	
AlN (SH10;Tokuyama)		200 (RT) 500 (100K) 15 (4K)	8.0 $\times 10^{-6}$	
Al_2O_3 (99.5 %)	0.8	25 - 30 (RT)	8.0 $\times 10^{-6}$	

Table 4.2: Thermal property of materials.

In Table 4.3, physical and electrical properties of various materials are summarized.

Material	Density [g·cm^{-3}]	Volume resistivity [Ω·m]	Dielectric constant	Dielectric strength [kV·mm^{-1}]
OFHC copper (C1020)	8.93	1.71 $\times 10^{-8}$ (RT) 3.5 $\times 10^{-9}$ (100K) 2.0 $\times 10^{-11}$ (10K)	-	-
Beryllium copper	8.2			-
SUS304	7.8	7.2 $\times 10^{-7}$ (RT)	-	-
SUS316	7.98	7.4 $\times 10^{-7}$ (RT)	-	-
Al	2.69	2.7 $\times 10^{-8}$ (RT) 4.4 $\times 10^{-9}$ (100K) 1.9 $\times 10^{-12}$ (10K)	-	-
Au	19.3	2.2 $\times 10^{-8}$ (RT) 6.5 $\times 10^{-9}$ (100K) 2.3 $\times 10^{-10}$ (10K)	-	-
Ag	10.5	1.6 $\times 10^{-8}$ (RT) 4.2 $\times 10^{-9}$ (100K) 1.2 $\times 10^{-11}$ (10K)	-	-
Macerite HSP	2.67	4.8 $\times 10^{13}$ (RT)	6.5 (1MHz)	15
AlN (SH10;Tokuyama)	3.3	$> 10^{12}$ (RT)	8.5 (1MHz)	> 15
Al_2O_3	3.8	$> 10^{12}$ (RT)	10.2 (1MHz)	12

Table 4.3: Physical and electrical property of materials.

4.4.3 Temperature rise in the case of magnet quench

If the magnet quenches, change in magnetic flux cause an azimuthal current. From the Maxwell's equation,

$$\nabla \times \mathbf{E} = -\frac{\partial \mathbf{B}}{\partial t} \tag{4.10}$$

If we assume a magnetic field of an infinitely long solenoid, we can rewrite Eq.(4.10) using cylindrical coordinate(r, ϕ, z). Taking the field axis in the z-direction,

$$\frac{1}{r}\left[\frac{\partial}{\partial r}(rE_\phi) - \frac{\partial E_r}{\partial \phi}\right]\hat{\mathbf{z}} = -\frac{\partial B_z}{\partial t}\hat{\mathbf{z}} \tag{4.11}$$

Neglecting the second term in Eq.(4.11) since we are interested in the azimuthal current, together with a constant change rate of the magnetic field strength,

$$\frac{1}{r}\frac{\partial}{\partial r}(rE_\phi) = -\frac{\partial B_z}{\partial t} \equiv a = const. \tag{4.12}$$

Now let us take a geometry like Fig.4.11 and integrate Eq.(4.12) from the inner diameter r_1 to the outer diameter r_2. Further assuming that $E_\phi(r_1) = E_\phi(r_2) \equiv E_\phi$, we have

$$E_\phi = -\frac{a}{2}(r_1 + r_2). \tag{4.13}$$

From Ohm's law $\mathbf{J} = g\mathbf{E}$, we can write

$$J_\phi = gE_\phi \tag{4.14}$$

in our case. Hence

$$J_\phi = gE_\phi = -\frac{ag}{2}(r_1 + r_2). \tag{4.15}$$

Our magnet can be de-energized approximately at the rate of 0.03 [Ts^{-1}]. Putting the values listed in Table 4.2 and Table 4.3 with the dimensions in Fig.4.9 and Fig.4.11, we can estimate that the temperature will increase 0.04 K, which is no problem.

By following the same way temperature change of the support ring was estimated to be 6.7 K. This value corresponds to a radial expansion of 20 μm, which is also within the tolerance.

4.5 Control system

Since the whole set up will be installed inside the AD ring, there will be little possibility to access the experimental area during the experiments. This is why almost all the apparatus are remotely controlled. Labview + GPIB control scheme is used.

4.5.1 Electronics

Voltages on the trap electrodes were controlled by amplifying the output of a signal generator (NF 1946) using a fast operational amplifier (PA85) with a slew rate of 200 V/sec. Output range is $\pm$150 V. The circuit diagram is shown in Fig.4.5.

Catching the energetic antiprotons ($\sim$ 10 keV) which enter a trap as a bunch of 250 nsec requires fast voltage switching on the entrance high voltage electrode. For an 10 keV-antiproton, traveling time for a bounce from the entrance HV electrode (HVF in Fig.4.8) to the exit HV electrode (HVB in Fig.4.8) becomes 700 ns. Considering that we want to catch tail antiprotons, we can sets the upper limit of the rise time as 450 ns. A thyratron (EG&G ; 7322) is used for this purpose. (Fig.4.6 for $\overline{\mathrm{p}}$ or H^- and Fig.4.7 for proton trapping). a TTL pulse triggers the thyratron and a fast rising high voltage is applied to the HVF electrode. Typical rise time is about 100 ns. After several msec, thyratron is replaced by a high voltage power supply (MATSUSADA ; HWR-25N or -25P) to maintain the high voltage.

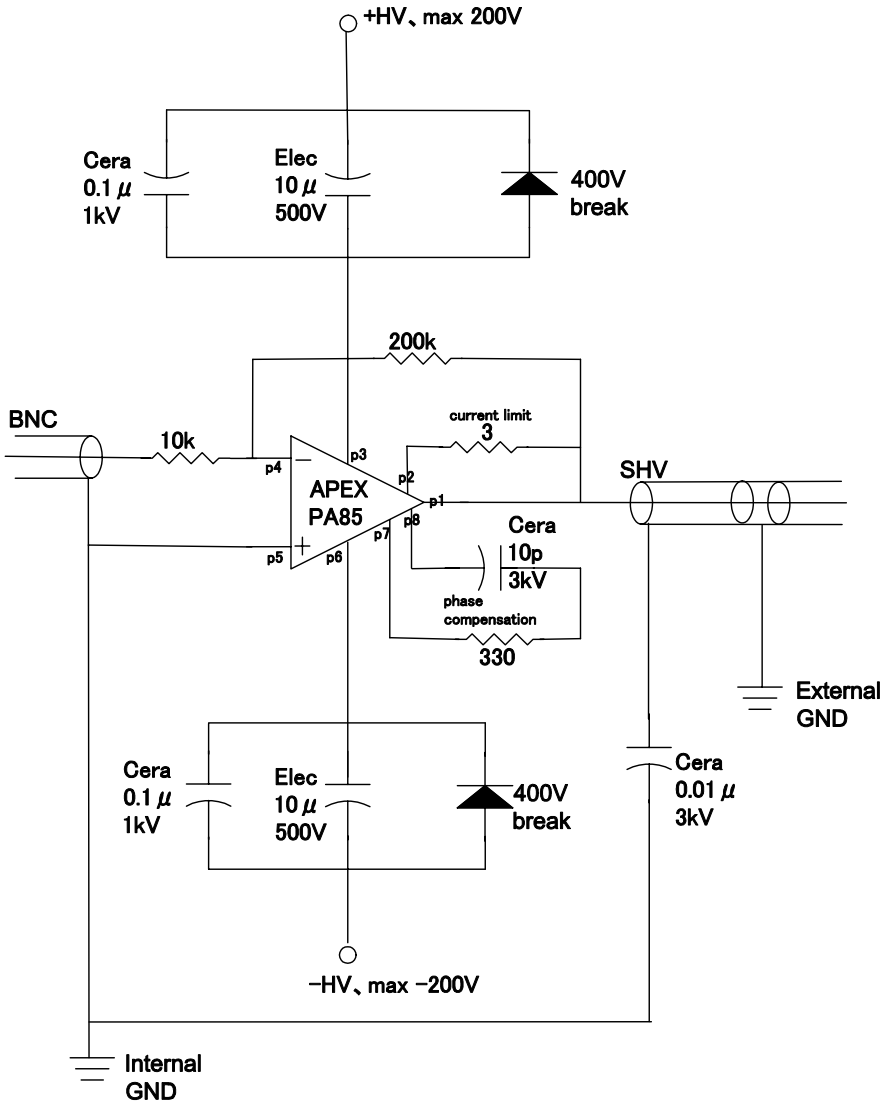

Figure 4.5: Amplifier for the control of trap electrodes.

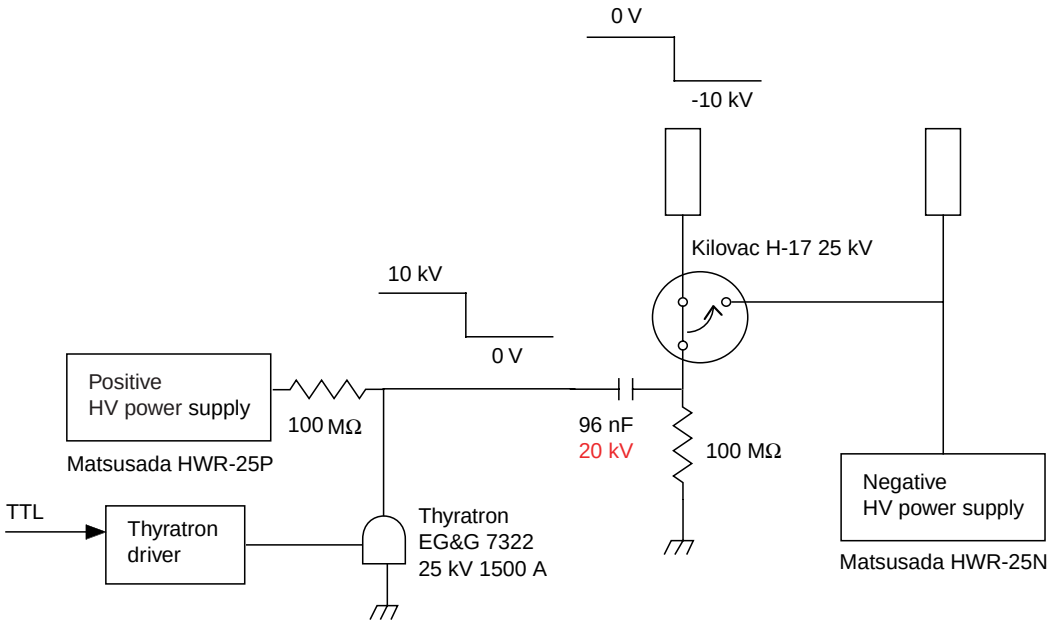

Figure 4.6: High voltage electrode control scheme ($\overline{\text{p}}$ or H^- operation).

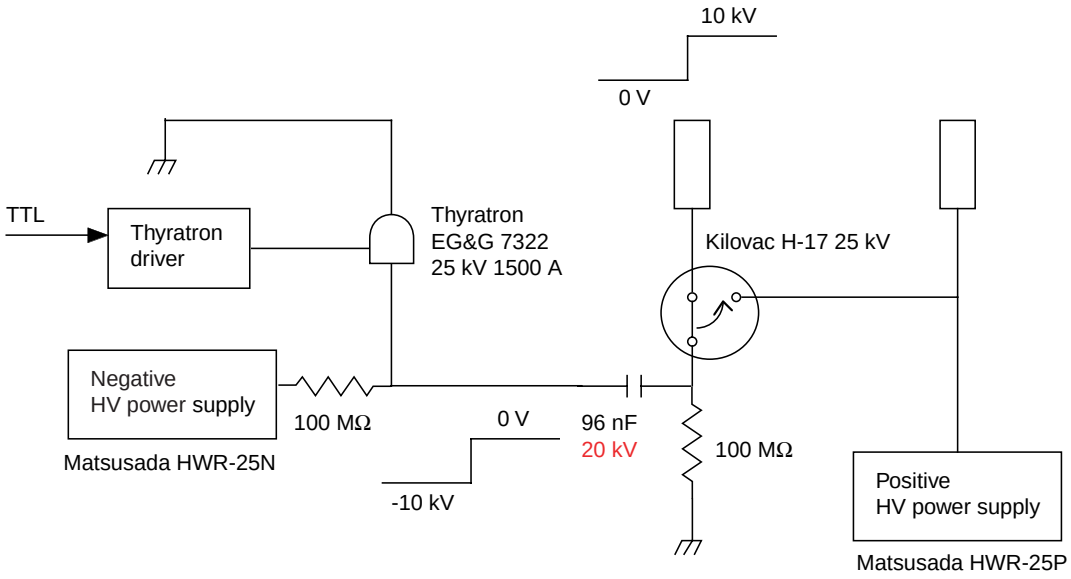

Figure 4.7: High voltage electrode control scheme (proton operation).

4.6 ASACUSA Trap assembled

In Fig.4.8, the configuration of the trap electrodes is given. Central harmonic region is created by five electrodes (FH2-BH2). One of them (S) is azimuthally segmented into four identical parts for the application of rotating electric field. F1 and B1 are to define the end of the harmonic region. They are longer than F2, F3, and B2 so as to prevent the outer field come into the harmonic region. Two electrodes, "HVF" and "HVB" are to capture energetic antiprotons from RFQD.

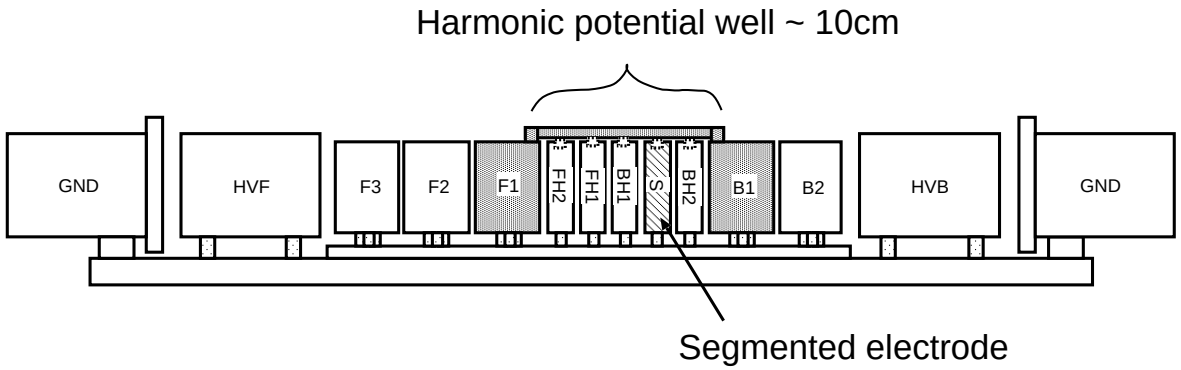

Figure 4.8: Configuration of trap electrodes. "HVF" and "HVB" are to capture energetic antiprotons from RFQD. Central harmonic region is created by potentials given on five electrodes (FH2-BH2). One of them (S) is azimuthally segmented into four identical parts.

Fig.4.9 is a precise drawing of the trap with dimensions.

Fig.4.11 shows how the trap is installed in a bore tube. To ensure sufficient thermal contact between the electrodes and insulators, silver foils (thickness $\sim 10 - 20\mu$m) were inserted in-between. Furthermore, a Multilam band (Multi-Contact ; type LAI) was attached along the outer circumference of each support ring. This band has many torsion spring contacts made of silver-plated copper beryllium, which is normally used to make electrical contact between two surfaces where large current flows.

We put a Rh-Fe sensor (27 Ω at RT) to monitor the temperature of the trap (Location is shown in the Fig.4.11). The temperature change during the cooling down of the magnet is shown in Fig.4.10. The discrepantly in the low temperature region seems to result from the cabling of the thermometer. Though four wire resistance measurement technique was used, the resistance of wires seems affected the reading. Anyway, it was confirmed that the temperature of the trap follows the temperature of the bore tube with a time delay of several hours.

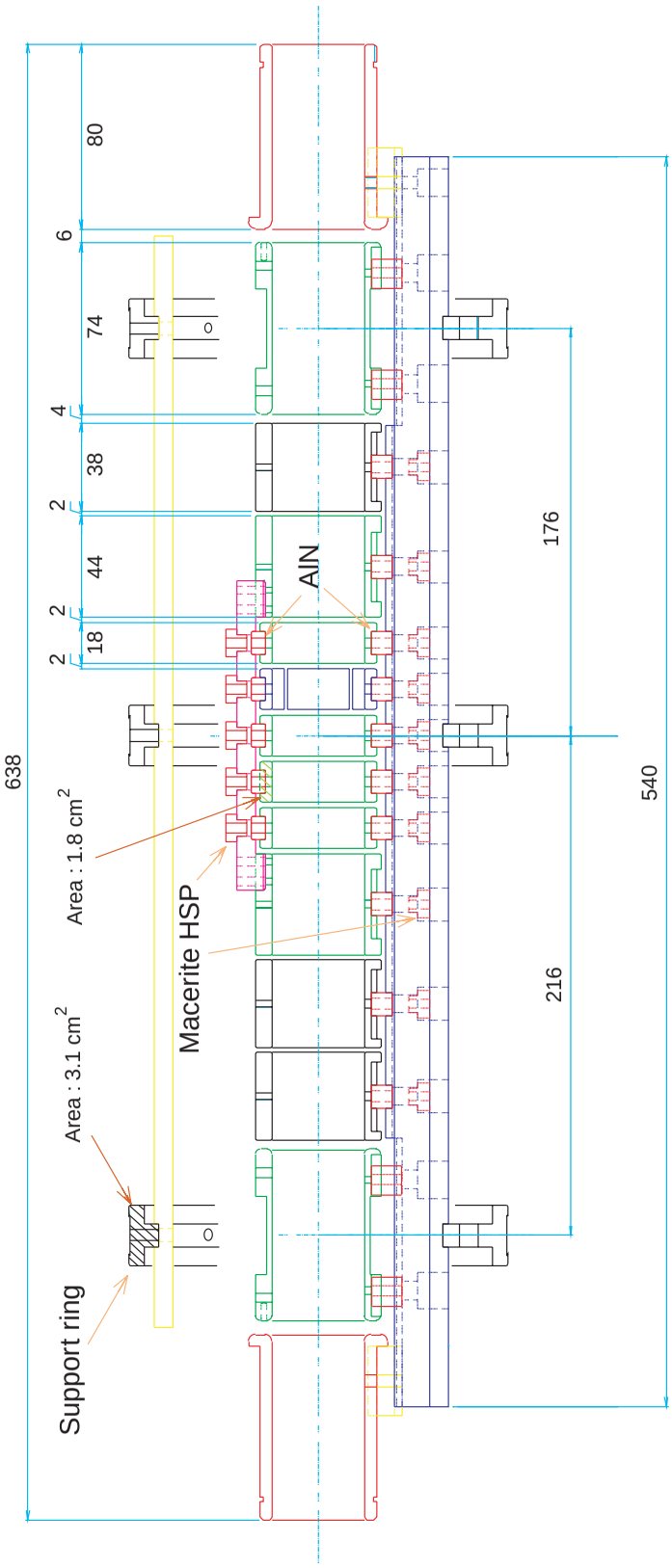

Figure 4.9: Configuration of electrodes ; side view

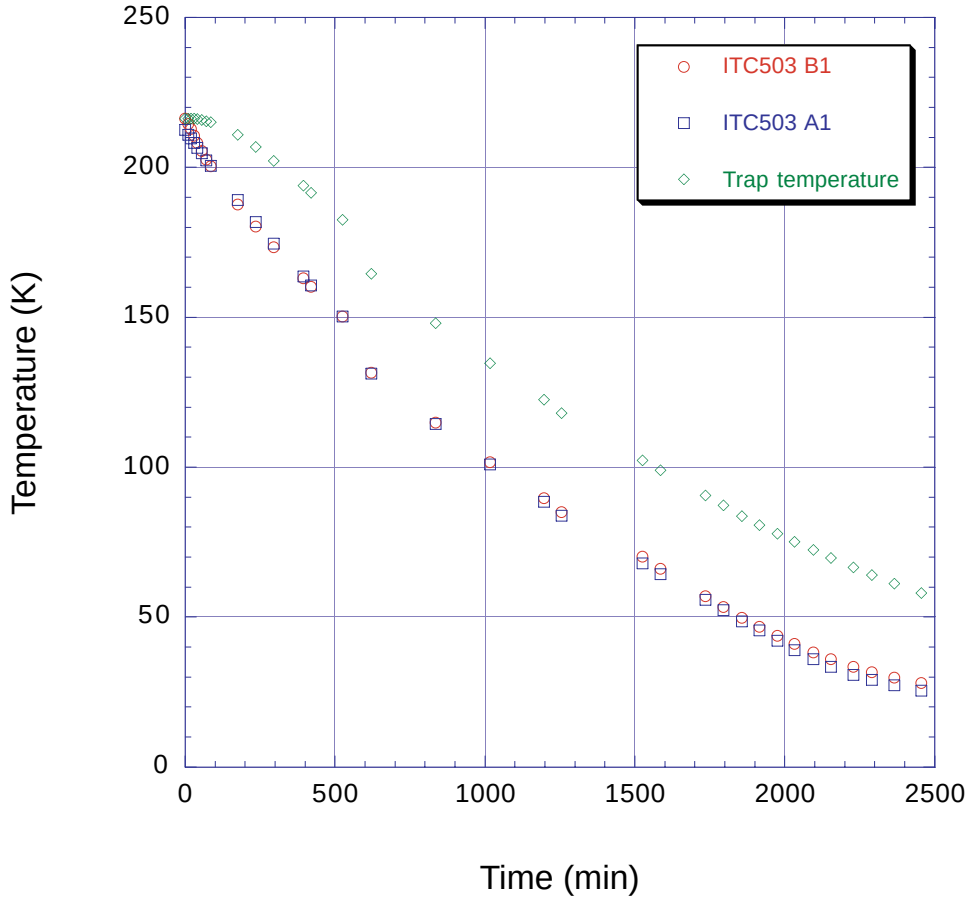

Figure 4.10: Heat transport measurement during the cooling down of the bore tube. ITC503A and ITC503B are thermometers located on the bore tube, near the trap. The discrepancy between the trap temperature and the bore tube temperature (readings of ITC503) in the low temperature region comes from the resistance of the wire which connects the RhFe sensor to the controller.

Fig.4.12 is a picture of the assembled trap. For demonstration, one of the segments of the azimuthally sectored electrode is detached with its support bar.

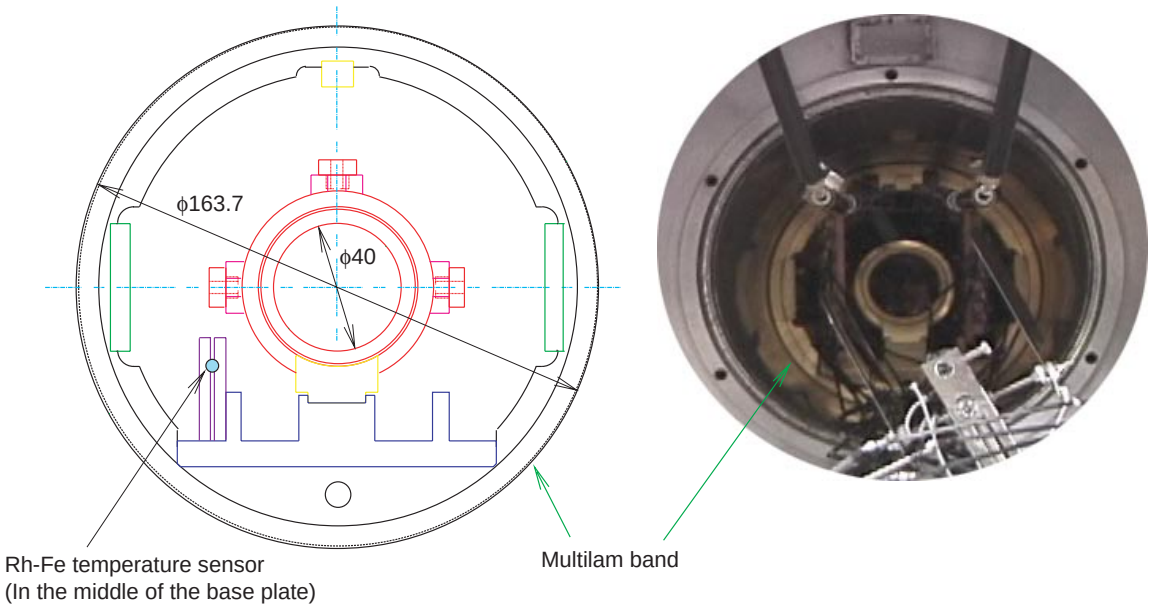

Figure 4.11: Structure of the trap support ; axial view

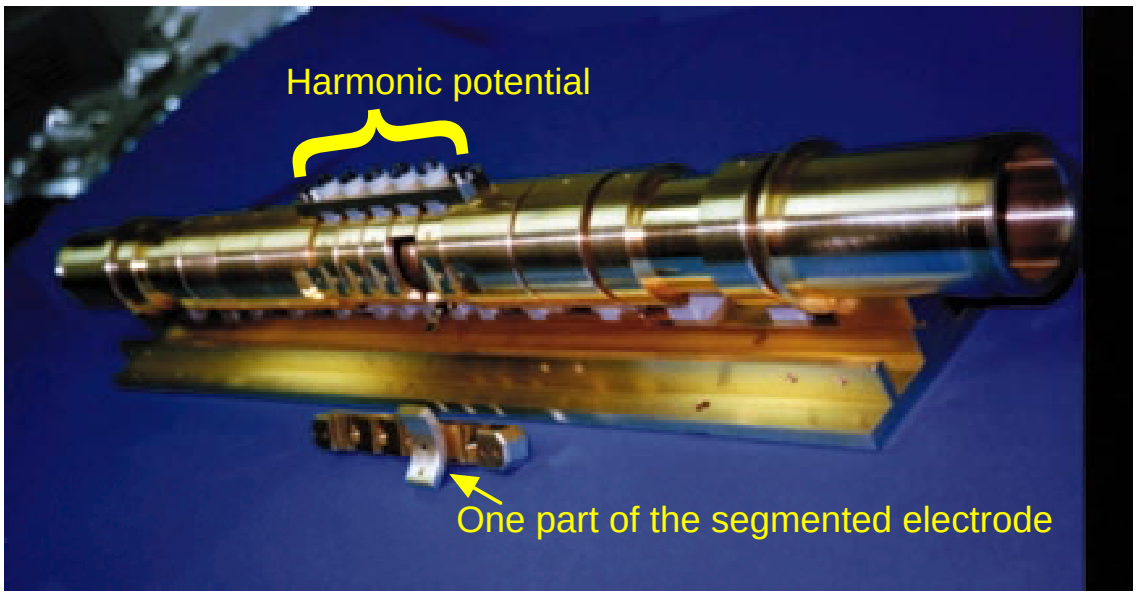

Figure 4.12: Picture of the ASACUSA trap.

4.6.1 Cabling

Cables used to supply powers and to detect signals were designed to fulfill the following conditions.

1. Shielding was definitely necessary. For the observation of plasma modes, detection of faint induced current requires it and for the HV cables, it prevents the induction on signal cables.

2. Materials should not affect the magnetic field and at the same time should be ultra-high vacuum compatible. Operation under the liquid He temperature is necessary.

3. In addition to the radiation considered in Section 4.4.1, heat transport due to cables in never negligible. To minimize the heat load to the bore tube, lower heat conduction was preferable.

Together with the conditions above, for signal cables, a SUS304 wire of 0.2 mm in diameter + thin alumina pipes and bises surrounded by SUS304 tubes (ϕ2, t0.15) are used. Outer tubes were connected to each other by spot welding. Thermal conductivity is anticipated to be less than 10 $\mu\mathrm{Wm}^{-1}\mathrm{K}^{-1}$. Structure of the HV cable is schematically shown in Fig.4.13. Thermal conductivity is anticipated to be less than 10 $\mu\mathrm{Wm}^{-1}\mathrm{K}^{-1}$ for signal cables and less than 300 $\mu\mathrm{Wm}^{-1}\mathrm{K}^{-1}$ for HV cables. Total heat flow through a HV cable is less than 3×10^{-4} W K^{-1}, which is comparable to the radiation from outside given in Sec. 4.4.1.

Fig.4.14 is a picture of the installed trap and cables, taken from the downstream end of the bore tube.

4.7 Vacuum requirements

For simplicity, suppose that trapping by electric and magnetic fields are complete so that the lifetime of antiproton plasmas is decided by annihilation with residual gases. Let us assume that antiprotons (1000 K in energy) are confined in the ambient temperature of 10 K. As an annihilation cross section, we may use 10^{-16} cm^2, which is a typical formation cross section of antiprotonic atoms. The condition that antiprotons should survive 1000 sec in the trap gives a constraint that the base pressure should be less than 10^{-13} Torr.

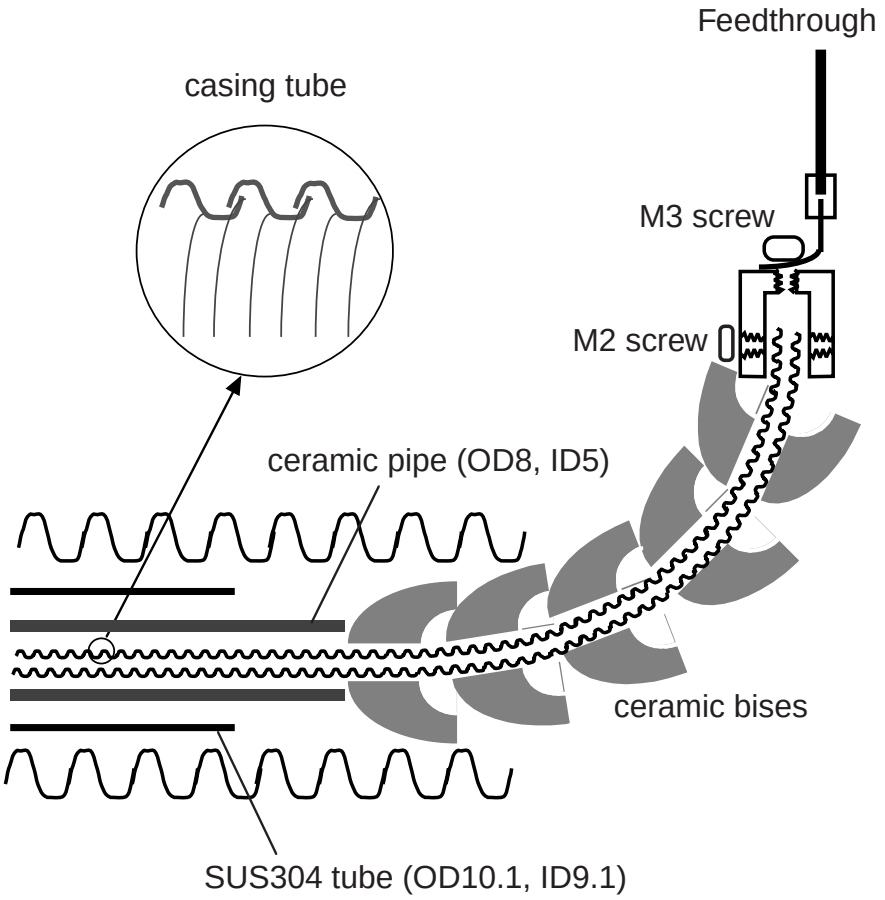

Figure 4.13: Structure of the cable for high voltage application. Straight parts where there is no necessity of flexibility were thoroughly covered by SUS304 tubes.

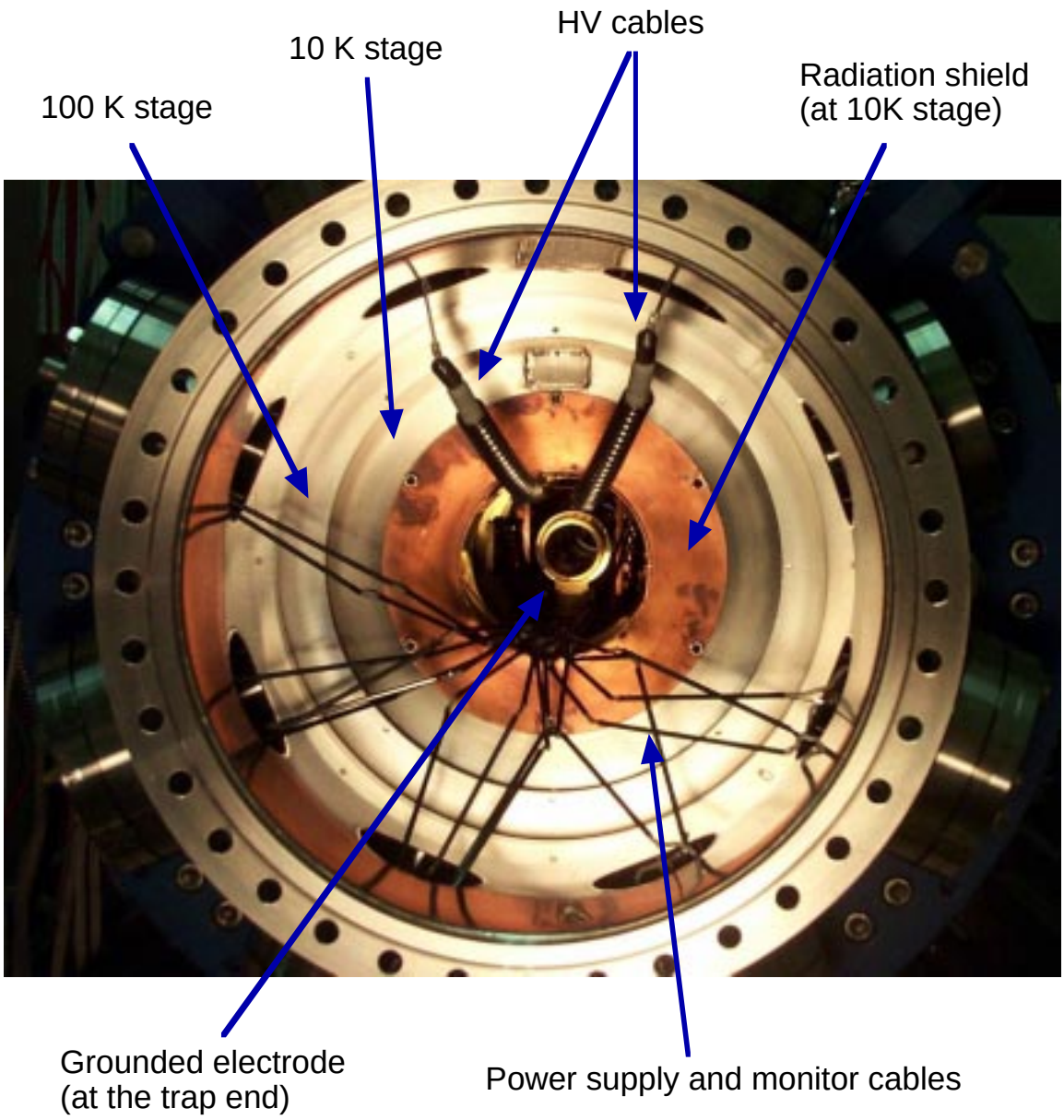

Figure 4.14: ASACUSA trap inside the bore tube.

4.7.1 Vacuum system

Turbomolecular pumps + Rotary pumps are used for the evacuation of the system. Since the bore tube will be cooled, the main component of the residual gas is hydrogen. (Consult Fig.4.15, vapor pressures of various materials vs. temperature are drawn.)

To gain the compression ratio, an extra 70 ℓ/sec turbomolecular pump was inserted between the rotary pump and the two turbomolecular pumps attached to the bore tube part. (Actual positions are schematically shown in Fig.5.1.)

At the entrance of the magnet, a 300 ℓ/sec ion pump (Varian Triode) is attached to keep the low pressure. Since around 4 K, most of the evacuation power would come from the cryogenic bore wall (cryopump!), one gate valve is located at the head of each turbomolecular pump so that we can disconnect it from the main chamber.

4.8 Superconducting solenoid

Magnetic field for the confinement of particles is another key to the trapping of particles. A superconducting solenoid manufactured from ultra fine NbTi filament was constructed. Drawing is shown as Fig.4.16.

4.8.1 Specifications

Below are the specifications of the superconducting magnet, which fit our requirements.

Field strength

The maximum field strength is 5 T. The strength is variable at the speed of 0.03 T/sec.

Field uniformity

In addition to the main solenoid, compensation coils are placed so that the field uniformity is guaranteed to be within $\pm 0.5\%$ over the region of 1100(length) $\times$ 10(diameter). Of course the trapping region is smaller than this and the field would be less distorted there.

Cryostat

Cryostat consists of two parts, one small reservoir fitted around the coil and the main large container of liquid helium located above the coil.

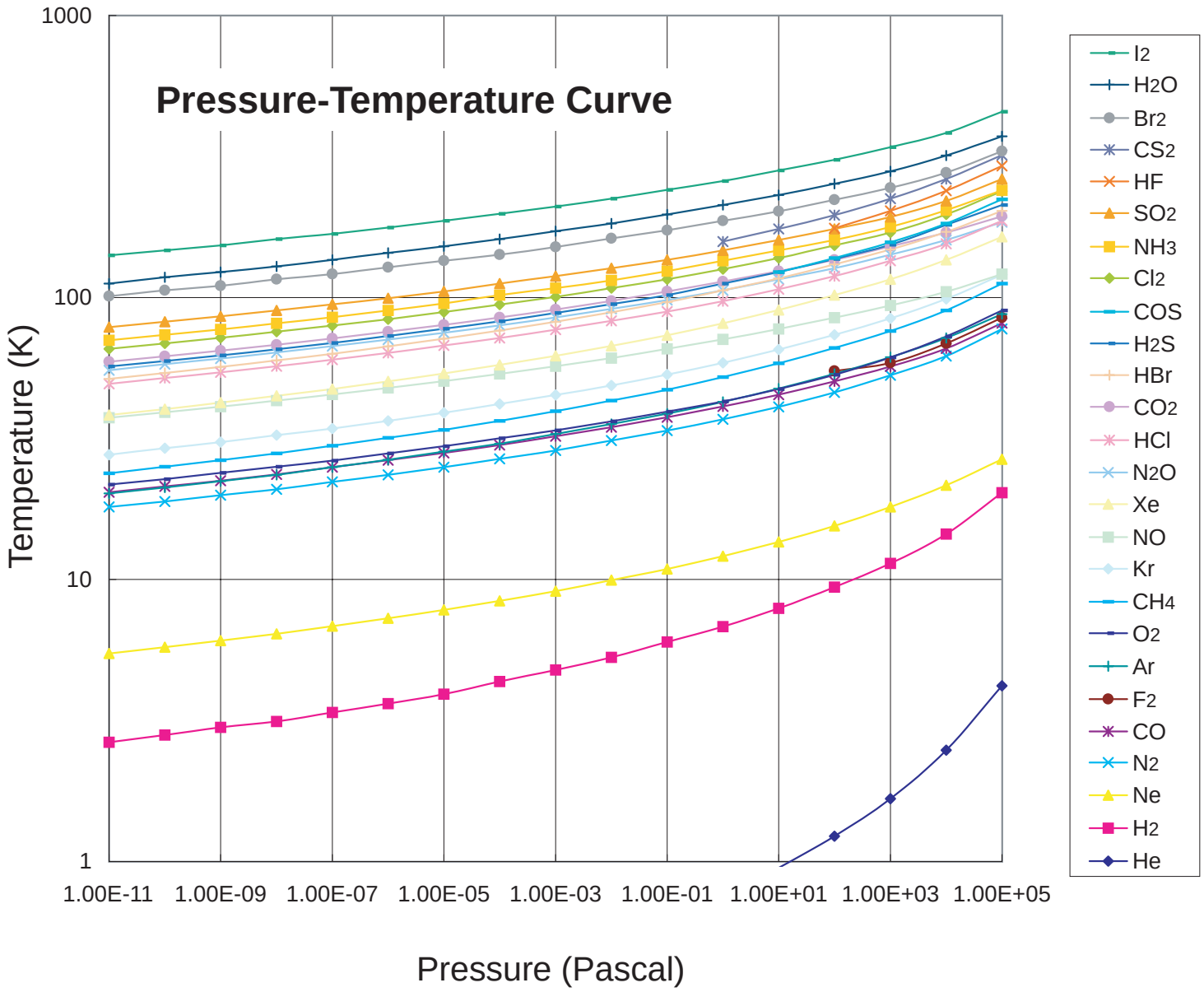

Figure 4.15: Vapor pressure vs. temperature.

Bore tube

It is essential for the experiments of antimatter to keep the pressure as low as possible. The bore tube made of SUS304 is bakable up to 420 K and can be operated at 3.5 K.

Alignment of the trap axis

Whenever there is an electric field non-parallel to the magnetic field, $\mathbf{E} \times \mathbf{B}$ drift occurs. Apart from the field asymmetry comes from the structure, we can minimize the cross product by aligning the electric field axis to the magnetic field line. The bore tube is connected to the end flanges via nested bellows so that its position can be changed. Adjustment of ± 2 mm is possible on both ends in 1μm steps with stepping motors.

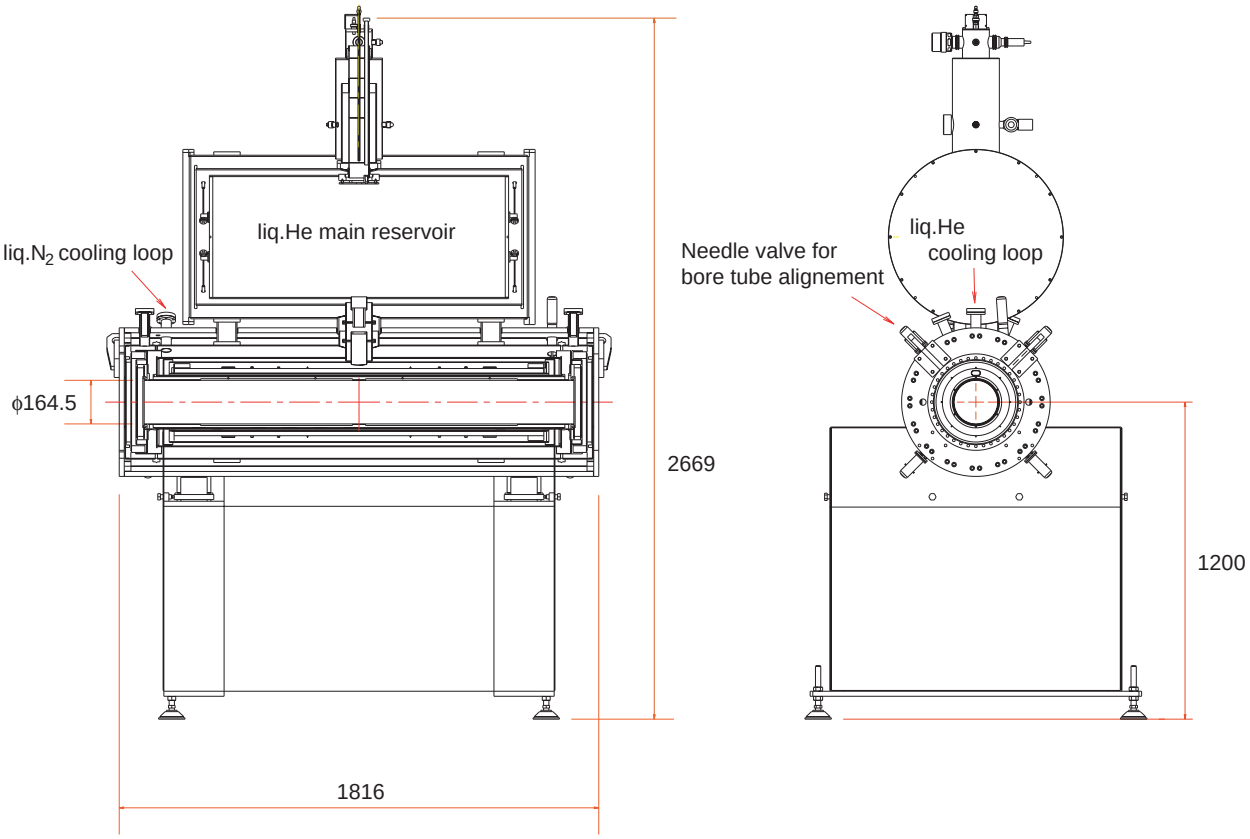

Figure 4.16: Structure of the superconducting solenoid

Below, in Fig.4.17 and Fig.4.18, calculated field profiles are drawn to show the shape of the fringing field.

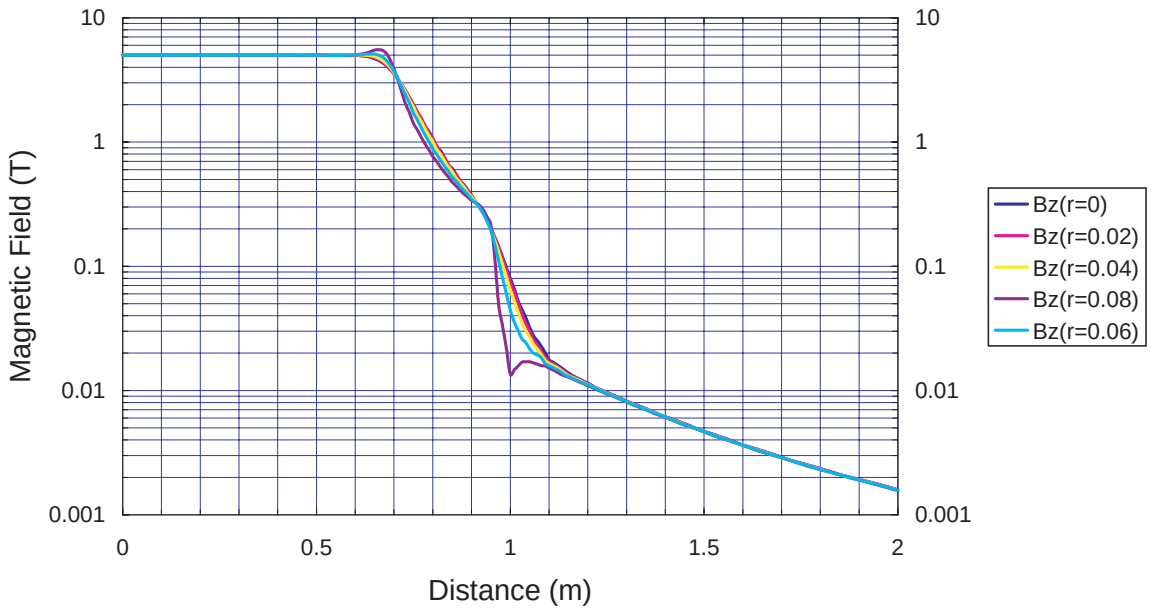

Figure 4.17: Magnetic field map with iron shields (axial direction). The origin of the distance is the center of the solenoid.

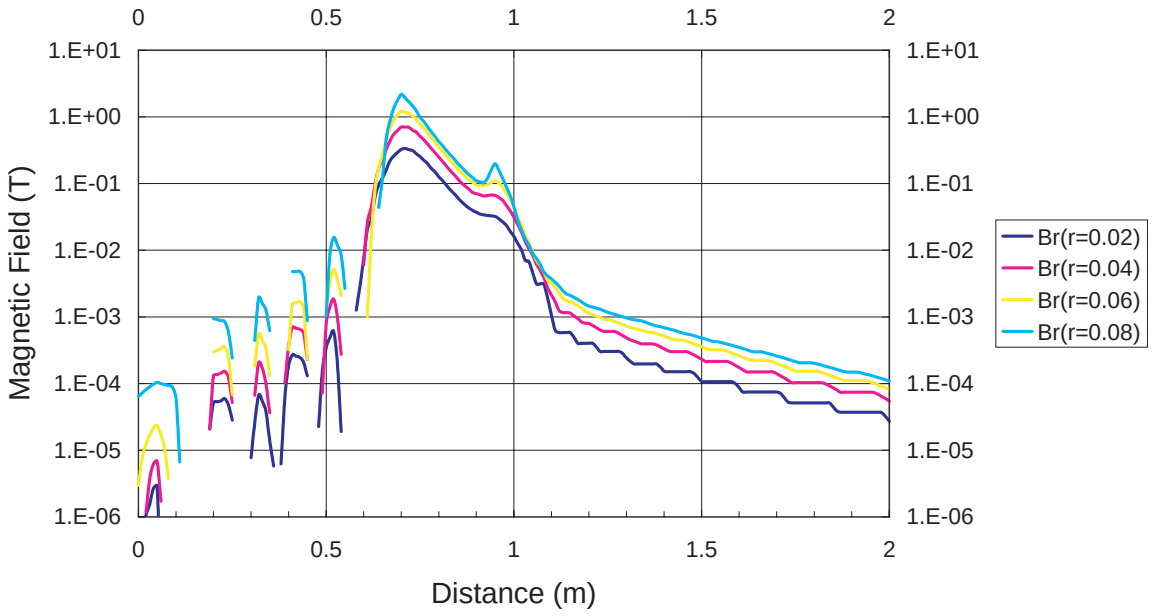

Figure 4.18: Radial field map with ion shields.

Chapter 5

Experiments

Since antiprotons cannot be easily obtained, protons and negative hydrogen ions are selected to simulate antiprotons. To apply electron cooling technique, H^- ions are preferable since we can confine them in the same region as electrons. The disadvantage is that a negative hydrogen has only bound state and corresponding ionization potential is as shallow as 0.75 eV. This sets an upper limit not only on the beam energy to be 1.4 keV, but also on the pressure in the trap region (See Sec.5.6). To try to capture higher energy particles, protons will be the best species. In Table 5.1, these discussions are summarized.

	Protons	H^- ions	Antiprotons
Characteristics	simple	composite (binding energy $\sim$ 0.75eV)	simple
Charge	$+e$	-e	-e
Mass	m_p	$1.001m_p$	m_p
Purpose	$\star$ capture of energetic particles $\star$ radial compression $\star$ extraction	$\star$ electron cooling	

Table 5.1: Characteristics of protons and H^- ions compared with antiprotons.

All the experiments except the measurement of the dependence of lifetimes of electron plasmas on the magnetic field were done under the magnetic field of 1T.

5.1 Experimental setup

In Fig.5.1, experimental setup is shown.

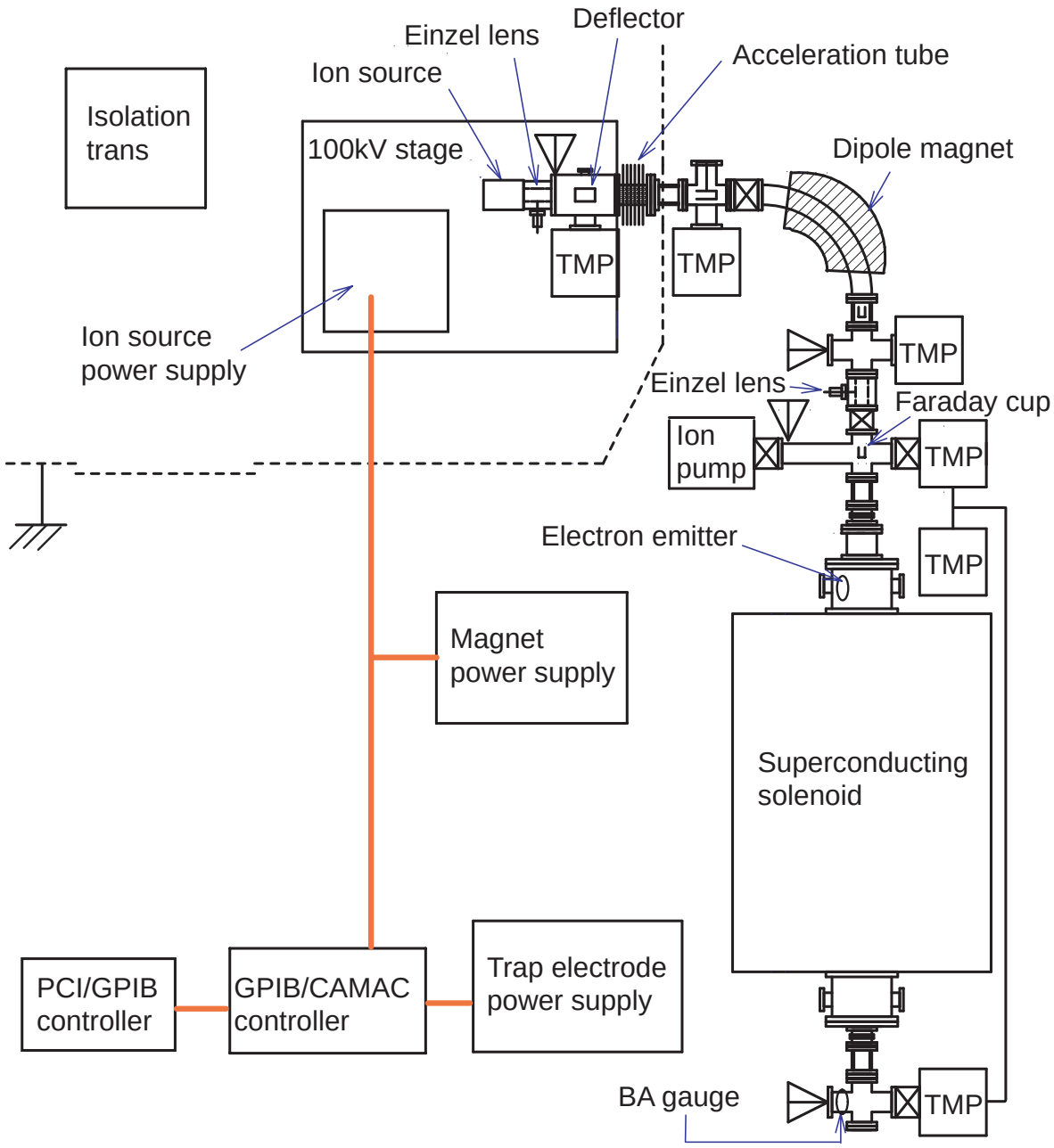

Figure 5.1: Beamline for proton or H^- injection. The deflector is used for pulsing of ion beams. Desired species is selected by the dipole magnet. All the system is evacuated by turbomolecular pumps and rotary pumps for roughing. A BA type ion gauge is placed at the end of the beamline to monitor the pressure.

There is a set of deflector to chop the beam. The desired ion species were selected by a dipole magnet. This beamline was designed so that we can have protons up to 100keV, with the pulse width of 200 nsec. A BA-type ion gauge was used to monitor the pressure of the bore tube in which the trap is installed, but it is located at the room temperature position.

In the rest of this section, descriptions of some components are given.

5.1.1 Spindt emitter

Generation of electrons was done by a Spindt emitter, a microfabricated field emitter array. Our requirements for the electron gun were cold emission and no heat load, small size and high current density, low voltage operation and compatibility with ultra-high vacuum. As is shown in Fig.5.2, a standard Spindt emitter consists of arrays of molybdenum tips ($\sim 1\mu$m)[77], total area covers 1 mm^2. The whole emitter array is mounted on a commercial TO-5 header.

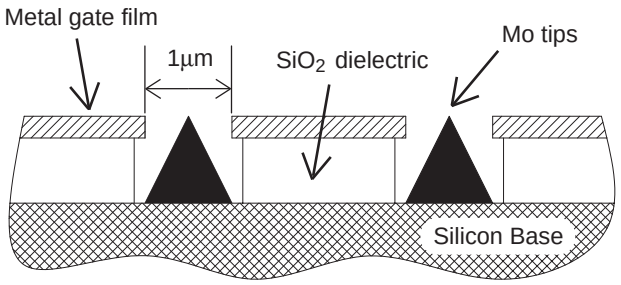

Figure 5.2: Structure of the Spindt emitter array

Fig.5.3 and Fig.5.4 show SEM images of the emitter.

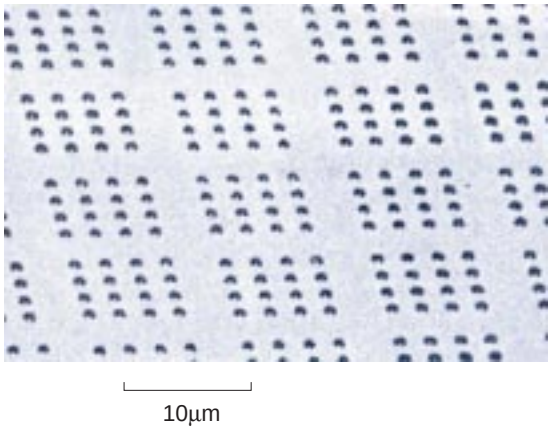

Figure 5.3: SEM micrograph of Spindt emitter array

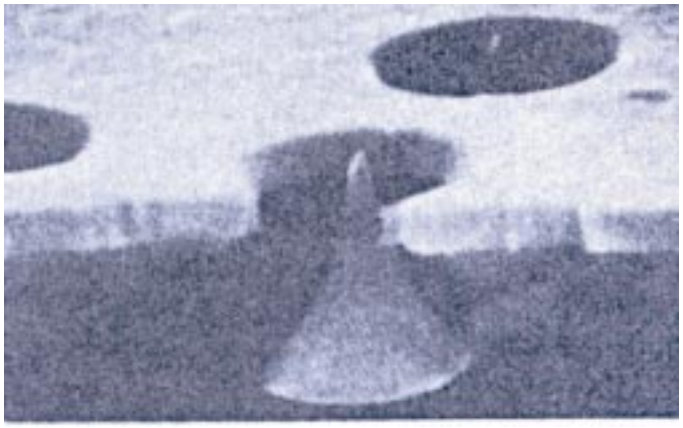

Figure 5.4: SEM micrograph of Spindt emitter array

The same combination of a Multi-ring trap and field emitter arrays is used in another experiment at Kyoto university[78].

The emitter was installed on the upstream side of the magnet (Fig.5.1), where the magnetic field strength is a few hundred gauss when we have 1T in the middle of the bore. We attached it on a linear feedthrough so that we can change the radial position. Its control circuit is given in Fig.5.5.

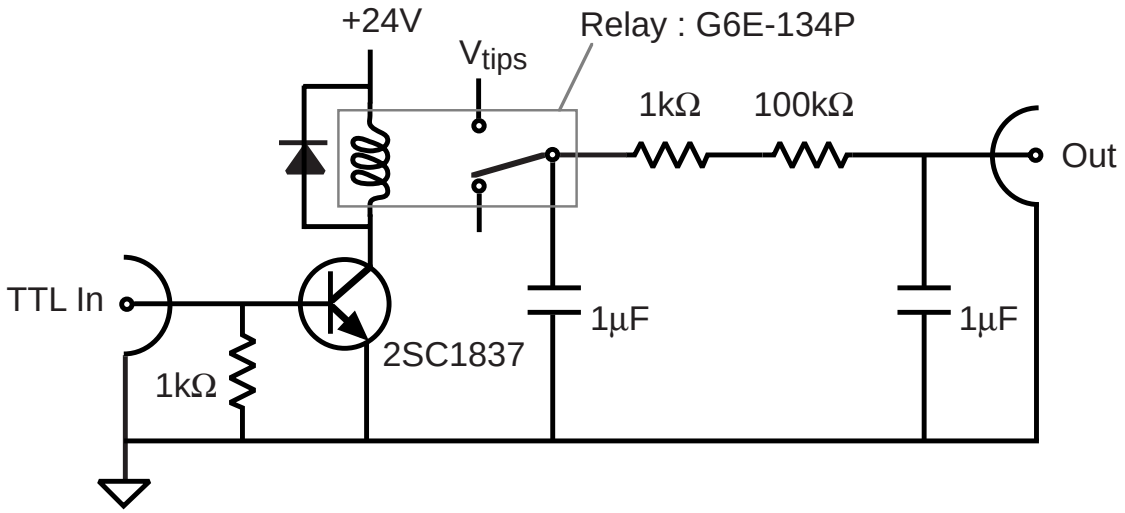

Figure 5.5: Bias supply circuit for the Spindt emitter. While the TTL in is on, V_{tips} is applied to the tips.

5.1.2 Duoplasmatron ion source

For the generation of protons and negative hydrogen ions, a Duoplasmatron ion source (HVEE Model358) was exploited. Fig.5.6 is a schematic drawing of the ion source. Since negative ions are known to be formed near the boundary of the first discharge region, we can extract them by changing the position of the intermediate electrode.

Below in Table 5.2, performance of this ion source is summarized. Current was measured with the Faraday cup shown in Fig.5.1. Experiments were performed with the same number of ions as the one expected for antiprotons. For the simulation of 50 keV-antiproton injection, at least DC current of 50 keV-proton beams should exceed 0.3 μA. This requirement was fulfilled without any difficulty. When the magnetic field of 1 T was applied, 60-70% of the incoming beam (1 keV H^- ions) was transmitted to the trapping region through the fringing magnetic field.

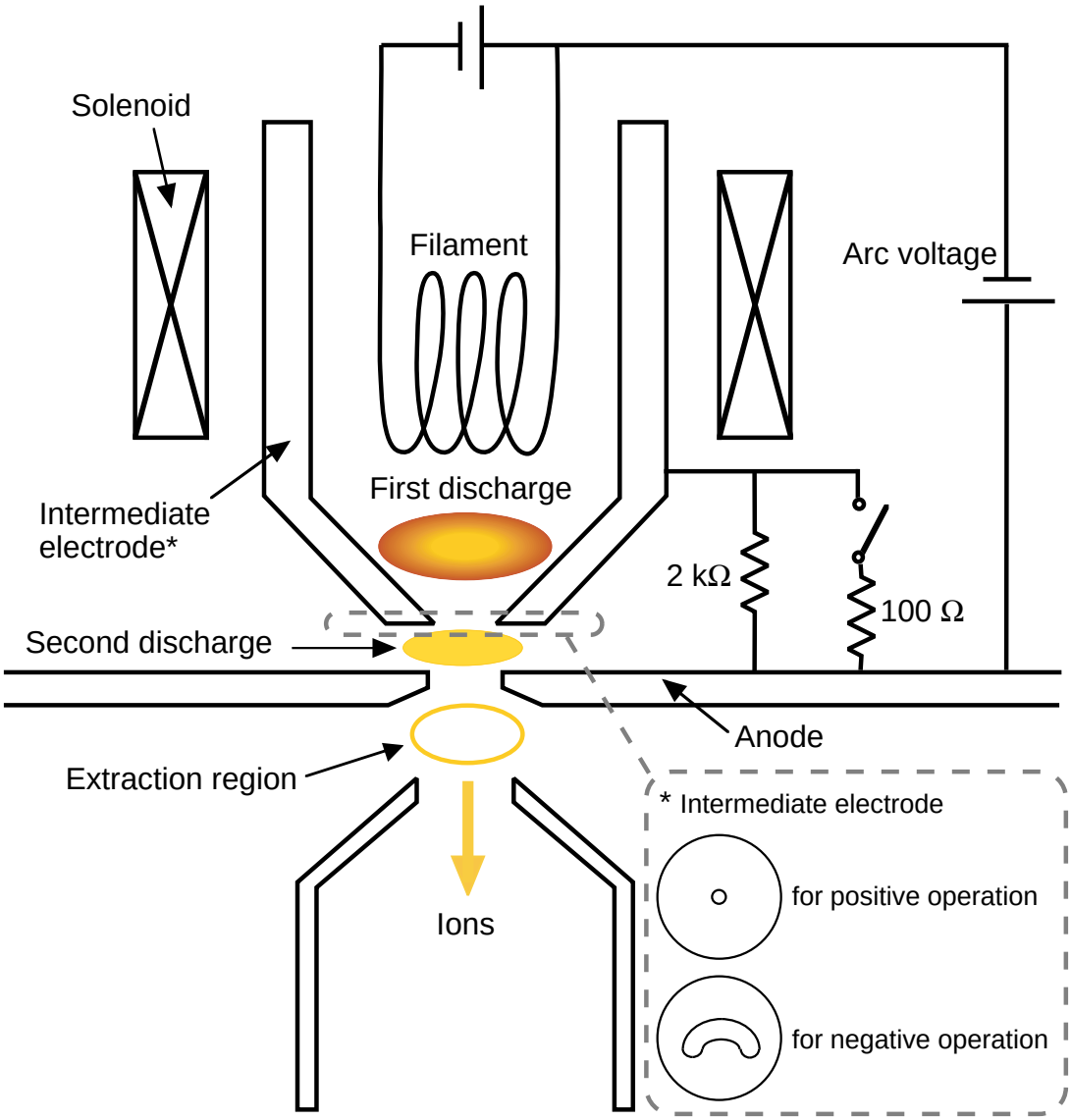

Figure 5.6: Cross section of Duoplasmatron ion source. Negative ions are known to be formed near the boundary of the plasma.

Extraction energy [keV]	Proton beam [μA]	H^- ion beam [μA]
1	-	0.4
25	31	-
53	37	-

Table 5.2: Performance of the ion source. DC current of proton beam or H^- ion was measured with the Faraday cup shown in Fig.5.1.

5.2 Confinement of electron plasmas

The Spindt emitter was located outside the magnetic field where the field strength is about 100 Gauss . Its radial position was adjustable within 0mm to 55mm and normally we injected electrons from an off axis point.

Trapping of electrons was done in the following manner. Consult with Fig.5.7.

1. Formation of a potential (on the axis) as the one shown on top.
2. Injection of electrons for about 2.5 sec from the emitter located 2 inch off axis from the center. Typical current was a few μA. The number of trapped electrons were controlled either by changing the emitter potential or by changing the duration of injection.
3. Extraction toward a Faraday cup (schematically shown in Fig.5.7) by changing the potential from upstream electrode to downstream.

Since there was no change in the potentials given to the electrodes during the injection, namely no active change was made in the entrance wall potential, electrons captured in the trap can be attributed to the ones that came from ionization of background gas or the ones that lost energy by collisions.

The number of electrons ejected after certain time was obtained by integrating a current flowing through a Faraday cup. The change in the number was measured by changing the trapping time and from the gradient of the least square fitted line, the life time was induced. Here, we define the lifetime as characteristic time such that the number of particles becomes $\frac{1}{e}$. Results of these lifetime measurements of electron plasmas are summarized in Fig.5.8. For both of the harmonic and cylindrical potential ($V_{trap} = 50$ V), two series of measurements was done by changing the initial number of electrons (marked

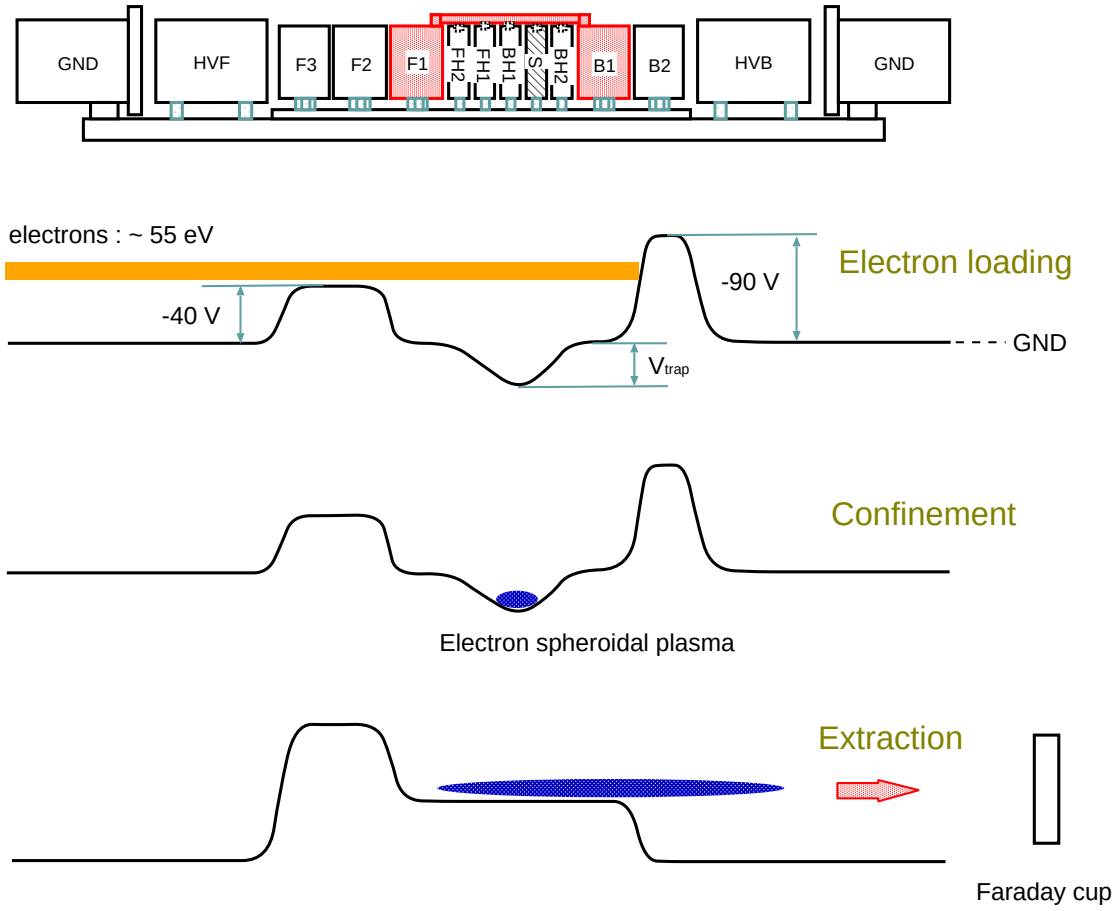

Figure 5.7: Formation-confinement-ejection of electron plasmas.

with the same name in the legend). In the case noted "high vacuum", the bore tube was cooled down to 10 K and the pressure monitored with a BA gauge was 5×10^{-10} Torr. For other measurements, pressure was about 1×10^{-9} Torr (bore tube temperature ~ 40 K). Since the gauge is located outside the cryogenic bore tube (in the room temperature position), the pressure in the trapping region is considered to be much better. The way to apply rotating field etc. will be explained in Sec.5.5.

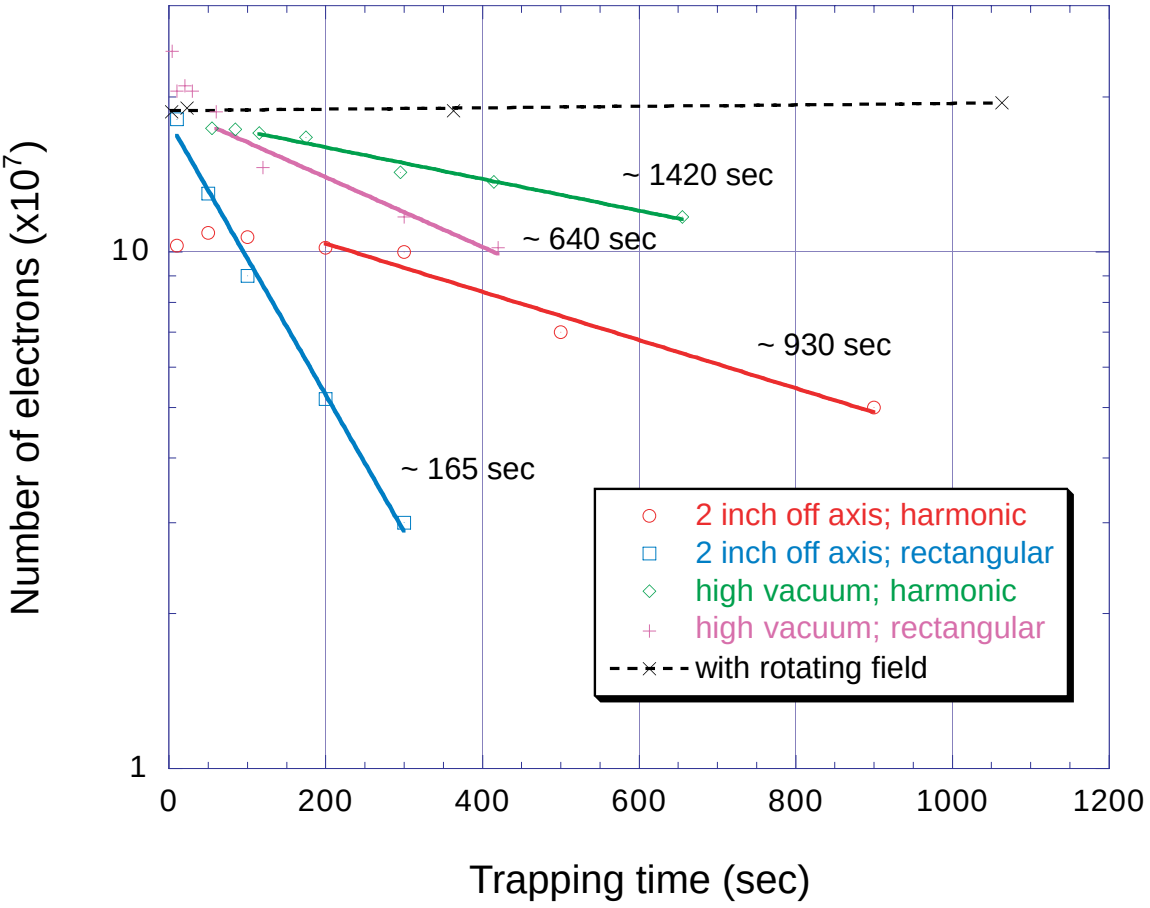

Figure 5.8: The number of electrons in plasmas vs. confinement time. $V_{trap} = 50$ V for both harmonic and rectangular potential. Two colors with the same description in the legend correspond to the difference in the initial number of electrons. Pressure monitored with a BA gauge was 1×10^{-9} Torr. In the case noted "high vacuum", the bore tube was cooled down to 10 K and the pressure was 5×10^{-10} Torr.

Containment property was also measured as a function of the magnetic field strength, which is shown in Fig.5.9.

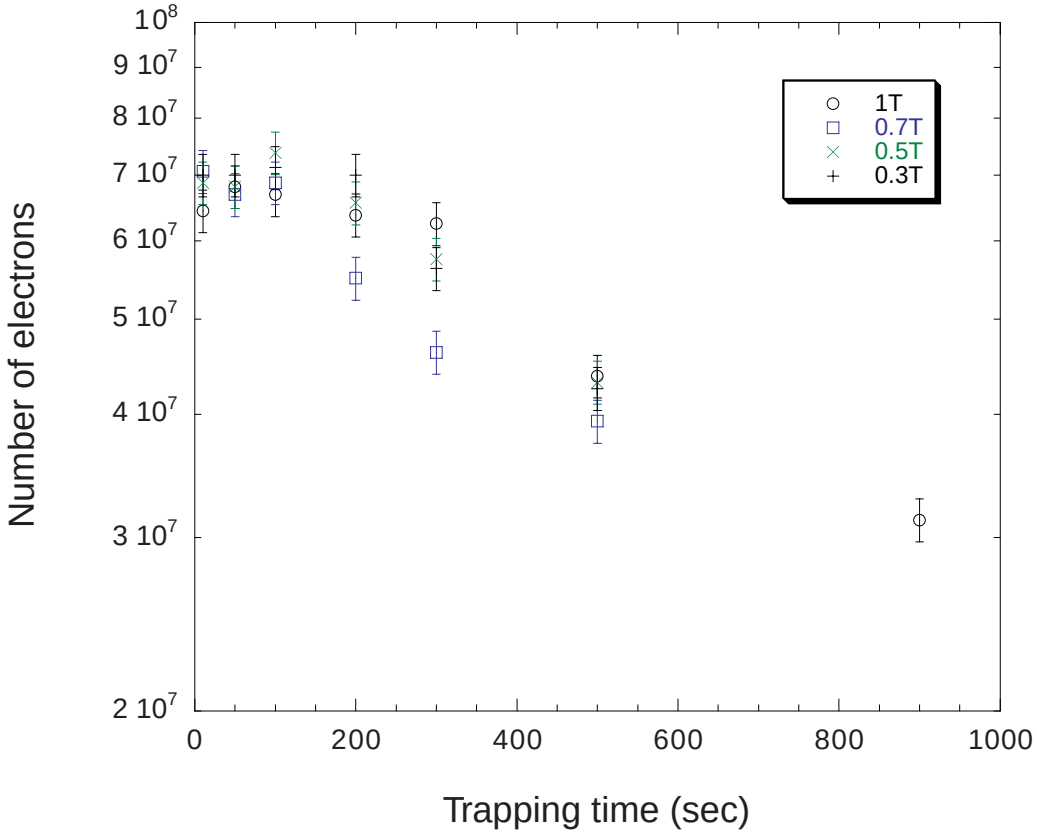

Figure 5.9: Decay of the number of electrons in plasmas with different B-fields.

We can see that the strength of the magnetic field had little influence on the lifetime, which is not easily explained[1]. It can be still governed by the field non-uniformity or the misalignment of trap electrodes to the magnetic field axis. We may note that there exist a report on the observation of B-independent transport[79] in the region where the ratio of the axial bounce frequency to the rotation frequency is larger $10 \sim 20$, which is our case.

5.2.1 Rectangular potential vs. harmonic potential I

It is remarkable that harmonic potential has a confinement ability superior to that of rectangular potential. This could be understood if we recall the fact that the confinement region in the case of rectangular potential becomes field free so that the plasma is fragile against any perturbations like field asymmetry etc.

[1] If plasmas diffuse classically, the lifetime scales as B^2.

5.3 Observation of plasma modes

Plasma modes described in Section 3.4.3 are useful tools to diagnose plasmas. Calculated mode frequencies are shown in Fig.5.10. Here, realistic parameters are assumed: $B = 1$ T, $N_e = 1 \times 10^8$, $b_0 = 6$ mm, and $T_e = 0.1$eV. In the abscissa, axial mode number (l) is given. Azimuthal node is zero.

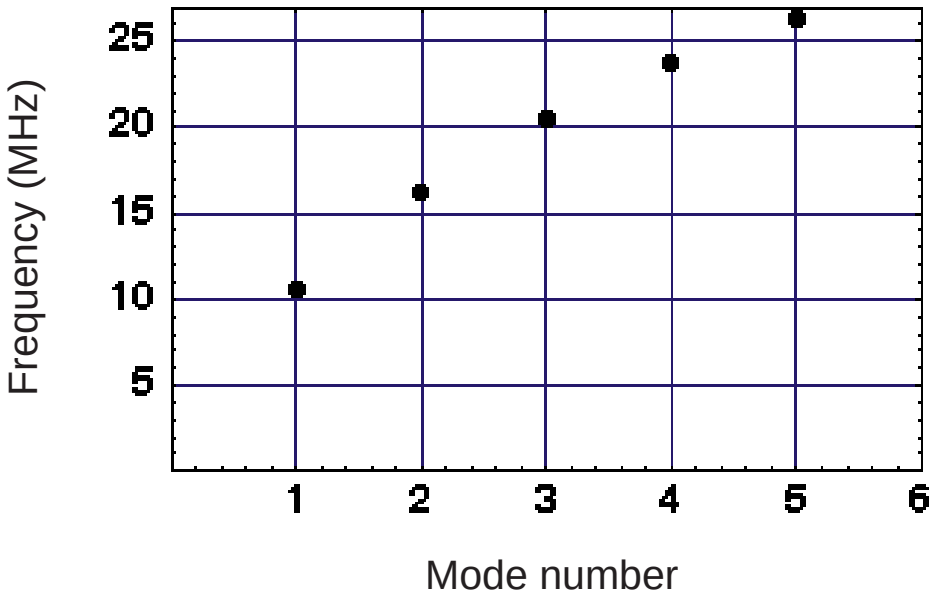

Figure 5.10: Calculated frequencies of plasma electrostatic modes. Assumed parameters : $B = 1$ T, $N_e = 1 \times 10^8$, $b_0 = 6$ mm, and $T_e = 0.1$eV.

Below, Fig.5.11 is a generic example of the axial modes observed with a spectrum analyzer. The signal picked up from the electrode "FH2" was amplified and analyzed with a FFT spectrum analyzer (SONY Tektronix 3056). Since "FH2" is a ring electrode, observable modes have axial symmetry. The top figure represents the Fourier transformed power vs. frequency and the other two figures are showing its temporal change. (1,0) mode and (2,0) mode are identified with the calculated values in Fig.5.10.

5.4 Plasma diagnostics with tank circuits

5.4.1 Basic concepts of tank circuits

Consider a parallel resonant circuit composed of an inductor, a capacitor and a resistor. Since both the capacitor and the inductor store energy, this kind of circuit is

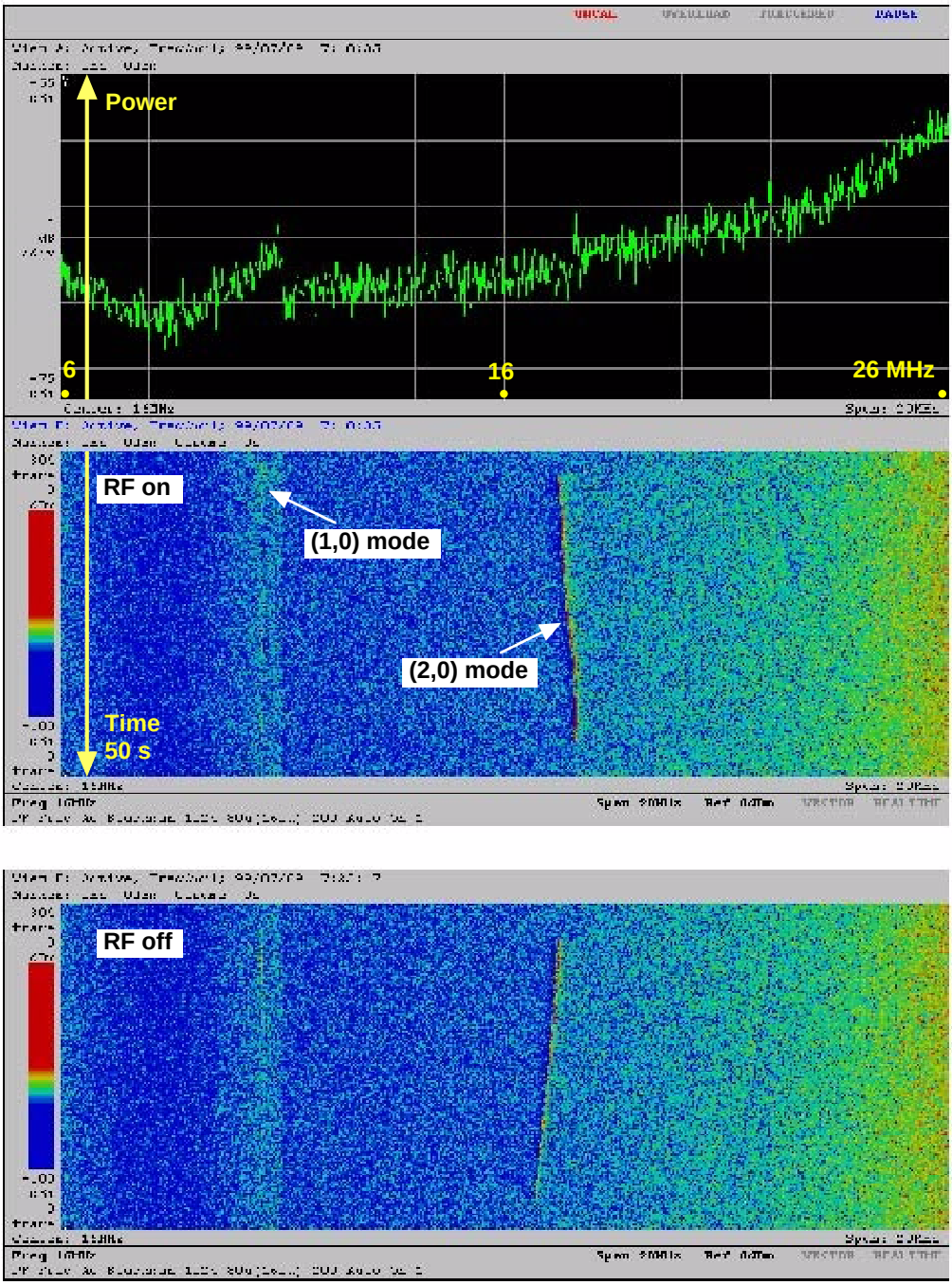

Figure 5.11: Observed plasma modes. (1,0) and (2,0) modes can be recognized. (3,0) mode is also visible.

referred to as a tank circuit. Since this circuit shows a bandpass response, it is also called a tuned circuit.

5.4.2 Monitoring of the number of stored particles with tuned circuits

This technique has been used to monitor the number of particles in a Penning trap[80, 81]. It is known that for n particles in a trap, an equivalent circuit can be considered, as is shown in Fig.5.12.

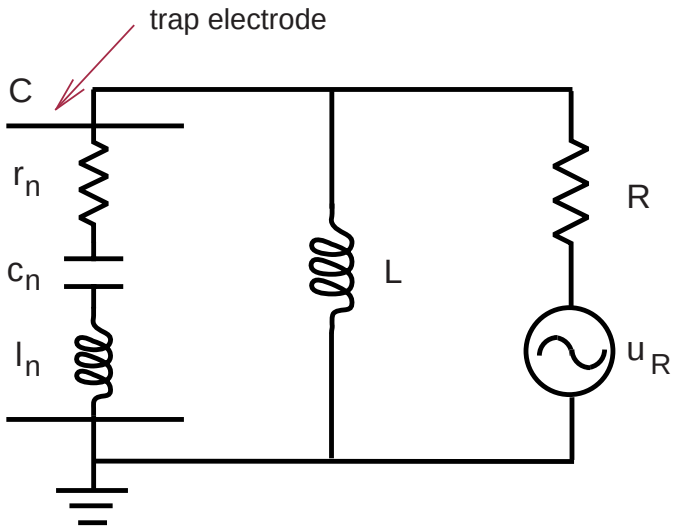

Figure 5.12: An equivalent circuit for charged particles oscillating in a parallel plate capacitor.

The impedance of the circuit is given by

$$Z = \frac{1}{\frac{1}{i\omega\ell_n + \frac{1}{i\omega c_n} + r_n} + i\omega C + \frac{1}{i\omega L} + \frac{1}{R}}. \tag{5.1}$$

When external L and C are resonated at ω_z, we can analyze that the impedance in Eq.(5.1) has one dip at $\omega = \omega_z$ and the width of the dip depends on the number of the particles. Thus, the number can be determined by measuring the width of the dip.

Fig.5.13 shows the setup for the determination of the electron number with a tank circuit tuned at the (1,0) frequency of electron plasmas.

Below, Fig.5.14 and Fig.5.15 are examples of measured resonance curve with a circuit tuned at the (1,0) frequency of electron plasmas. The spectrum in Fig.5.15 was obtained

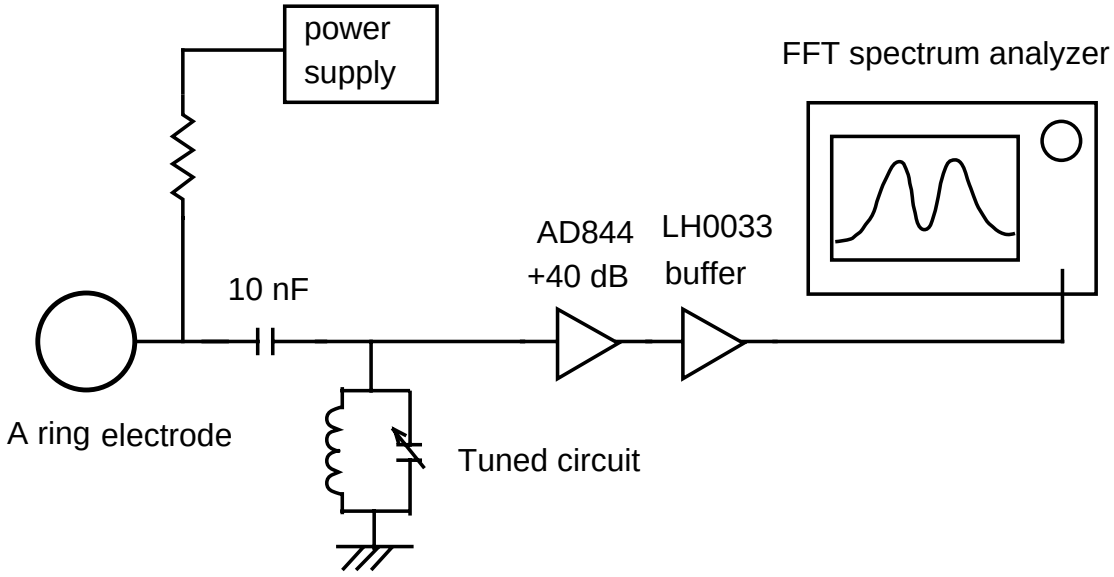

Figure 5.13: Electron number monitoring with a tuned circuit. The buffer(LH0033) was added for the protection of the spectrum analyzer. AD844 was for signal amplification.

for the electron number $N_e = 6 \times 10^7$ trapped in a potential of $V_{trap} = 50V$.

The calibration curve to determine the electron number from the measured peak splitting is shown in Fig.5.16. Δf is the separation of two peaks.

5.5 Radial compression of electron plasmas by an application of rotating electric fields

The fact has been established that the shape of a plasma can be controlled by applying a torque on it[64, 65, 82, 83]. In the case of nonneutral plasmas confined in rectangular potential, density changes due to coupling between rotating fields with normal modes are observed.

5.5.1 Circuit description

Azimuthal quadrupole field was generated at the segmented electrode with a circuit shown in Fig.5.17. Two inputs (phase = 0° and 90°) were prepared by an function generator (NF1946). Using ferrite cores each input was split into two so that the one

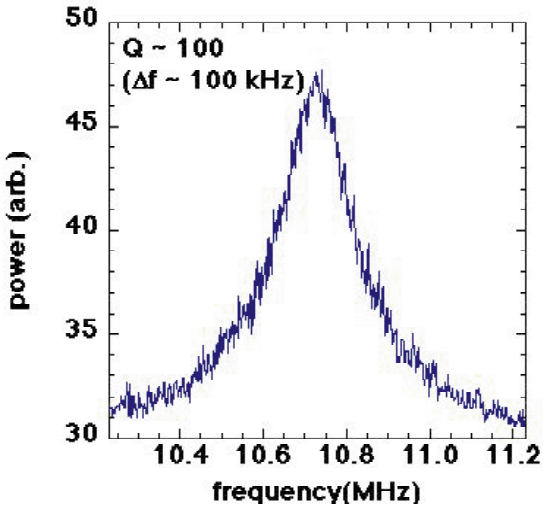

Figure 5.14: Resonance curve without electrons.

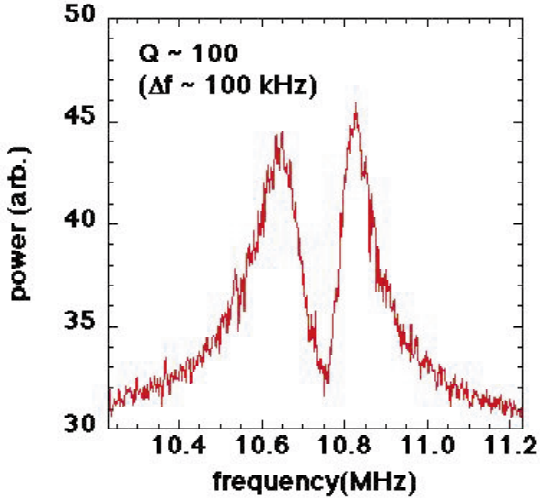

Figure 5.15: Resonance curve with electrons ($\sim 6 \times 10^7$).

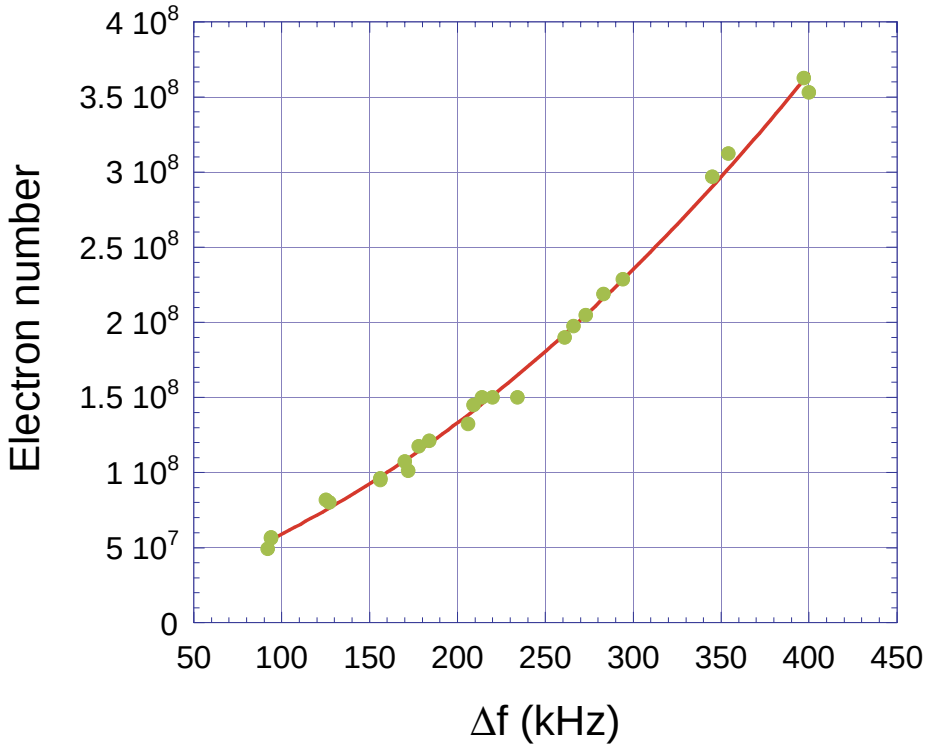

Figure 5.16: Electron number monitored with a tuned circuit. The solid line represents the least square fit to a quadratic function. Δf is the peak-to-peak separation.

keeps the original phase and the other has 180° retarded one. Outputs are amplified by operational amplifiers (OPA658) and applied to the segmented electrode.

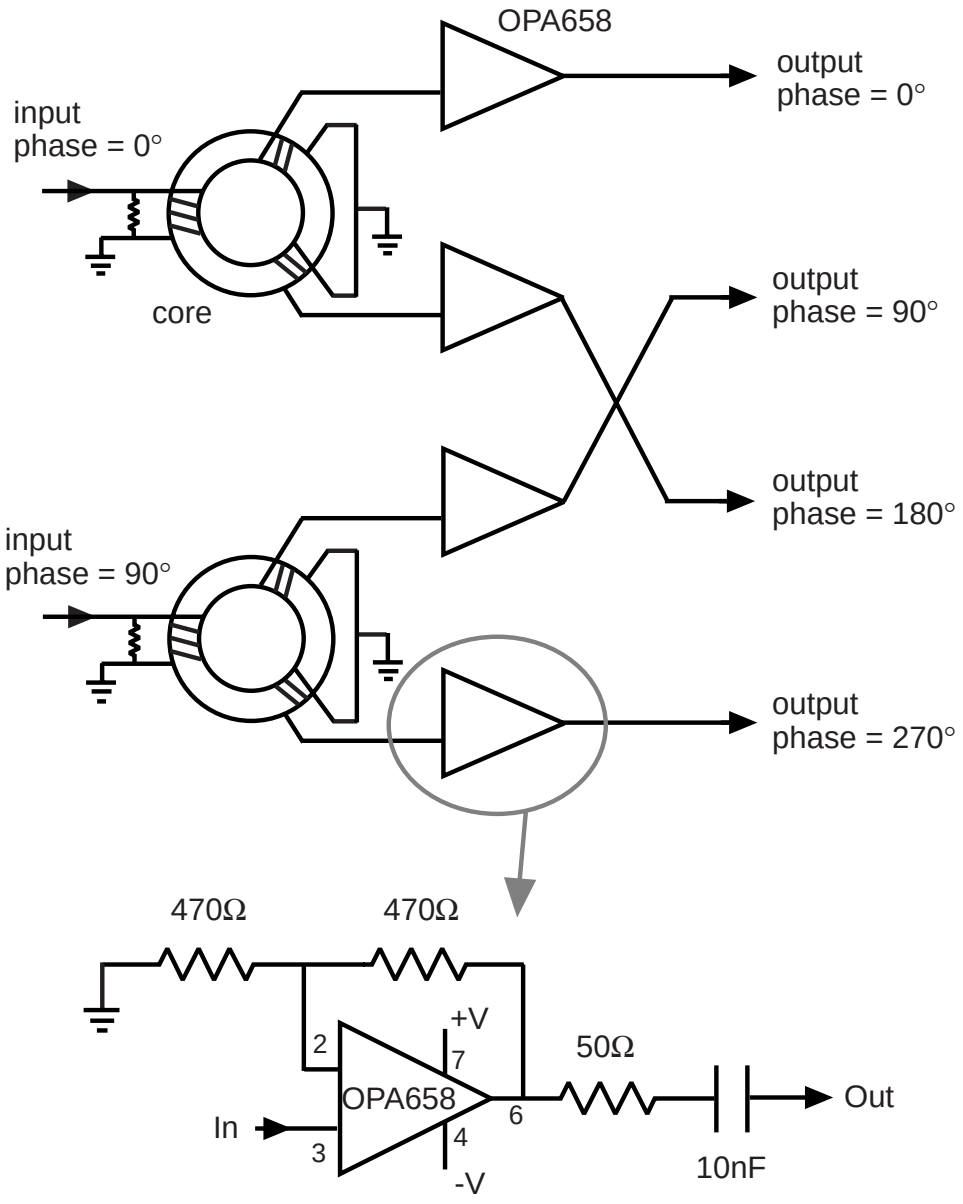

Figure 5.17: The circuit for rotating electric field generation. Total amplification is 2.

5.5.2 Measurement of a compression ratio with a segmented Faraday cup

At first, we searched parameters by measuring the charge with a radially segmented Faraday cup[84]. The inner diameter was 2 mm and the outer diameter was 38 mm. It was located next to the HV electrode, where the magnetic field is still uniform. In Fig.5.18, shown are electrode configuration and schematic trap-cool-dump procedure.

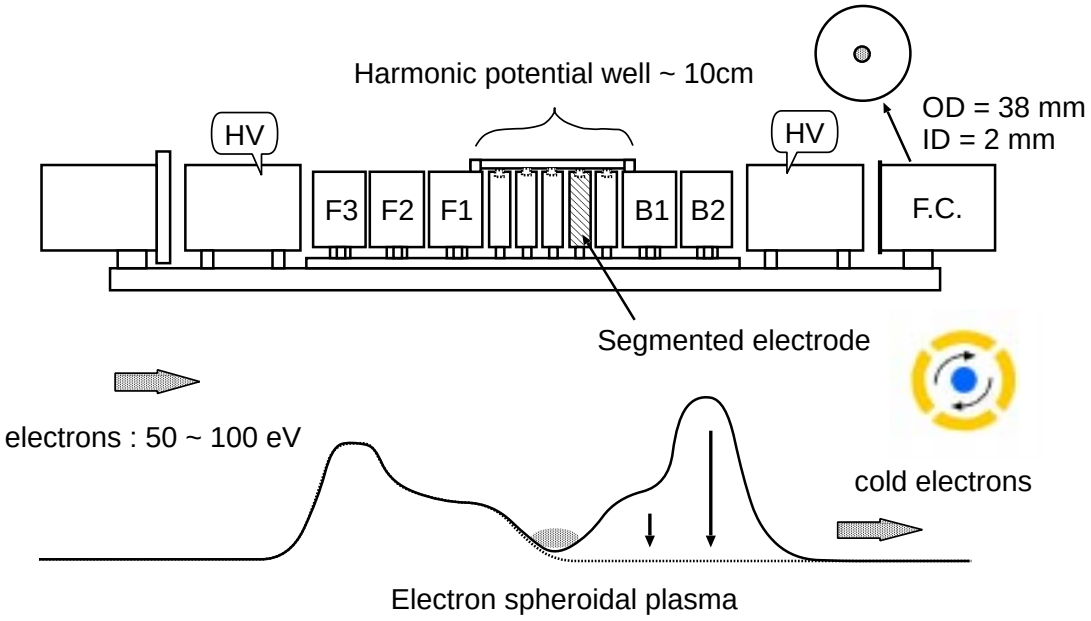

Figure 5.18: Configuration of electrodes with a segmented Faraday cup. There was no change in the potential during the injection of electrons. At the ejection, potential on each electrode was changed one by one from the upstream electrode to lower the potential on BH1-B2.

The rotating field was applied keeping the sweep rate constant(2 MHz/min). (In our case, all through the experiments with electrons, only quadrupole field has been applied.) The results are summarized in Fig.5.19. Amplitude was 1.0 V $(\frac{1}{2}V_{pp})$[2]. It was shown that the rotating electric field can compress the electron plasma and up to 60% of the constituent particles was confined within a region of 2 mm in diameter. In addition, the lifetime of the plasma became longer (See Fig.5.8). It can also be seen that the application of too high frequency reduces the fraction of electrons compressed radially. From the fact

[2]Though what counts is not the voltage but the strength of the electric field, let us use the amplitude of the applied voltage on segmented electrodes as an index. Since the radius of curvature of each segment is 2 cm, it can be read as 1 V/2 cm.

that there was no significant change in the compression ratio when we change the sweep rate to twice as long, destination frequency of around 2.5 MHz seems to be the most effective. Since the effectiveness also depends on the sweep rate, optimization is still necessary. Generation of electrons by ionizing the residual gas was observed when the amplitude was too high.

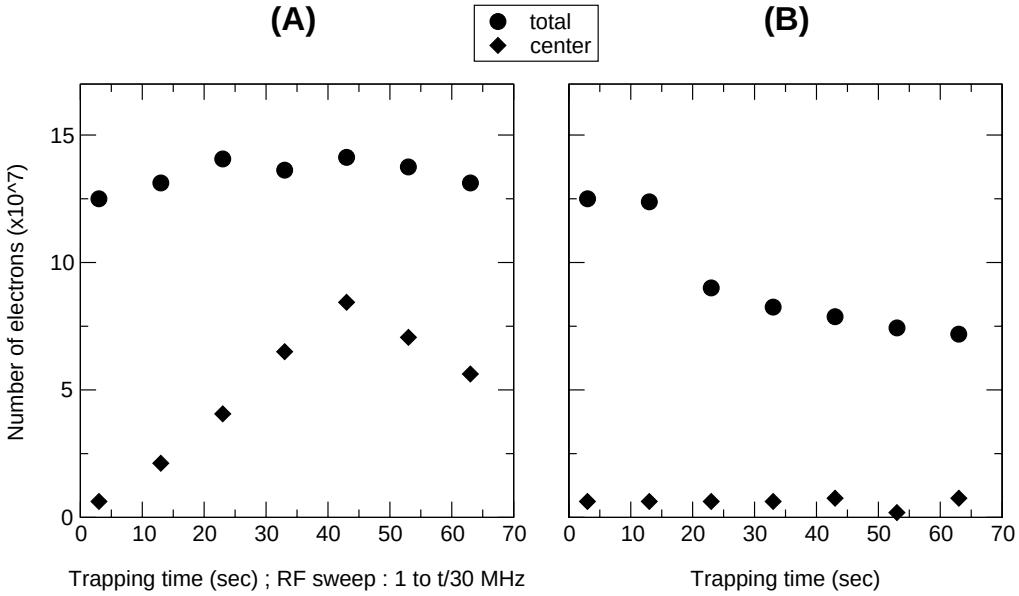

Figure 5.19: Effect of rotating electric fields. (A) : with rotating field, (B) : without rotating field. Amplitude was 1.0 V.

5.5.3 Observation of radial profiles

In the next step, the effect of rotating electric field to the plasmas was directly observed by a combination of a zinc oxide (ZnO) screen formed on thin layer of Indium-Tin-Oxide (ITO) and a CCD camera. ZnO(P-15) emits green light (peak at 505 nm) and is normally used in low energy applications. We selected it since it has the highest light emissivity at least in the electron energy range 1 eV - 100 eV. ZnO screen was prepared on a glass plate coated with thin layer of ITO. It is a kind of ceramic and is known to be transparent as well as electrically conductive[3]. Transmissivity of ITO is shown in Fig.5.20. The advantage is that we can observe the profile and can measure the charge at the same time. The size of the ZnO screen was 40 mm $\times$ 40 mm and as a Faraday cup, it covers 50 mm $\times$ 50 mm. At the position of the screen, the strength of the magnetic field was 0.9 T while we have 1.0 T at the center of the bore tube. The screen can be electrically floated for the acceleration of electrons that impinge on it. We note this voltage as V_{acc}.

[3]We can note that ZnO itself, when it is in the form of crystal, is a material of the same kind.

The CCD used in the experiment (ROX-40) was selected because of its high sensitivity (0.0005 lx), peaks around 500 nm as shown in Fig.5.21 which is also convenient for the detection of lights from the ZnO. The NTSC (National Television Standards Committee) output was connected to the input of the digital camera recorder.

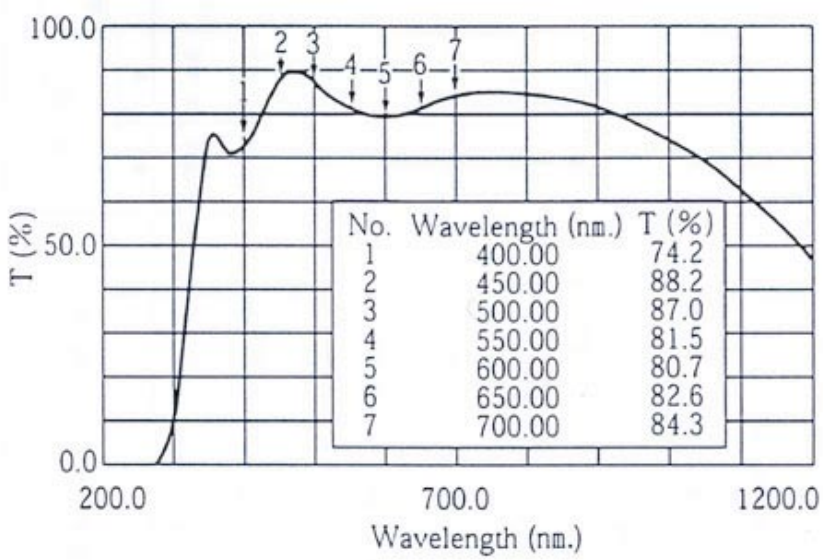

Figure 5.20: Transmissivity of ITO screen.

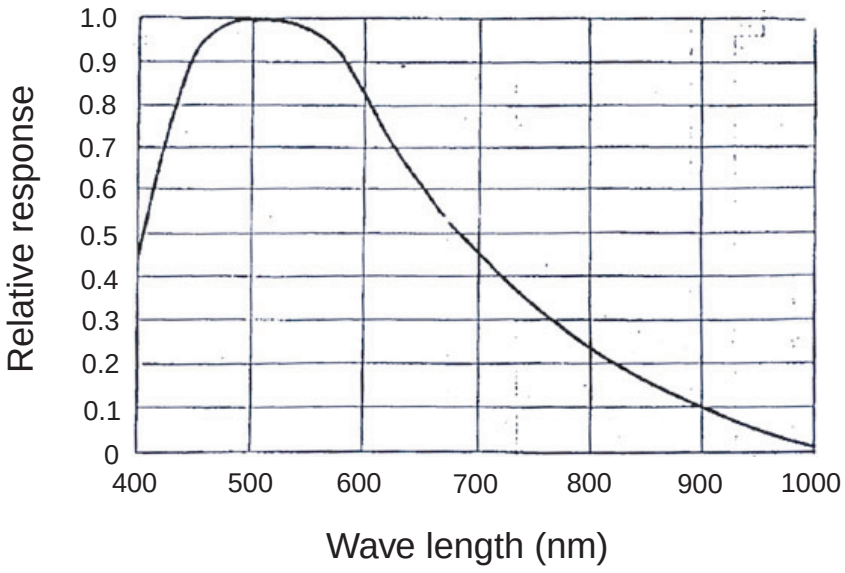

Figure 5.21: Sensitivity of the CCD (ROX-40).

Setup is shown in Fig.5.22.

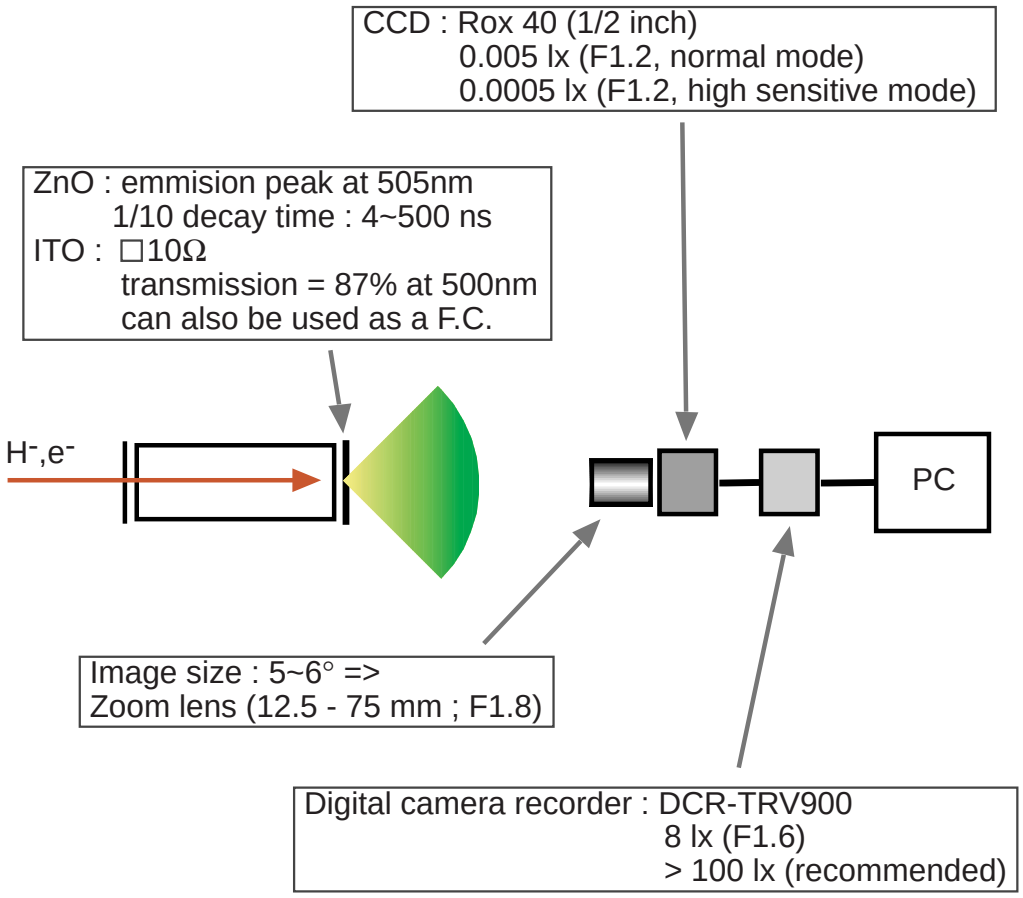

Figure 5.22: Configuration of ZnO screen and CCD camera for the observation of radial profiles of plasmas

Fig.5.23 shows the image taken with the CCD camera. Electron emitter was at the position about 2.5 cm off-axis. The upper-left figure shows the profile without the rotating field, and lower-left, with the rotating field. Note that the profile is line-integrated along the magnetic field axis. In the case without rotating field, a fit to an elliptical function is also shown. If the plasma is spheroidal and has a uniform density, line-integrated profile becomes elliptical. The fitting is well within a fluctuation of the data and we may consider that the plasma is spheroidal. Total number of electrons was $N_e = 1.1 \times 10^8$ and the frequency of rotating field was swept from 500 kHz to 3 MHz within 15 sec (Note that the condition was not identical to the one shown in Fig.5.19). The amplitude of the rotating field was 1 V. The acceleration voltage (V_{acc}) of 2.5 kV was applied to the surface of the ZnO screen. Electrons were preloaded in the trap 60 sec before the application of rotating field and ejected while rotating field on, at the frequency around 2.7 MHz. By

comparing the profile with and without rotating field, we can observe that rotating fields deform the plasma so that its radial profile differs from the one for spheroidal plasmas.

To avoid a spatial conflict between the emitter and the ion beam injected from the ion source, it was necessary to further change the electron gun position to about 5 cm off-axis. Profiles with no azimuthal field applied are shown in Fig.5.24 for 2.5 cm off-axis injection, and in Fig.5.25 for 5 cm off-axis injection. Below, superposition of ellipses on the radial profile guides the eye to check whether the plasma was really spheroidal or not. The fact that the right shoulder is systematically lower than the left seems to be because of the non-uniform ZnO screen. Except the images shown in Fig.5.23, all the profiles were observed with the same ZnO screen.

After making sure that the plasma shape can be controlled by sweeping the frequency as was done in Section 5.5.2, we tried to apply a field with a constant frequency and found that it is also possible to compress the plasma under certain conditions. Fig.5.26 shows the temporal evolution of profiles. The number of electrons was $N_e = 1.3 \times 10^8$. Rotating field was applied for 120 sec, from 60 sec after the injection of electrons. The frequency was 2 MHz, and the amplitude was 0.5 V. By roughly estimating the number of particles at each radial position, it can be seen that about a half of the trapped electrons were gathered within the radius of 1 mm, which is in congruity with the measurement with a segmented Faraday cup (*cf.* previous section). After the application of rotating field for 120 sec, it was also observed that the plasma keeps the compressed shape at least for 30 sec.

Now it is possible to enumerate factors that affects the profile: (1) the frequency of rotating field, (2) its amplitude and duration, (3) the number of particles, and (4) the trap depth. Let us examine how the radial profile changes as these parameters. Firstly in Fig.5.28, frequency dependence is shown. Electrons were loaded 60 sec before the application of rotating field, which lasted 60 sec at each frequency.

Three facts can be immediately seen.

1. In our case, any fields rotating at a proper constant frequency (1.5 MHz $< f \leq$ 2.5 MHz) rotating in the same direction as plasmas were found to be effective.
2. Except for 3.0 MHz, the higher the frequency is, the sharper the central part becomes. The minimum diameter was about 1.5 mm.

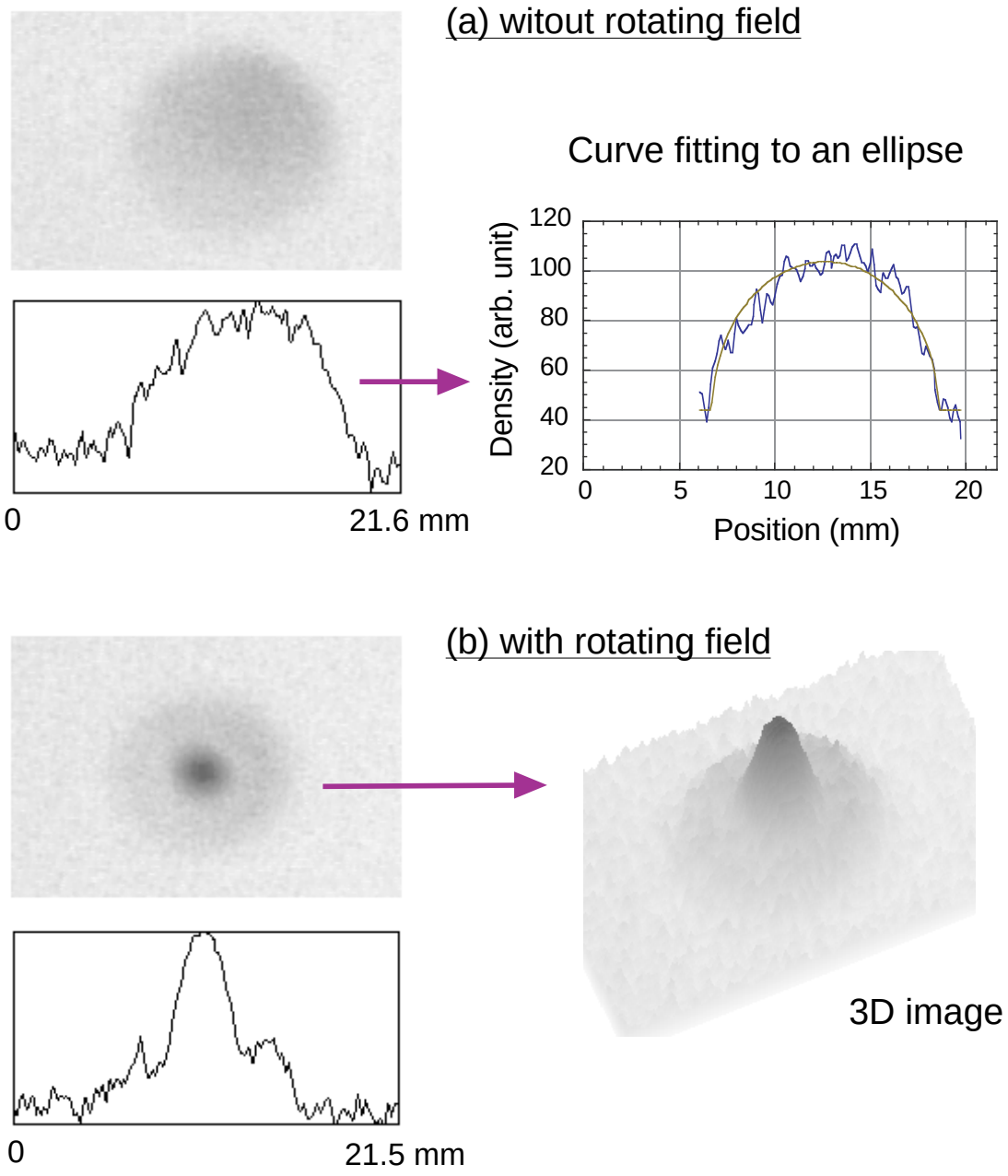

Figure 5.23: Compression of electron plasmas. Two cases are shown: (a) without and (b) with rotating field. Total number of electrons : $N_e = 1.1 \times 10^8$, frequency of rotating electric field was swept from 500 kHz to 3 MHz within 15 sec and electrons were ejected while rotating field was on (at around 2.7 MHz). $V_{acc} = 2.5$ kV.

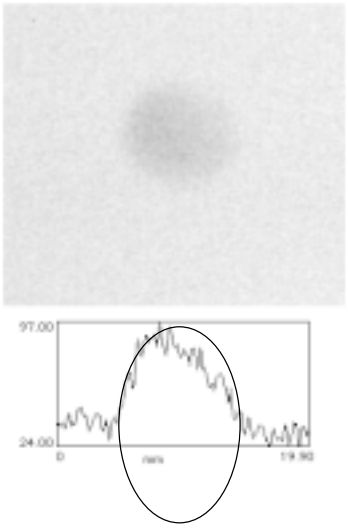

Figure 5.24: No rotating field ; 1 inch injection

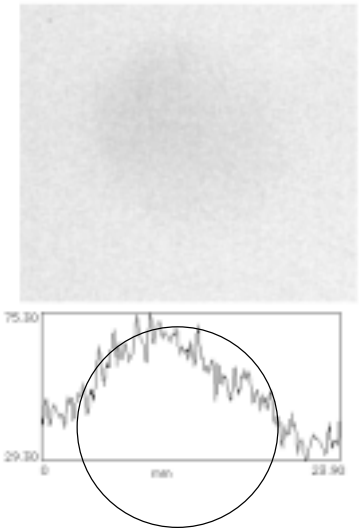

Figure 5.25: No rotating field ; 2 inch injection

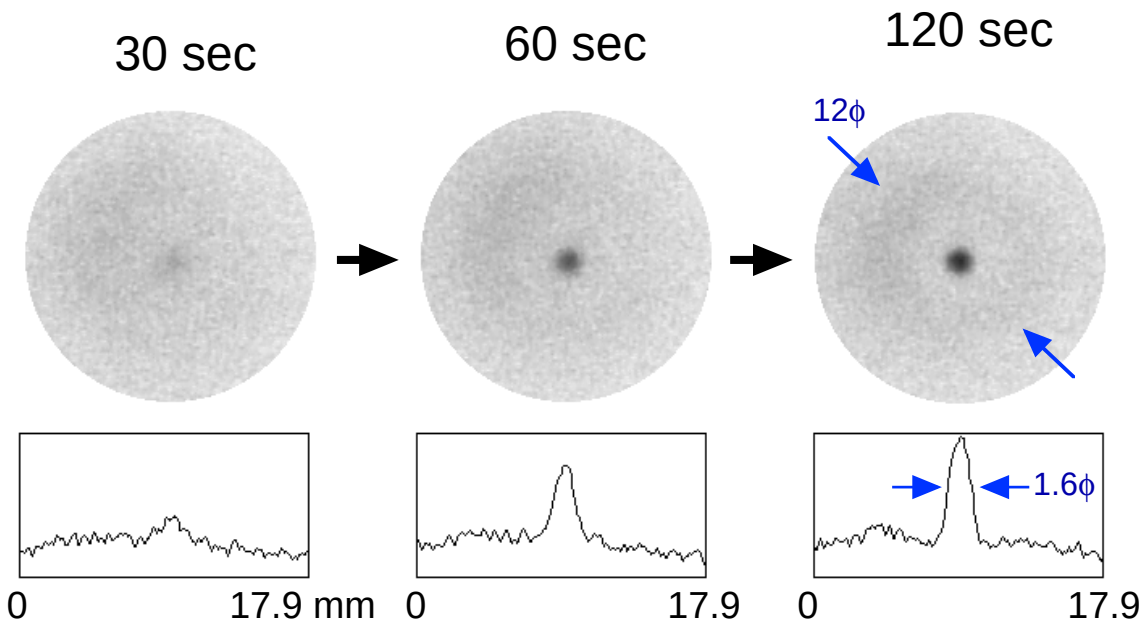

Figure 5.26: Temporal change of the profiles of electron plasmas. $V_{trap} = 50$V and $N_e = 1.3 \times 10^8$. 60 sec waiting + 120 sec rotating field at 2 MHz, 0.5 V.

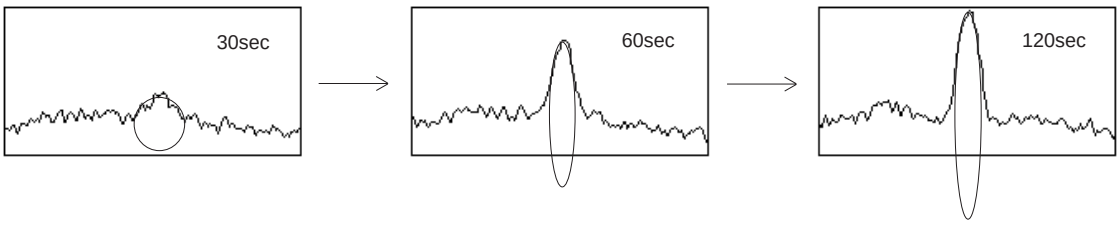

Figure 5.27: Profile change with ellipses to guide the eye.

3. Between 2.5 MHz and 3.0 MHz, there seems to exist a threshold such that the ionization of background gas starts to be significant. This fact can possibly be applied for pressure gauges in ultra-high vacuum region. It may also be noted that the ionization of background gas by RF fields can be used to maintain the number of electrons[85].

About the second parameters, amplitude and duration of rotating fields, they were optimized together with the frequency. The dependence of the diameter on the field amplitude is shown in Fig.5.29. The frequency of the rotating field was 2 MHz.

Secondly, dependence on the total charge (N_e) was observed (Fig.5.30-5.32. Numbers under each figure represent the total number of electrons trapped.). As in the case for frequency dependence measurements, electrons were loaded 60 sec before the application of rotating field, which lasted 60 sec at each frequency. V_{acc} was 6.0 kV. Since the trap depth was kept constant (V_{trap} = 50 V) in these observations, to have more particles directly leads the radial expansion of the plasma. These figures qualitatively show that tendency.

Third parameter is the trap depth. Fig.5.33 shows how profiles changed according to it. Rotating field (2 MHz) was applied for 60 sec, starting from 60 sec after the confinement. The number of electrons (N_e) was 1.0×10^8, and the acceleration voltage (V_{acc}) was 4.0 kV.

Shallower potential will make the plasma extend axially so that the aspect ratio will be large. As was expected, in V_{trap} = 20 V case, the radius of central part became smaller than in the case of V_{trap} = 50 V. It was also observed that the time width of extracted electrons became longer, which is consistent with axially elongated shape.

When a plasma in a harmonic well is in equilibrium, constituent particles distribute

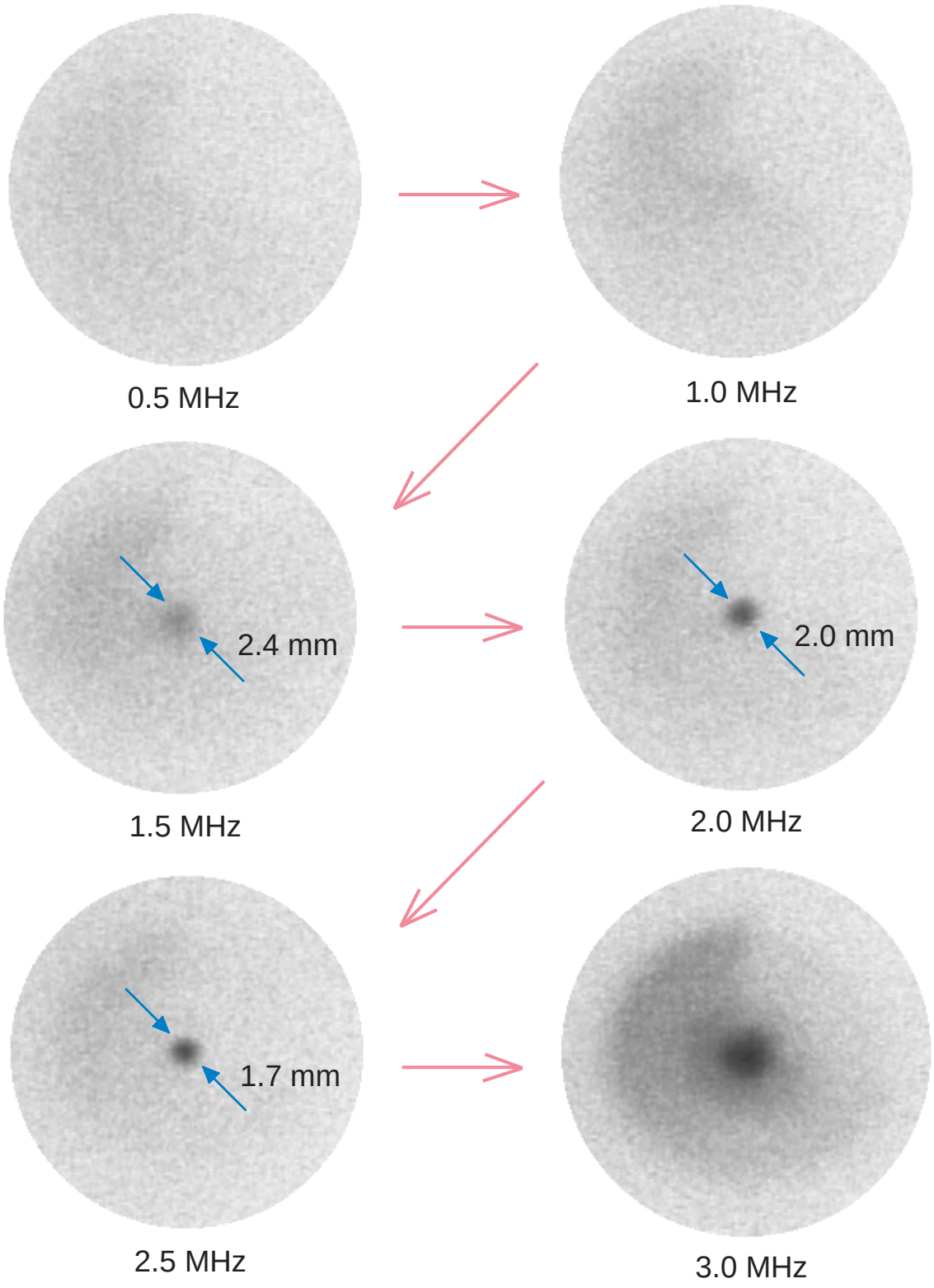

Figure 5.28: Effect of the frequency of rotating electric fields on the profile of electron plasmas. Trapping time was 60 sec (waiting) + 60 sec (with rotating field, 0.5 V). V_{acc} = 4.0 kV.

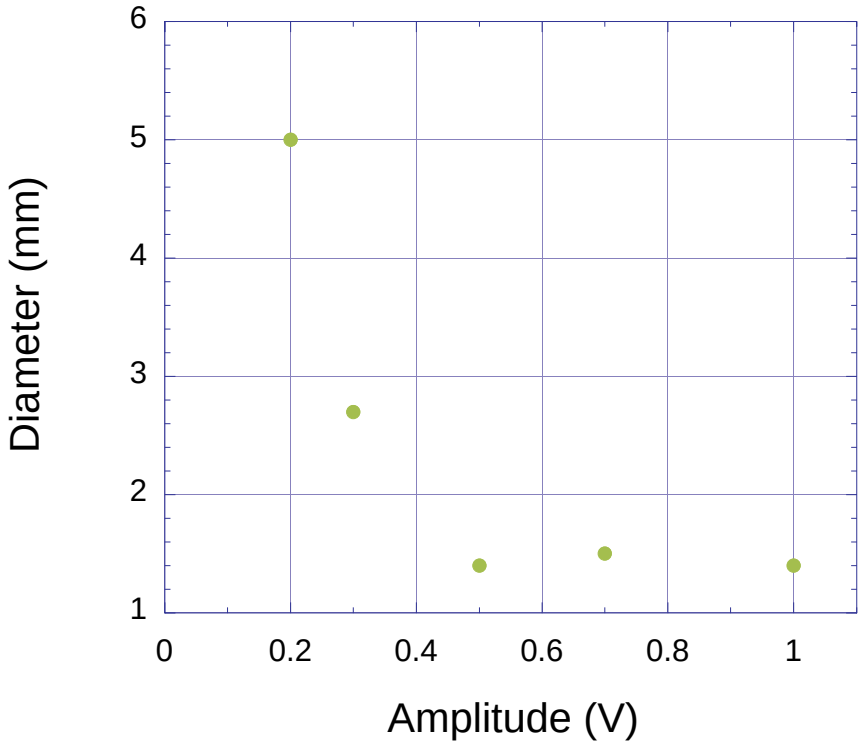

Figure 5.29: Amplitude dependence of the compressed diameter, measured for the constant rotation frequency of 2 MHz. Trapping time was 60 sec (waiting) + 60 sec (with rotating field). $V_{acc} = 4.0$ kV.

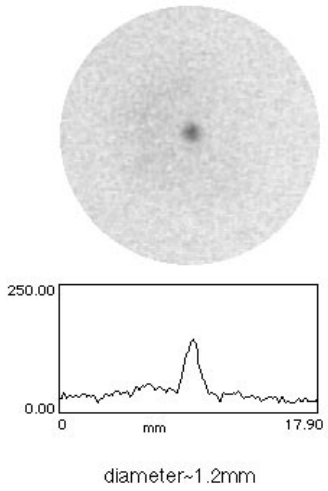

Figure 5.30: $N_e = 1.3 \times 10^7$

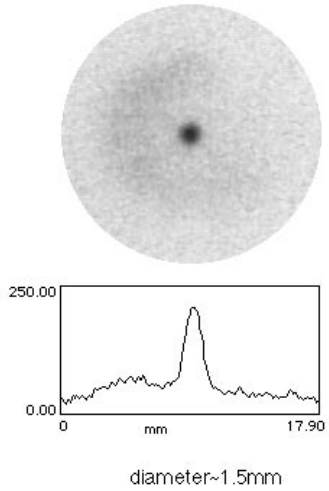

Figure 5.31: $N_e = 3.6 \times 10^7$

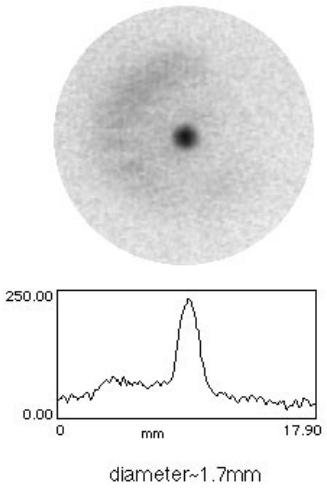

Figure 5.32: $N_e = 5.4 \times 10^7$

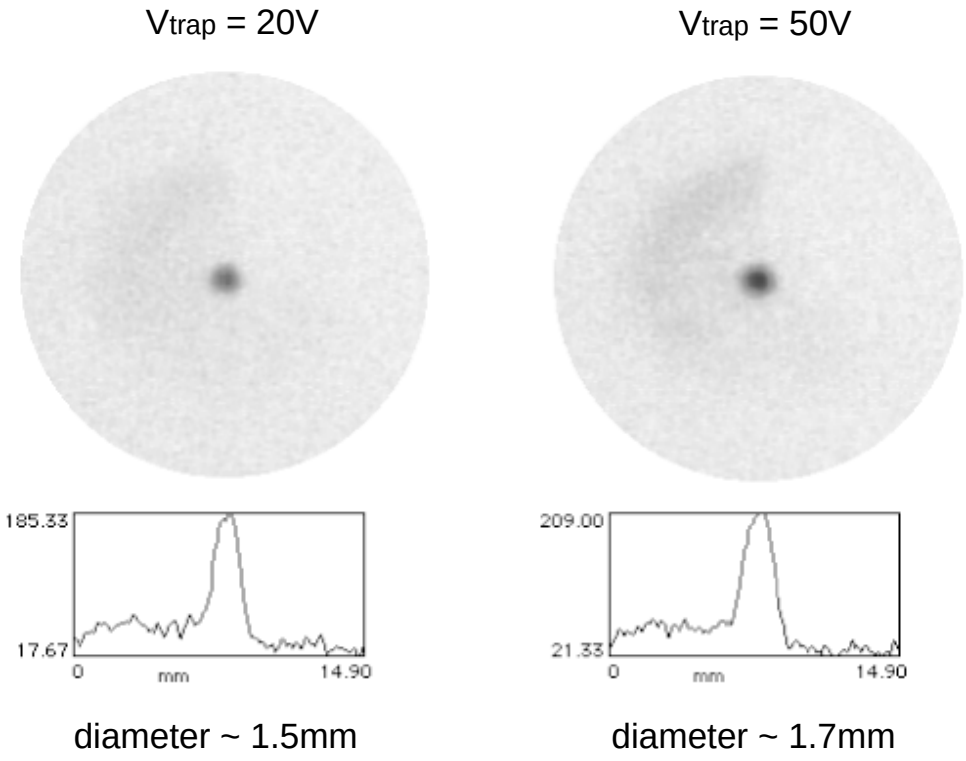

Figure 5.33: Radial compression of electron plasmas with different trap depth with 2 MHz rotating field. $N_e = 1.0 \times 10^8$, $V_{acc} = 4.0$ kV

themselves so that the applied trap potential is canceled. When we compress the plasma with a rotating field, because of the space potential, its axial length will be longer. This means, around the center, restoring force by the trap potential exist. It seems to be decisive to the minimum possible radii of the compressed plasma.

5.5.4 Rectangular potential vs. harmonic potential II

The effect of rotating electric fields on electron plasmas in rectangular potentials is shown in Fig.5.34 for the potential depth = 25 V and in Fig.5.35 for the potential depth = 50 V. V_{acc} was 4.0 kV for both observations. The application of rotating field started 60 sec after the injection of electrons. The duration was 120 sec at 2 MHz. As compared with the radius for harmonic potential (Fig.5.33), diameter of central dense region became larger by approximately 50%. However, it is interesting to see that there is little halo around the central peak.

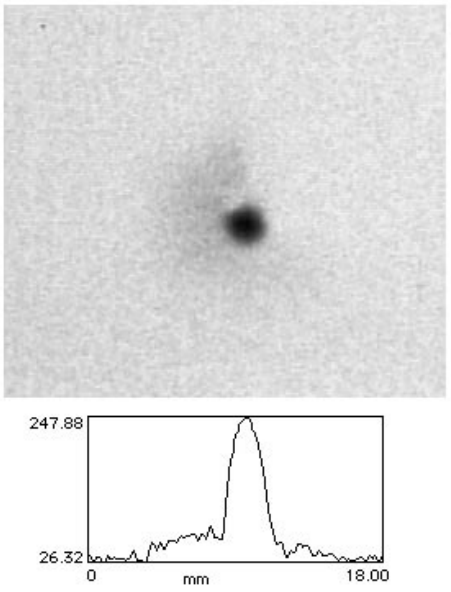

Figure 5.34: Rectangular potential ; V_{trap} = 25 V. $N_e = 1.3 \times 10^8$. V_{acc} = 4.0 kV. Diameter is about 2.4 mm.

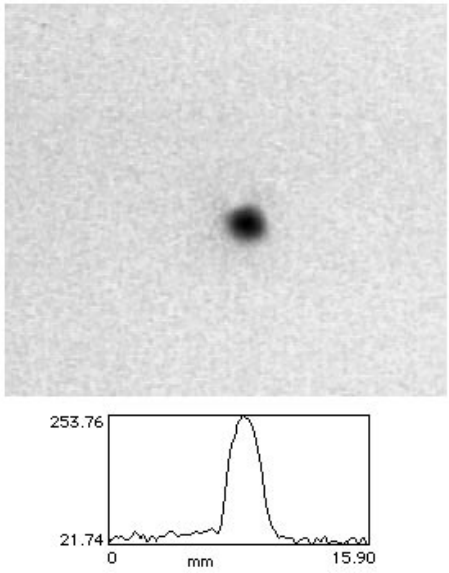

Figure 5.35: Rectangular potential ; V_{trap} = 50 V. $N_e = 9.6 \times 10^7$. V_{acc} = 4.0 kV. Diameter is about 2.3 mm.

5.6 Confinement of negative hydrogen ions

A negative hydrogen ion has the same charge and almost the same mass as those of an antiproton and it is the best candidate for the simulation experiment of antiprotons.

However, there is one thing which is definitely different between H^- ions and antiprotons: A negative hydrogen ion is a composite particle whose binding energy is 0.75 eV. This means that we should be careful so as not to destroy it for the experiments to be successful. This leads to these two cautions.

1. The injection energy should be lower than 1.4 keV, which corresponds to 0.75 eV for the electron bound to the H^- ion. Otherwise, detachment process by the collisions with electrons in the trap will be preponderate.

2. Collisions with neutral residual gas should be taken into account. Above a few eV in CM energy, the detachment by collisions with them will be of significance.

In Fig.5.36, cross section for the reaction $H^- + H_2 \rightarrow H + e^- + H_2$ is shown[86]. (Note that in our cryogenic environment, the main component of the residual gas was molecular hydrogen. See Fig.4.15.) Detachment cross sections on various gases are summarized in the reference [87]. One of the experimental data for the detachment on hydrogen molecule can be found in the reference by Risley *et. al.*[88].

Using a detachment cross section $\sigma \sim 10^{-15}$ cm^2, density of residual hydrogen $n \sim 10^6$ cm^{-3} (at 10 K ; 10^{-12} Torr), velocity of 100 eV-H^- ions $v \sim 2 \times 10^7$ cm s^{-1}, we can estimate that the lifetime of H^- ions is about 50 sec. To maximize the lifetime, we tried by lowering the bore tube temperature to keep the pressure as low as possible so that the number of the residual gas decreases. So far, lowest temperature of 5.7 K has been observed. At the same time, the trap was floated to a certain potential so that the kinetic energy of H^- ions inside the trap would be smaller(See the following sections).

5.6.1 Energy distribution

Ideally, if monoenergetic H^- ions can be introduced in the trap, we can define the initial kinetic energy of ions inside the plasma and we can easily set the floating potential. On the other hand, when the direction of injection is not parallel in that case, perpendicular energy component ($E_\perp$) will change. If we consider the conservation of magnetic moment, we can estimate it. Supposing that H^- ions with $E_\perp = E_{\perp out}$ are injected from the point where $B = B_{out}$ and enters into a magnetic field of B_{in},

$$\mu = \frac{E_{\perp out}}{B_{out}} = \frac{E_{\perp in}}{B_{in}}, \tag{5.2}$$

that means

$$\frac{E_{\perp in}}{E_{\perp out}} = \frac{B_{in}}{B_{out}}. \tag{5.3}$$

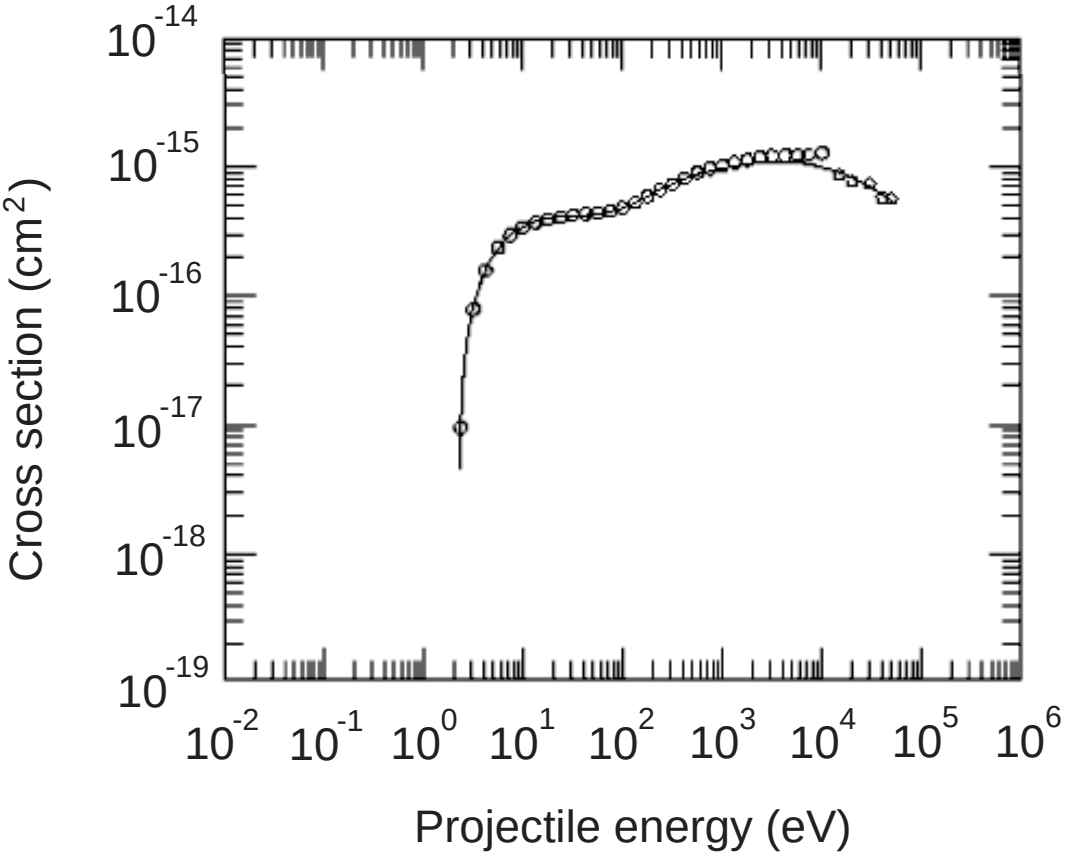

Figure 5.36: Detachment cross section of H^- ions ($H^- + H_2 \rightarrow$ fast $H + e^- + H_2$)[86].

In practice, $\frac{B_{in}}{B_{out}} \sim 1000$.

By monitoring the current transmitted through the trap, energy distribution parallel to the magnetic field axis was measured to be as broad as 900-1000 eV for 1000 eV injection. The trap floating potential was set close to -900 V so that the trapping efficiency becomes maximum.

5.6.2 Lifetime of H^- ions

To find the optimum condition for effective electron cooling of H^- ions, ions should be trapped for sufficiently long period in the trap. At first, we measured the lifetime of H^- ions in the trap. Fig.5.37 shows the procedure (electrons were not introduced in this case). While H^- ions are being injected into the trap (floated to -890 V) the potential on the HVF electrode is ramped up. Next, the potential on HVB is lowered. Then, by reducing the potential on B2, ions are extracted toward the Faraday cup, namely, the ITO screen described in Sec.5.5.3. Its effective area measured 50 mm $\times$ 50 mm. At the position of the Faraday cup, the strength of the magnetic field was about 0.9 T when we had 1.0 T at the center. To get the particle number, signal from the Faraday cup was connected to a charge amplifier (ORTEC;142AH) and the voltage output was converted to a number with a conversion factor of 162 mV for 10^6 charges. To keep the pressure as low as possible, gate valve before the dipole magnet was opened only at the injection. Still, the reading of the BA gauge at the far end of the beamline became one order higher because of the gas flow from the ion source. (For the location of the gauge etc., see Fig.5.1.)

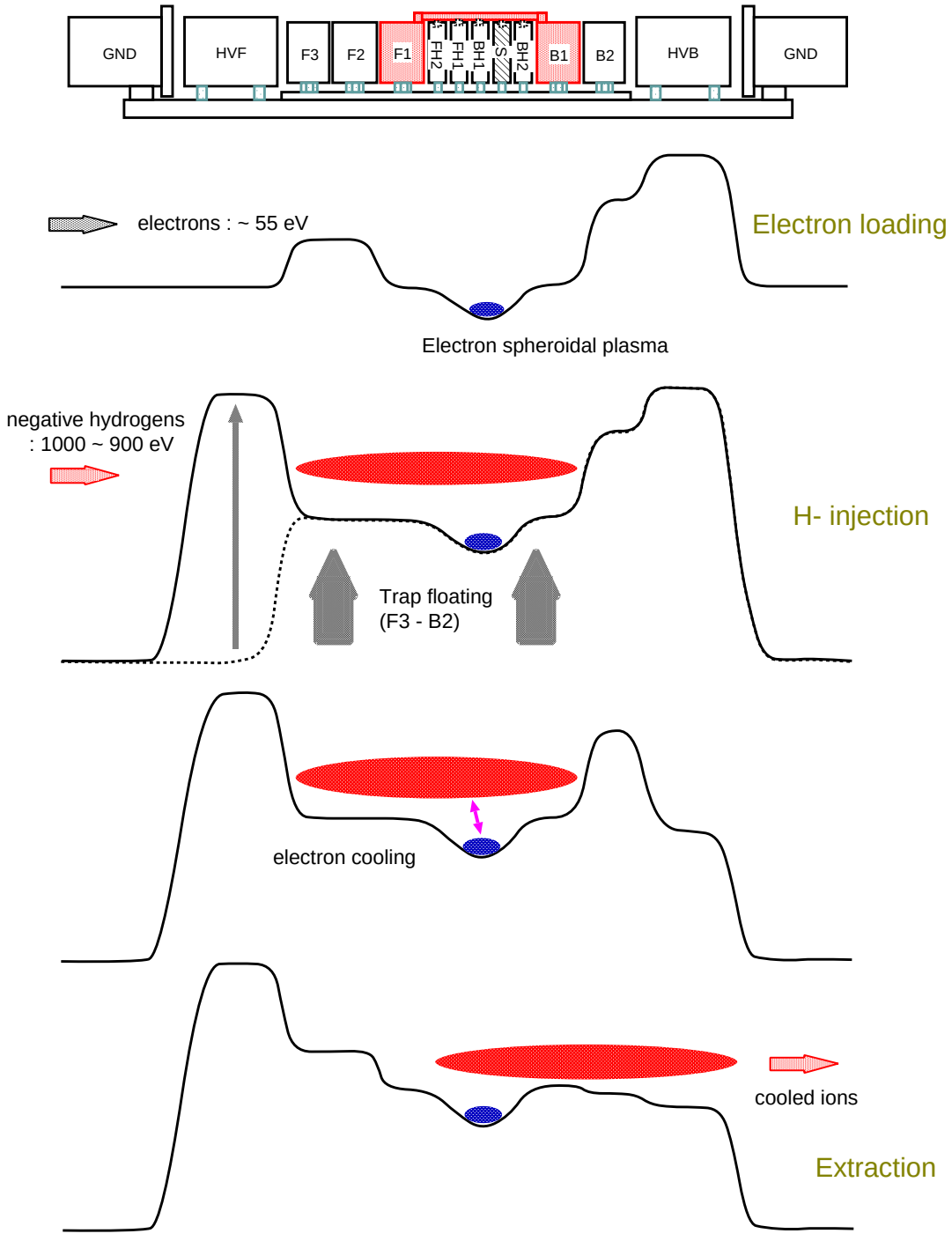

Figure 5.37: Potential change during the H^- cooling experiment. Lines correspond to a potential on the center axis. After certain cooling time, H^- ions were extracted, by reducing the voltage on the electrode "B2". In the case of rectangular potential, central dimple was not formed. Trap floating potential is defined as a potential given to the electrodes "F1" and "B2".

Fig.5.38 summarizes the measurements. It can be noted that, by forming the harmonic region, the confinement property was improved, although H^- ions were not trapped in the harmonic potential well, as schematically shown in Fig.5.37.

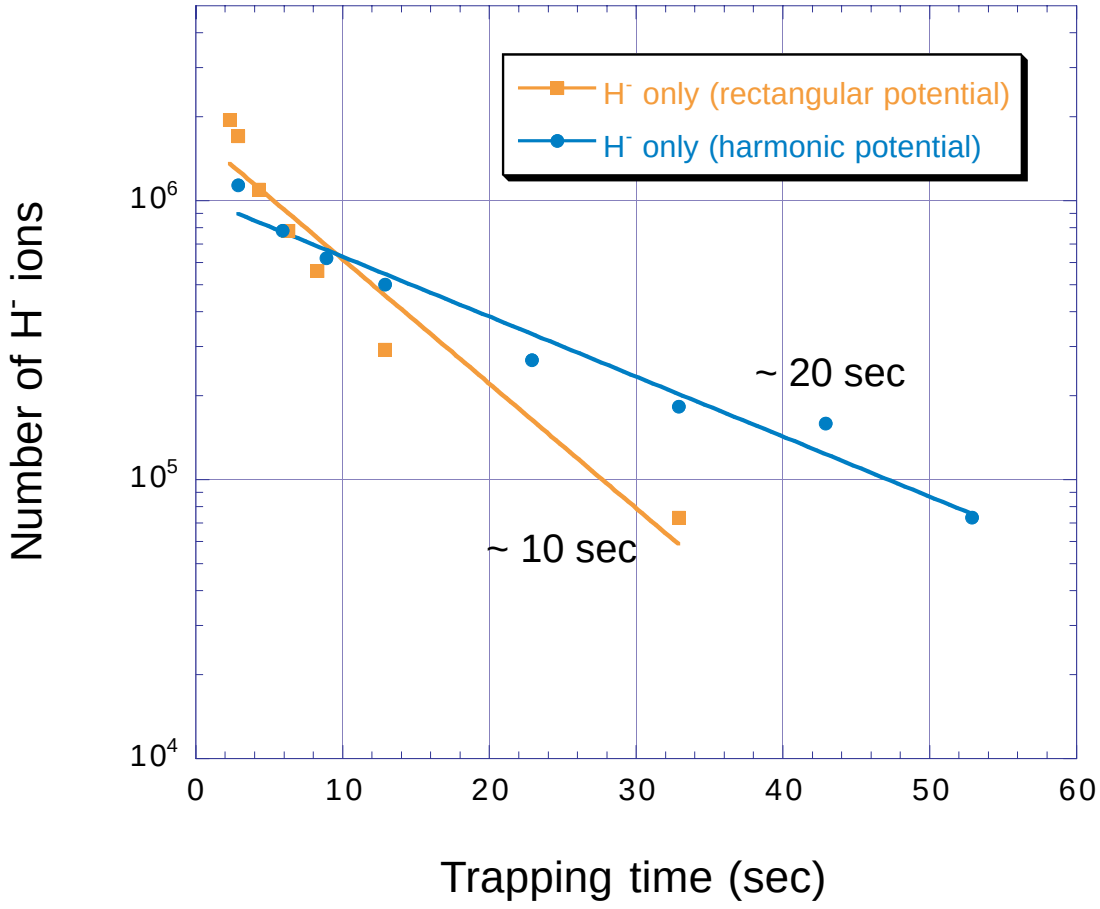

Figure 5.38: The number of H^- ions vs. trapping time. In the figure, "harmonic potential" means rectangular potential + harmonic dimple as shown in Fig.5.37.

5.7 Electron cooling of negative hydrogen ions

The injection-hold-dump and measure scheme is shown in Fig.5.37. Though eventually the energy of H^- ions will become the same as that of electrons, there was no effective way to experimentally separate H^- ions from electrons. Thus, to confirm the cooling by electrons, what we tried was to observe the shift in the energy distribution of H^- ions.

5.7.1 Decay time correction

Since the charge amplifier had a decay constant ~ 800 μsec, following correction has been made. Supposing a current integrator (Fig.5.39) with a time constant $\tau = RC$, output voltage $V(t)$, incoming current $I(t)$, the change of the output after a time interval δt is given by

$$CV(t+\delta t) = CV(t)\mathrm{e}^{-\frac{\delta t}{\tau}} + I(t)\delta t. \qquad (5.4)$$

Here, C is the capacitor in the integrator. Considering that δt is an infinitesimal quantity, to the first order of δt, we have

$$I(t) = \frac{CV(t+\delta t) - (1-\frac{\delta t}{\tau})CV(t)}{\delta t}. \qquad (5.5)$$

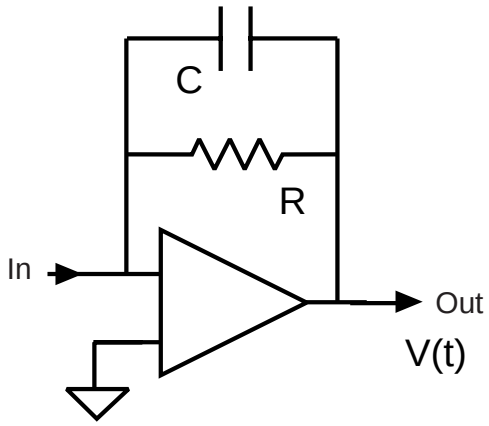

Figure 5.39: A schematic of a current integrator.

The raw signal is shown in Fig.5.40 and the corrected current in Fig.5.41. Spurious "negative" current was excluded by this correction.

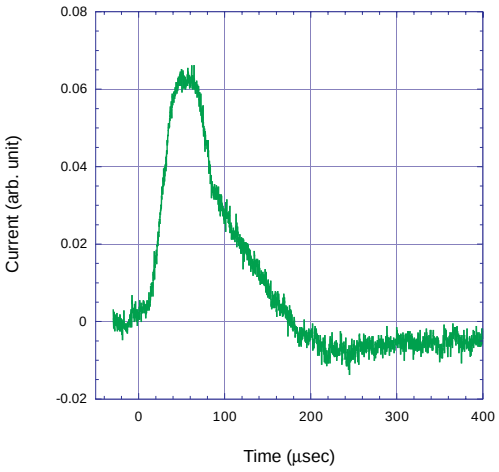

Figure 5.40: Without correction of decay constant.

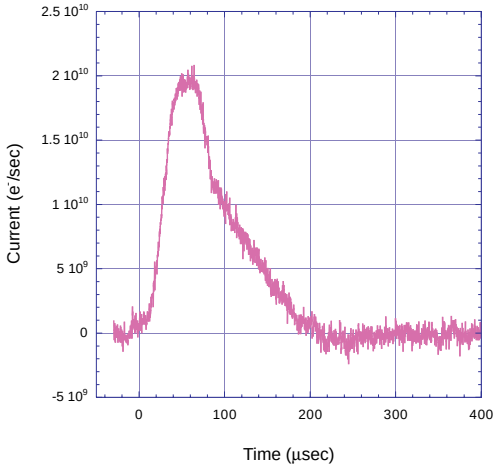

Figure 5.41: With correction of decay constant.

5.7.2 Change in the energy distribution of trapped H^- ions

Measured current of extracted H^- ions is shown in Fig.5.42. About $N_{H^-} = 2 \times 10^6$ H^- ions were injected. The abscissa correspond to the potential change of the electrode "B2" (V_{B2}). The correspondence is shown in the lower graph of Fig.5.42. Radial variation of the potential maximum is as in Table.5.3.

V_{B2} [V]	-1000.0	-950.0	-925.0	-900.0
Potential maximum at $r = 0$	-982.0	-938.7	-917.1	-895.5
Potential maximum at $r = 1$ mm	-982.1	-938.8	-917.1	-895.5
Potential maximum at $r = 6$ mm	-984.1	-939.9	-918.0	-896.0

Table 5.3: Radial potential variation. Potentials on neighboring electrodes were $V_{B1} = -875.0$ V and $V_{HVB} = -855.0$ V.

Since the TOF of both electrons ($\leq$ 200 ns) and of ions ($\leq$ 10 μs) from the trap to the Faraday cup were shorter than the time constant of potential change (slower than 1 V/μs), lower energy particles came later in time. In this sense, Fig.5.42 can be read as a graph of energy distribution of extracted H^- ions. Taking the difference of the peak position and the trap floating potential ($|V_f| = 890$ V), we can define the energy (in the direction parallel to the magnetic field) of the ion clouds in the trap. Hereafter, trap floating potential designates the potential given to the electrodes "F1" and "B1". For 0.9 sec trapping, the value was about 65 eV. In principle, there is no significant change in the shape as trapping time increases. That the number of higher energy ions seem to decrease faster is because of the higher detachment cross section.

In Fig.5.43, shown are energy distributions of H^- ions cooled by electrons. About $N_{H^-} = 2 \times 10^6$ H^- ions were injected into a cloud of $N_e = 1.5 \times 10^8$ electrons, that were prepared 70 sec before the injection of ions. The very existence of the slower (= lower energy) component exhibits the evidence of electron cooling. If we measure the temperature from the trap floating potential, initial 65 eV became 50 eV after 2.9 sec cooling, 30 eV after 5.9 sec cooling.

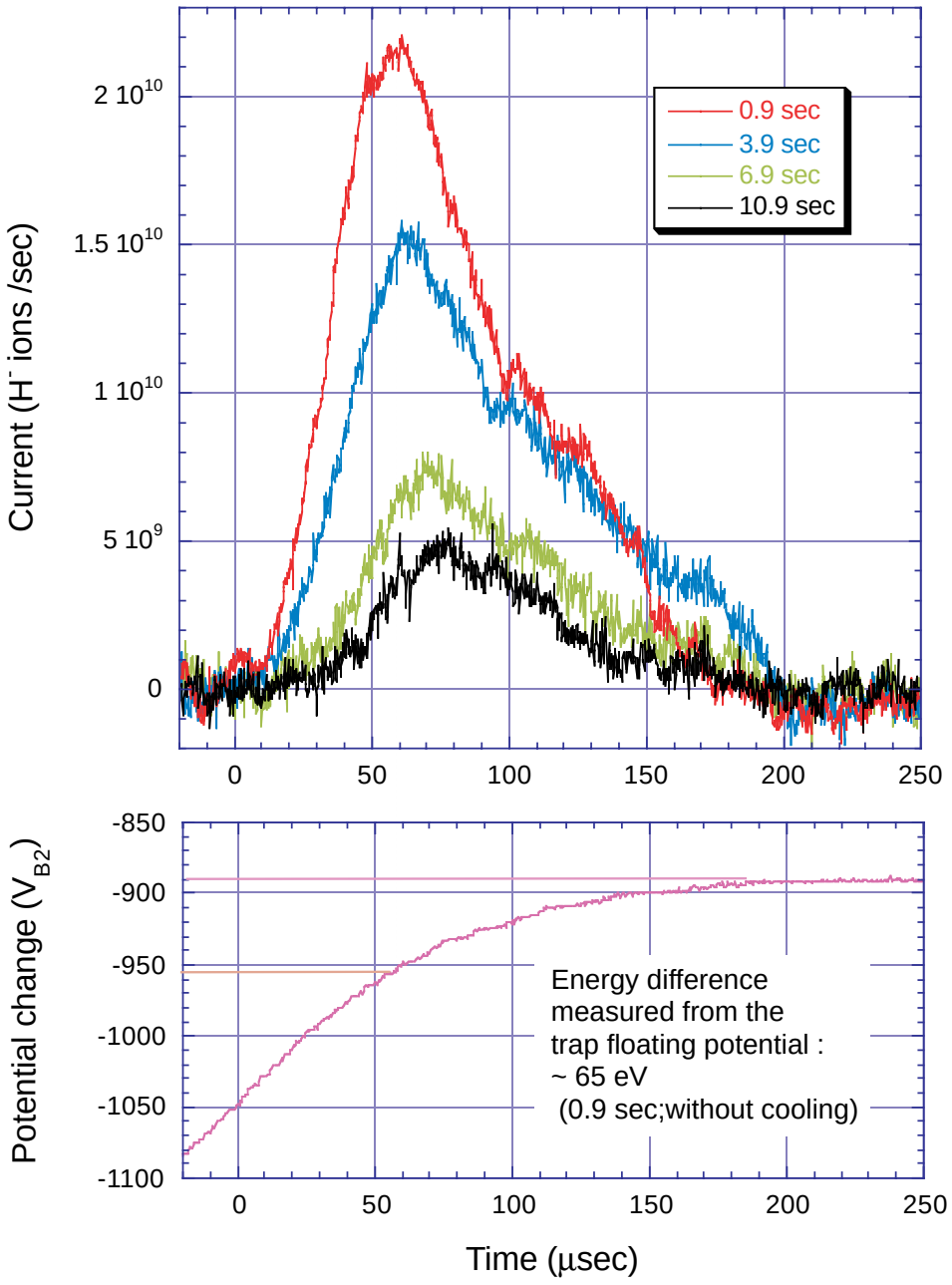

Figure 5.42: Current of H^- ions extracted from the trap. $N_{H^-} = 2 \times 10^6$. There was no major change in the energy distribution as trapping time increased.

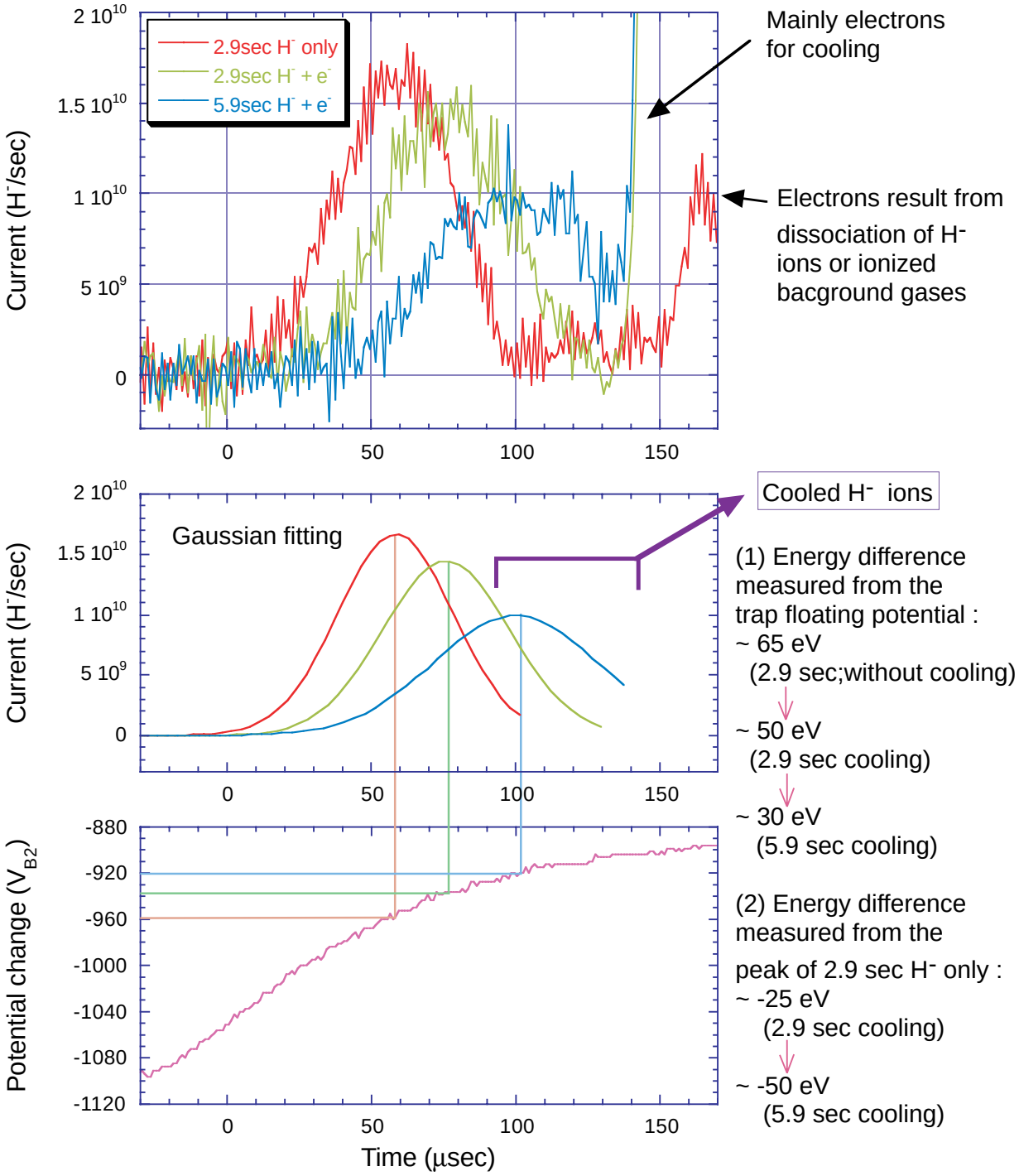

Figure 5.43: Electron cooling of H^- ions. $N_{H^-} = 2 \times 10^6$ and $N_e = 1.5 \times 10^8$. Electrons were prepared 70 sec before the injection of ions.

Moreover, the effect of rotating electric field was also observed (See below, Fig.5.44 and Fig.5.45). About $N_{H^-} = 2 \times 10^6$ H^- ions were injected into a cloud of $N_e = 9 \times 10^7$ electrons. For the measurements indicated by "H^- + e^-", electrons are preloaded 70 sec before the injection of ions. In the case of "H^- + e^- with rot-E", from after 60 sec of electron injection, a rotating field (2 MHz, 0.5 V) was applied for 120 sec. Then, ions were injected after an interval of 30 sec to let electrons be cooled. In these short time ranges, we can see that the high energy peak disappears as time passes and the low energy tail moves toward lower energy.

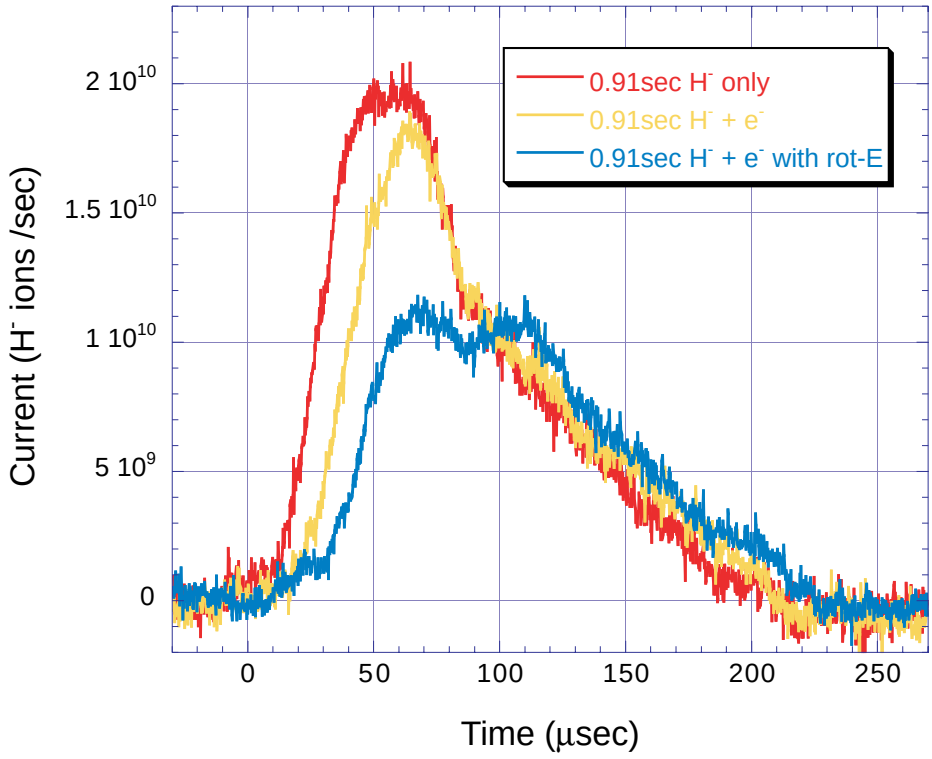

Figure 5.44: Energy distribution of H^- ions for 0.91 sec electron cooling. $N_{H^-} = 2 \times 10^6$, $N_e = 9 \times 10^7$.

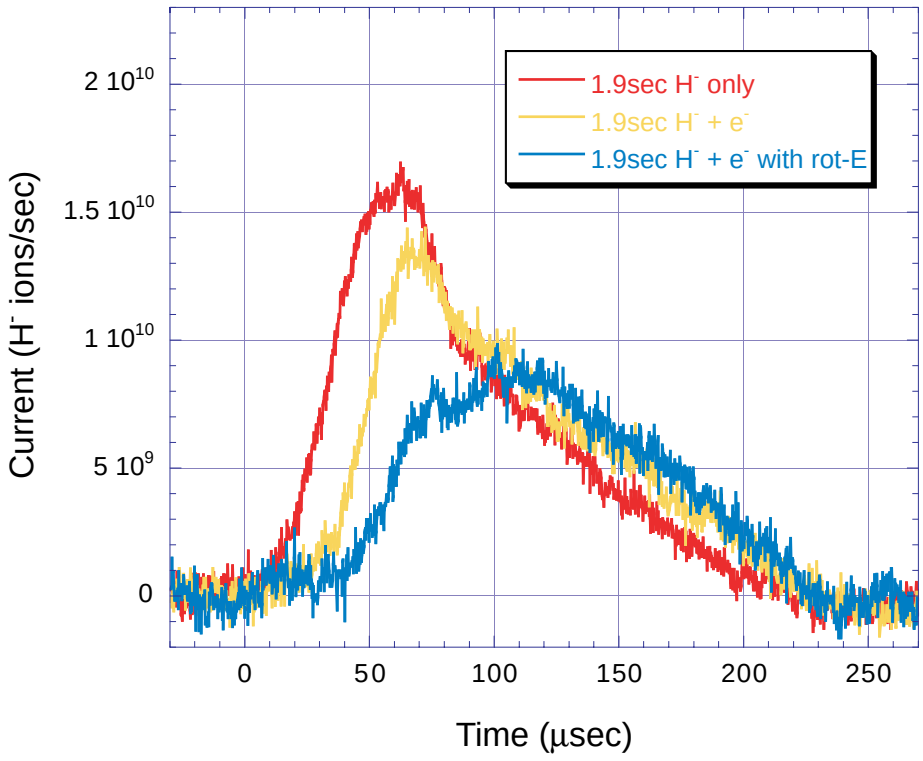

Figure 5.45: Energy distribution of H^- ions for 1.9 sec electron cooling. Other conditions are the same as Fig.5.44.

In Fig.5.46, shown is superposition of two graphs, "0.91 sec H^- + e^- with rot-E" from Fig.5.44 and "1.91 sec H^- + e^-" from Fig.5.45. As is schematically shown in the figure, the average diameter of electron plasmas without rotating field was about 12 mm and the incident ion beam had a diameter of 5 mm inside the trap. It can be seen that the decrease of the high energy peak is faster for the case with rotating field and the low energy tails are almost the same, which leads to the fact that cooling speed became more than two times faster when we compress the electron plasmas by the application of rotating fields. At least before the injection of H^- ions, when we applied the rotating field, effective (line-integrated) density of electrons became 20 times larger than the case without.

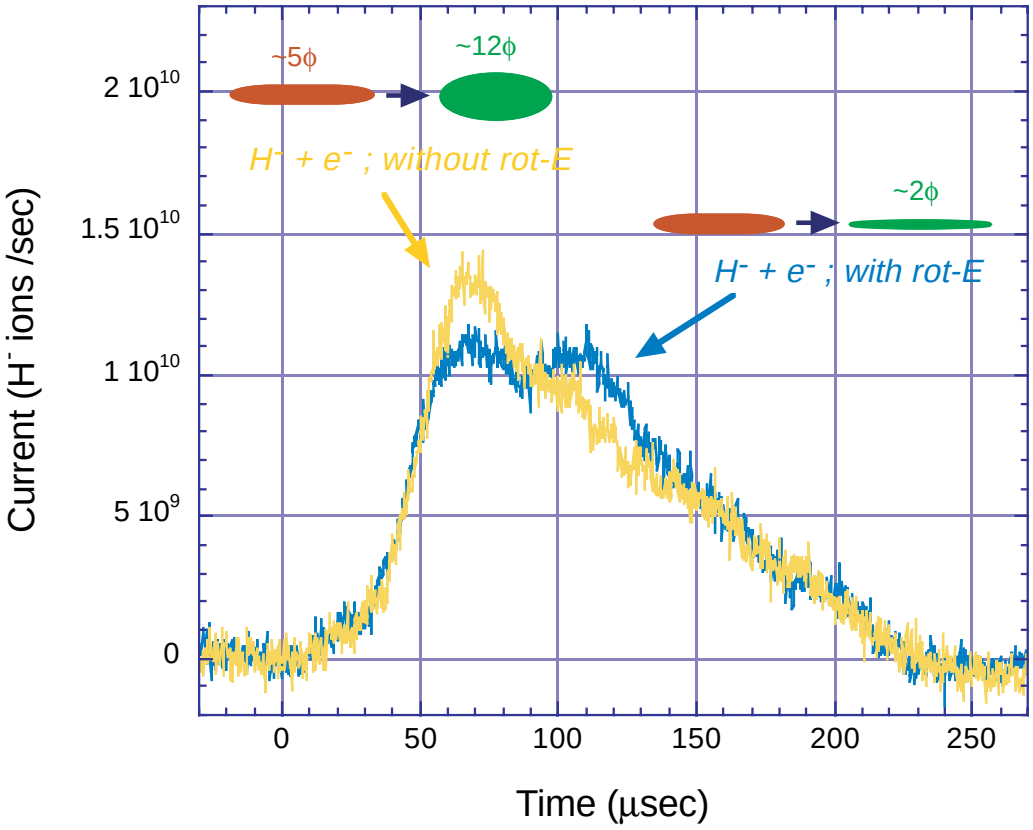

Figure 5.46: Effect of the compression of electron plasmas by rotating fields on the cooling speed of H^- ions.

5.8 Measurements of electron temperature

When we mix energetic ions with cold electrons, the temperature of electron plasmas will be shifted upwards, which indicates how the cooling proceeds. The temperature of electrons in the direction parallel to the magnetic field was estimated using a high-energy fraction of extracted electrons. We can surmise that it somehow reflects the temperature when the velocity distribution of a plasma is Maxwellian. We counted electrons according to their time of arrival at the Faraday cup until it reached about 5% of the total number. It was shown that the temperature can be determined with a formula below[89] in the case only high-energy electrons are used :

$$\frac{1}{e}\frac{d\log_{10} N}{dV_{B2}} = \frac{1.05}{k_B T}. \tag{5.6}$$

Fig.5.47 shows the change of potential and the number of extracted electrons vs. time. Analysis was done using only higher energy electrons, that came out from the trap earlier than others. Though there should be some high energy electrons resulting from detachment of H^- ions at a position with high potential, the rising shape of electron signals used in the determination of temperature does not seem to be affected so much.

In the following, there are three results shown : Fig.5.48 for electrons only - with a dummy trigger for H^- injection ($T_e = 0.8$ eV), Fig.5.49 for H^- cooling of 3 sec ($T_e = 2.9$ eV), and Fig.5.50 for H^- cooling of 6 sec ($T_e = 1.3$ eV). Analyzed was only the temperature of electrons in the direction parallel to the magnetic field. In the figures, drawn lines are the least square fit to exponential functions. We can see that cooled electrons (Fig.5.48) are heated by energetic H^- ions (Fig.5.49), then synchrotron radiation took the energy away (Fig.5.50). For the electron only case, without the dummy trigger, temperature of less than 0.4 eV was observed.

A numerical calculation was done with the input of experimental parameters : $B = 1$ T, $n_{H^-} = 1 \times 10^6$ cm^{-3}, $n_e = 5 \times 10^7$ cm^{-3} $T_{H^-}(0) = 100$ eV, $T_{e^-}(0) = 0.4$ eV(Fig.5.51). Here, a modification of the Eq.(4.3) was done so as to include the effect of background heating by electrical noise etc. ($T_{e_{bg}} = 0.4$ eV was used in the calculation.) With this additional term, the factor 8 used in Eq.(4.3) seems a few tens of percent larger than the value deduced from our measurements. This may come from another cooling mechanism like collision with residual gas molecules.

$$\frac{dT_p}{dt} = \nu_{pe}(T_e - T_p) \tag{5.7}$$

$$\frac{dT_e}{dt} = \nu_{ep}(T_p - T_e) - (T_e - T_{e_{bg}})A \tag{5.8}$$

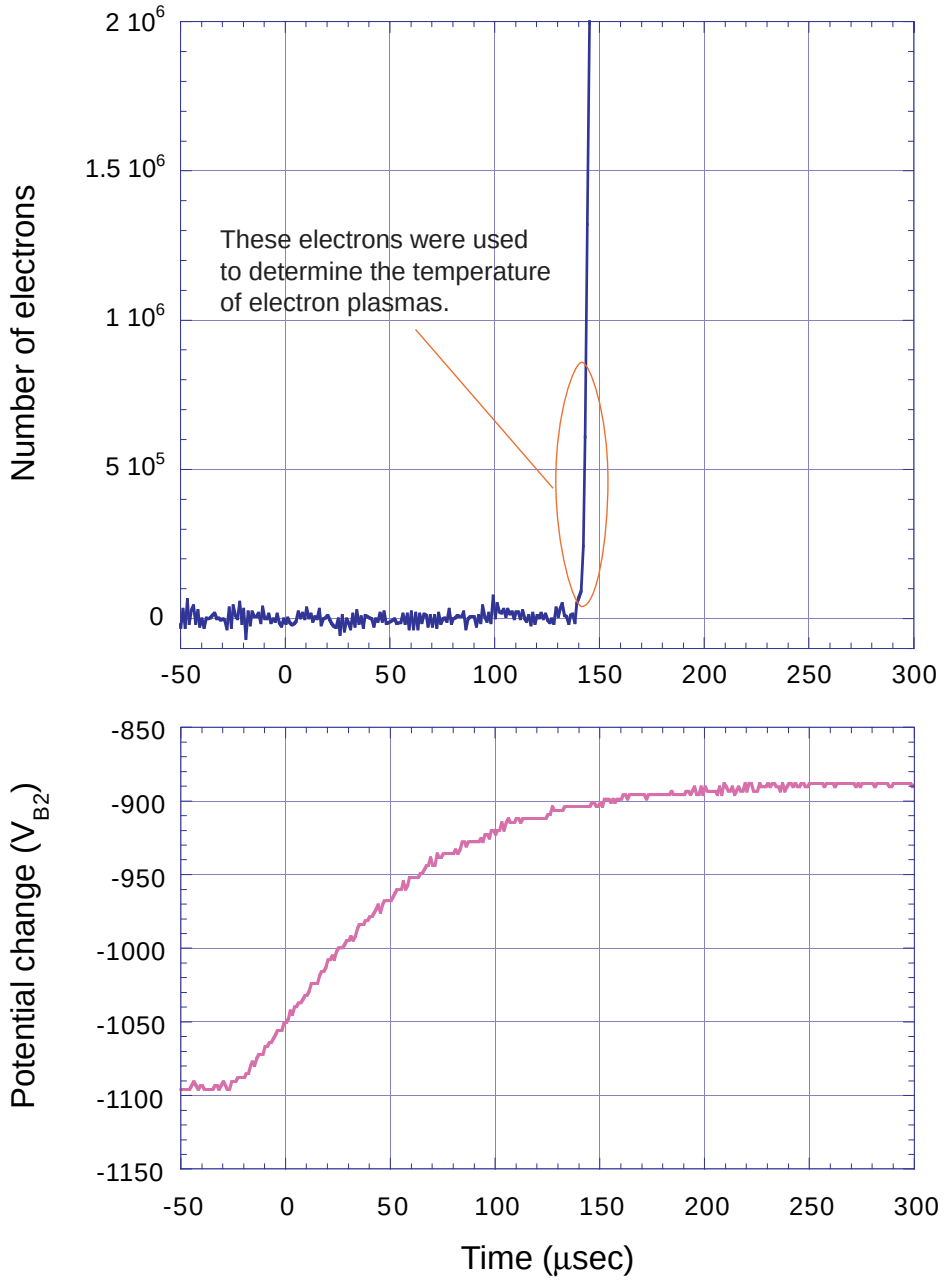

Figure 5.47: Change of the potential and of the number of electrons (integrated).

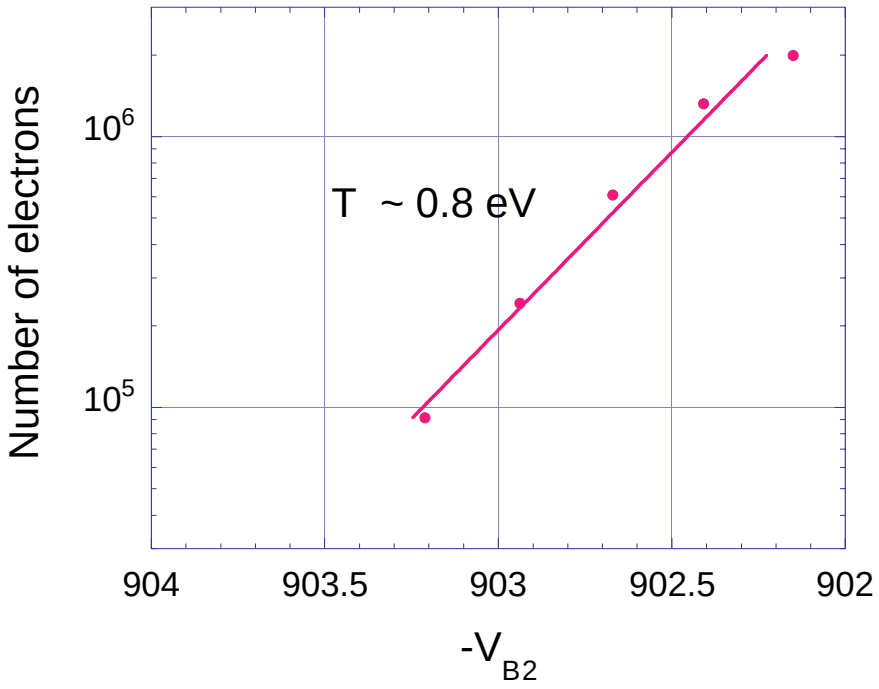

Figure 5.48: Electron temperature measurements ; electron only. Since the potential change *etc.* was the same as in the H^- trapping case, we can evaluate the temperature just before the injection of H^- ions. Drawn line is the least square fit to an exponential function.

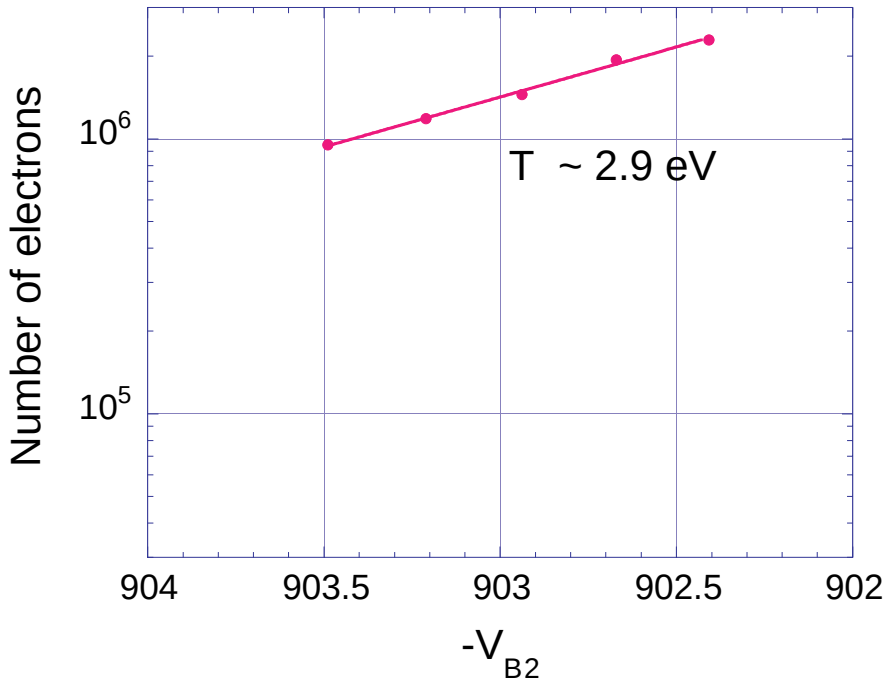

Figure 5.49: Electron temperature measurements ; with H^- cooled for 3sec.

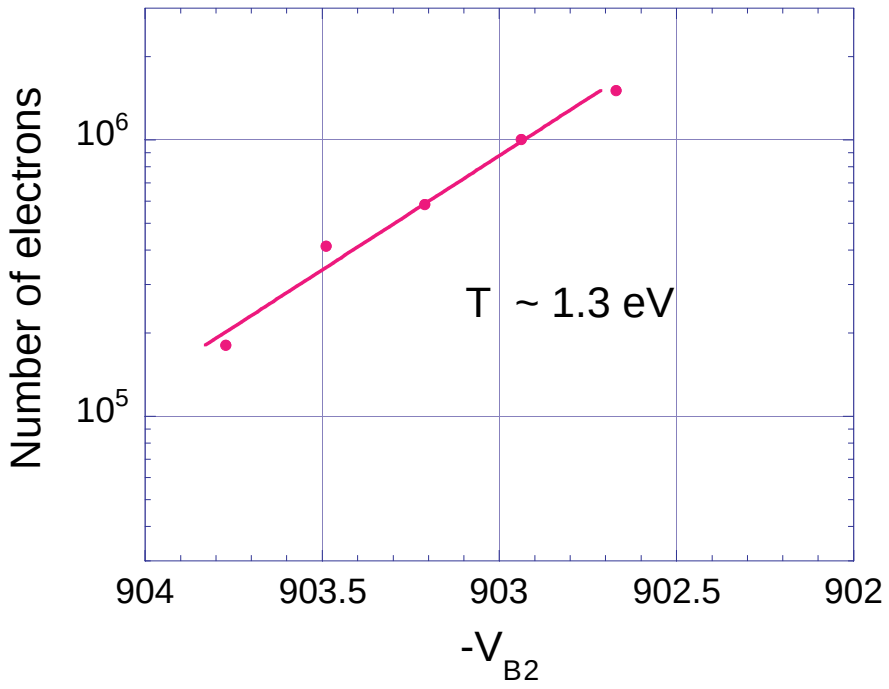

Figure 5.50: Electron temperature measurements ; with H^- cooled for 6sec.

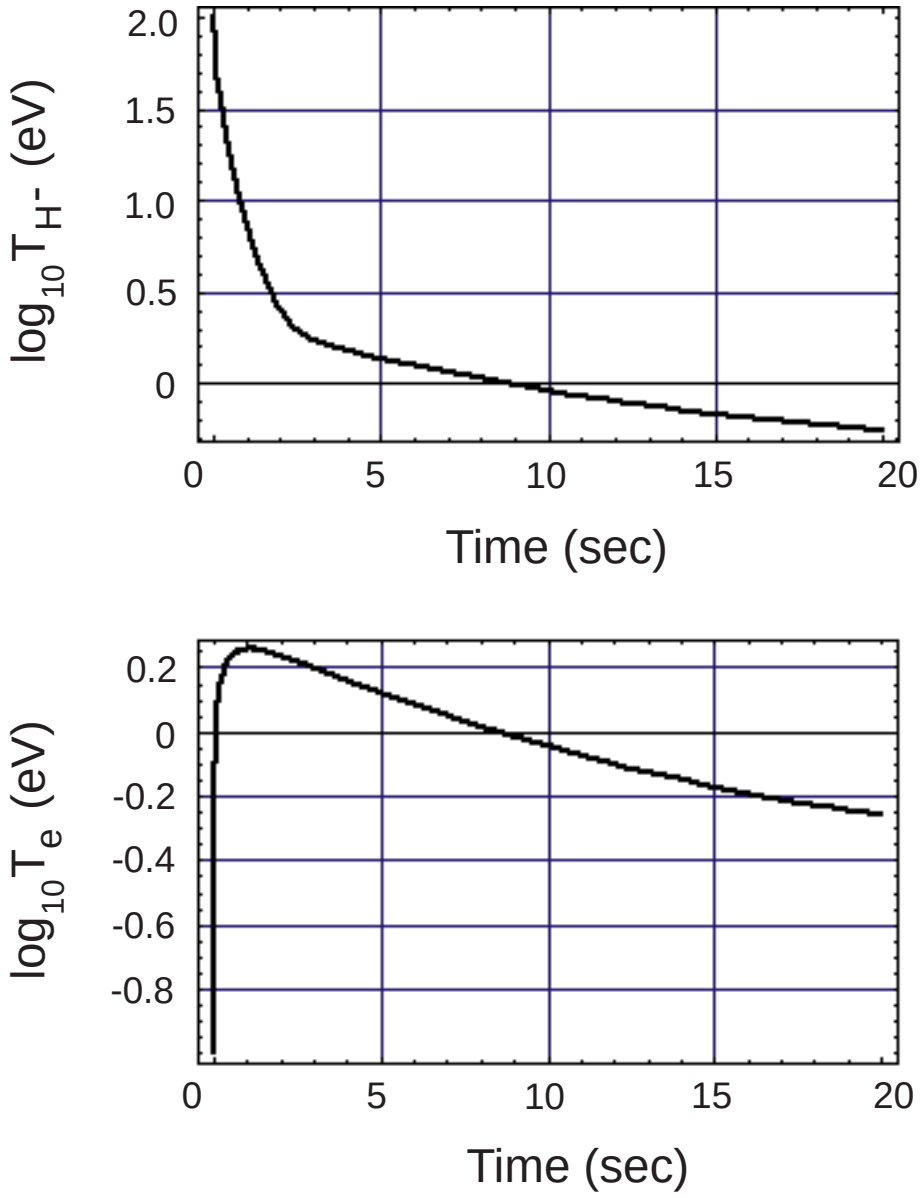

Figure 5.51: Numerical calculation of electron cooling of H^- ions.

We can see that the electrons are warmed up by the injection of ions and the temperature starts to decrease about one second after injection.

5.9 Possible non-destructive thermometer using (2,0) modes

The injection of energetic ions into a cold electron plasma caused an increase in the (2,0) frequency ω_{20} of the electron plasma (Fig.5.52). Comparing the temporal change of the (2,0) mode frequency with and without H^- ions, we find that initially increased frequency by the injection of ions comes back to lower as time passes. Time scale is approximately the same as the observation and calculation shown in Sec.5.8. To date, it seems there exist no other experiments which monitored the (2,0) frequency with this kind of beam injection into a cold plasma. Since ω_{20} is an increasing function of temperature[38], we thought that this can be used as an indicator of electron temperature. It should be noted that when we apply the rotating electric field, the radial density profile deviates significantly from the one of spheroidal plasmas. However, there is a report saying that ω_{20} is relatively insensitive to the radial profile in a similar system[36]. Further study on the relation between the radial profile and the temperature is necessary.

(2,0) mode ; no H^-

A plasma of $1x10^8$ electrons.

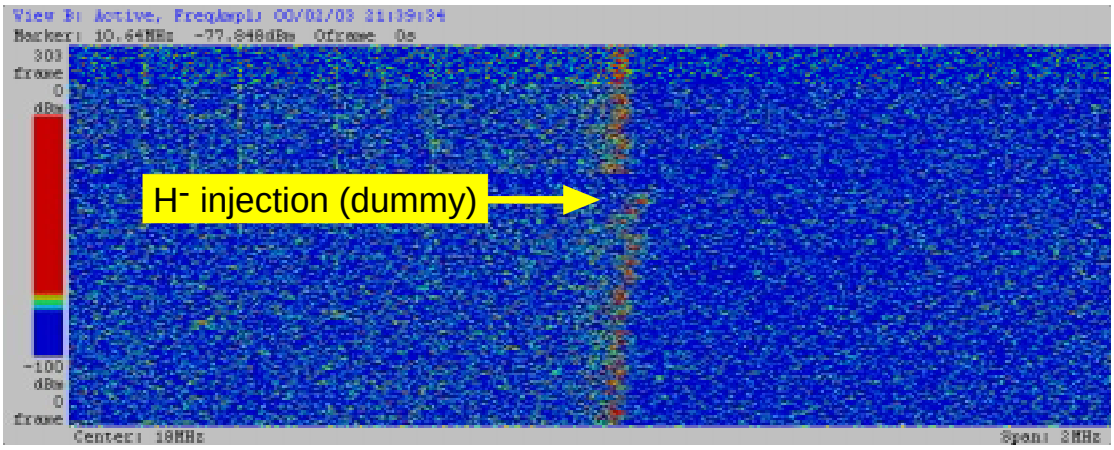

(2,0) mode ; with H^-

$5x10^6$ H^- ions injected into a plasma of $1x10^8$ electrons.

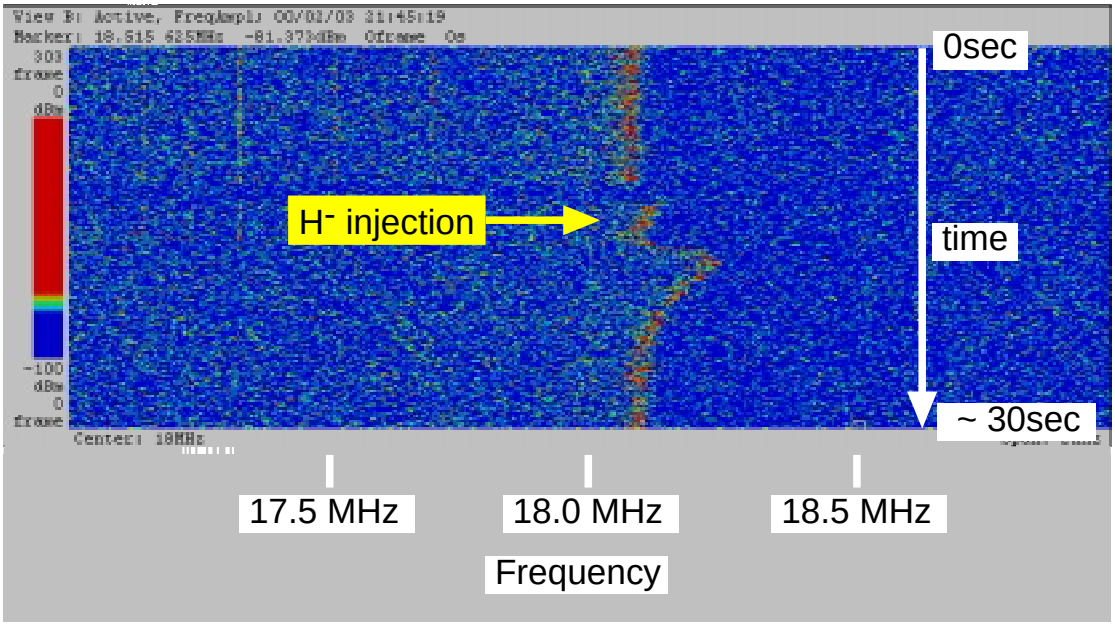

Figure 5.52: Effect of the injection of negative hydrogen ions into the electron plasma. In the upper figure, "dummy" means high voltage switching was done without injecting ions.

5.10 Radial compression of protons

Compression of proton clouds with rotating electric fields was tried and a shrink in the radial profile was observed, which gave an impetus to the extraction of trapped particles. The setup is shown in Fig.5.53. To convert ions into electrons, an MCP with a hole of 6 mm in diameter was located in front of a screen where the same combination of ZnO screen and ITO layer as in Fig.5.22 was used. Observed images are shown in Fig.5.53. In our experimental condition, the main component of the residual gas was hydrogen and plasmas were prepared by ionizing these hydrogen gas by electrons. It was found that created ion plasmas contain protons and H_3^+. To get the images shown in Fig.5.54, H_3^+ ions were expelled from the trap by exciting their axial oscillation.

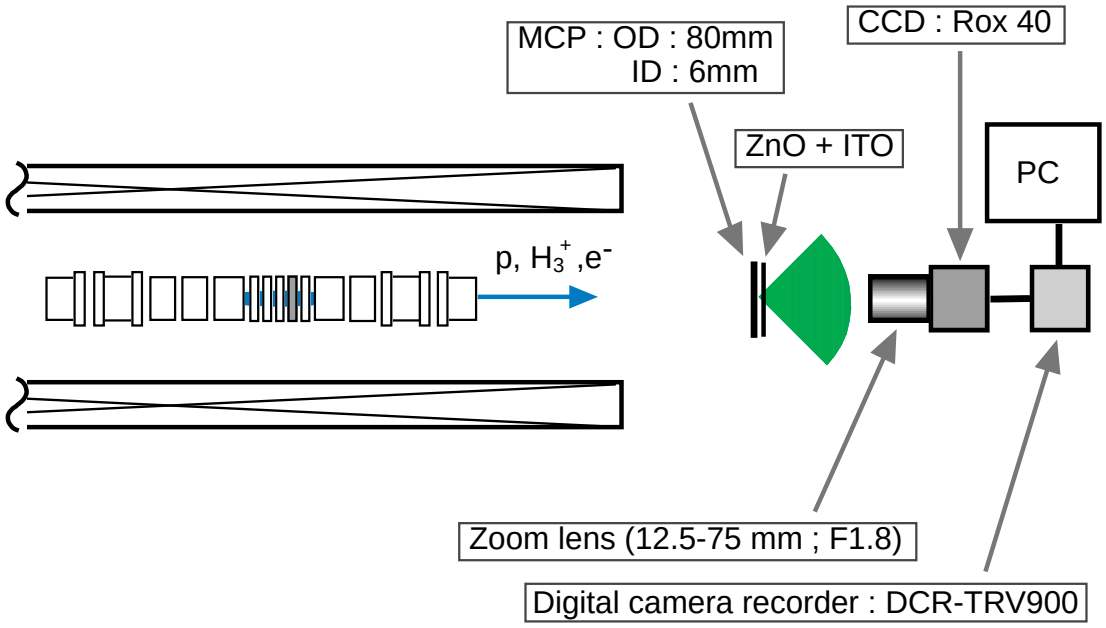

Figure 5.53: Experimental setup for the observation of radial profile of proton + H_3^+ plasmas.

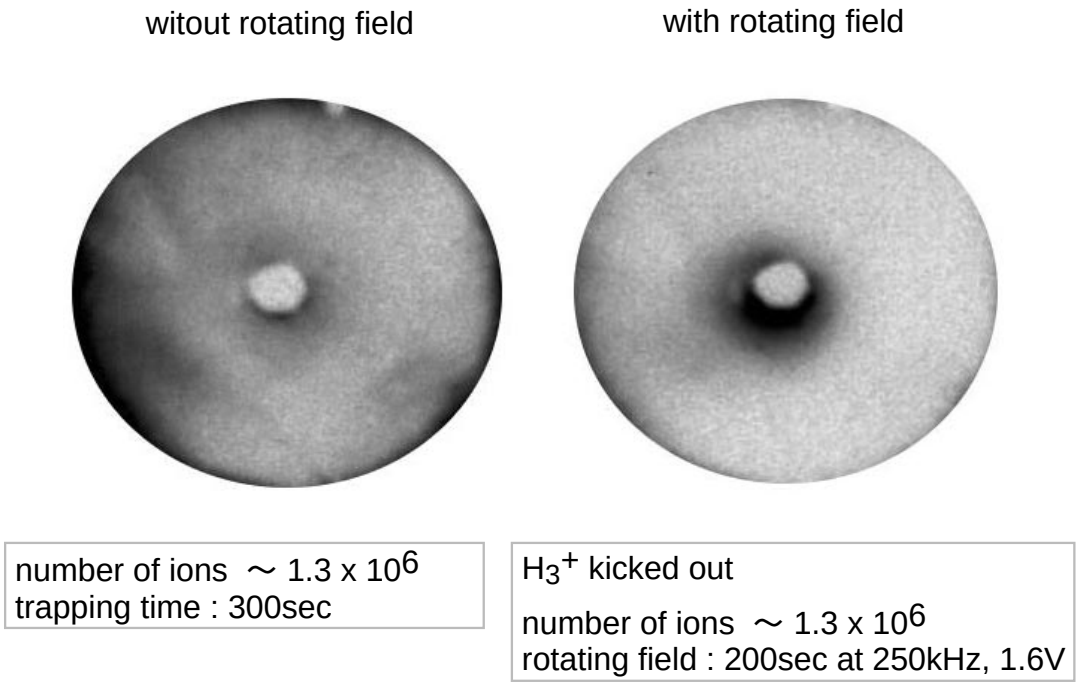

Figure 5.54: Observed profile of proton + H_3^+ plasmas.

Chapter 6

Summary and Conclusion

A new trap was developed for the realization of ultraslow antiproton beam. Below, achievements are enumerated.

1. For the construction of the trap, technical problems like heat conduction, material selection were considered. Ultra-high vacuum and low-temperature compatible, bakable, non-magnetic apparatus was designed and constructed.

2. Confinement property of the trap was checked. Under the magnetic field of 1 T, electrons are stored for more than 1400 sec, sufficient time to cool antiprotons. Having large harmonic potential, lifetime of electrons was about two times longer than the cylindrical case. Confinement of H^- ions was possible with a lifetime of 20 sec.

3. Control of the shape of electron plasmas was successful by applying proper rotating electric fields. The minimum diameter was less than 2 mm, within the requirement for the extraction of antiprotons. It was found that within the range from 1.5 MHz to 2.5MHz, rotating fields can effectively compress electron plasmas.

4. Electron cooling of 2×10^6 H^- ions was demonstrated for the first time. Change of the energy was determined by comparing the peak position measured from the trap floating potential and cooling time was estimated to be 6 sec for $N_{H^-} = 2 \times 10^6$ and $N_e = 1.5 \times 10^8$. It confirmed that the electron cooling of antiprotons will be possible. By compressing the coolant electron plasma, we could accelerate the cooling by more than a factor of two. This is the first demonstration that utilization of rotating electric field was applied to the cooling of particles. This will save the time so that we can have cooled antiprotons within pulse intervals at AD.

5. A possibility was shown that the plasma (2,0) mode can be used as a non-destructive thermometer for plasma diagnostics.

6. Compression of proton clouds was successful.

For some reason, until very recent, there seemed little interaction between physics with single particle traps and nonneutral plasma physics, though their method was somehow similar. Here, techniques and experiences in wide area of physics are gathered to produce intense beam of ultracold antiprotons. We could call it syncretisme. Antagonist?

Chapter 7

Future works

Before the shipment of the system to CERN, various extraction way will be tried searching the most efficient manner. Transport efficiency and beam emittance will be evaluated through the experiments with protons.

Practically, it is necessary to prepare slow antiprotons within a pulse interval at AD. Effect of rotating electric field will be reconfirmed and optimization of the density of electrons etc. will be done in the first moment after the installation of apparatus at AD.

7.1 Planned improvements

7.1.1 Magnet replacement

Replacement of the superconducting magnet will be done by the end of the year 2000. With essential specifications listed in the Section 4.8.1 unchanged, following improvements are expected.

1. Modifications to the radiation shields and support assemblies of helium reservoirs in order to reduce the heat load.
2. Addition of a hot gas inlet for more effective baking.
3. End flanges will be assembled so that they are parallel to each other and perpendicular to the center line within the tolerance of $\pm 0.3^{\circ}$.

7.1.2 Addition of another segmented electrode

(1) For the detection of plasma modes which have azimuthal structure under the influence of rotating electric field, or (2) to apply the rotating field at both ends of the plasma, it would be meaningful to replace one of the ring electrode with a set of segmented one. It has already been prepared for future use.

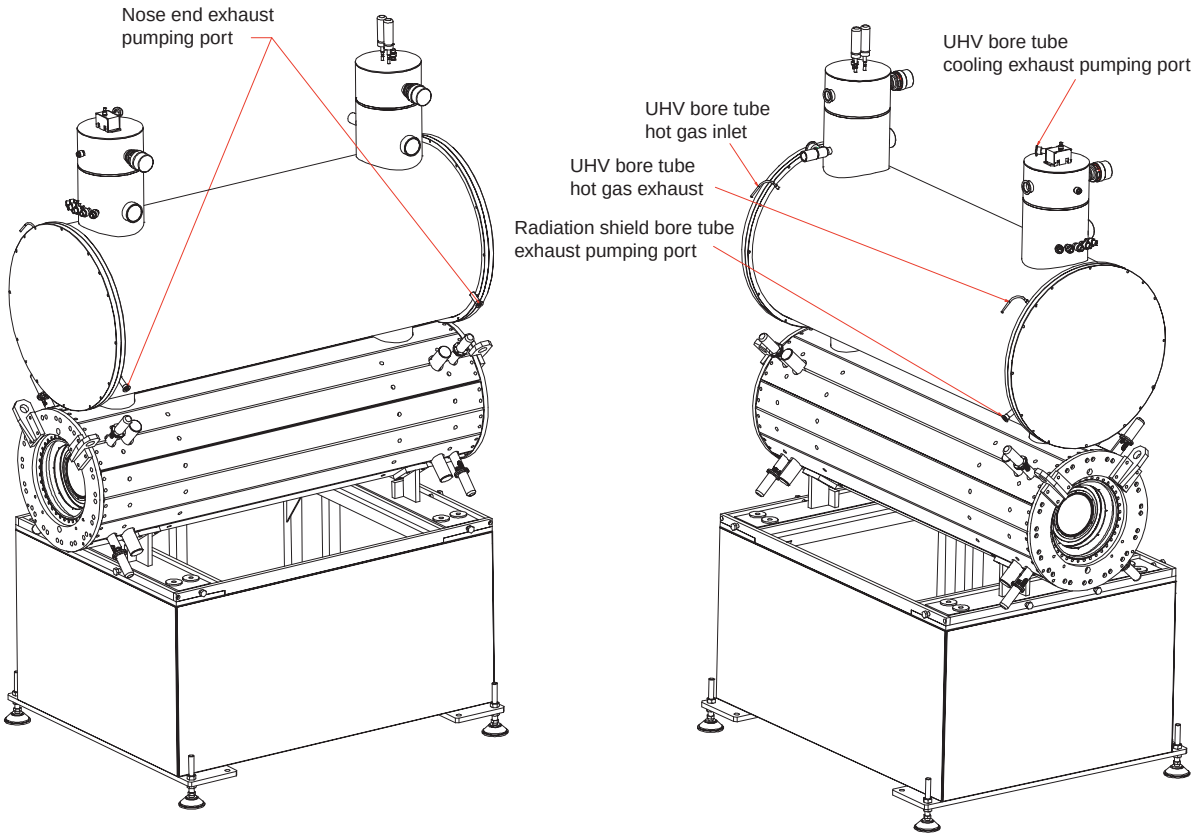

Figure 7.1: Superconducting solenoid - sketches

Acknowledgement

First of all, I would cordially like to show my gratitute to Prof.Dr.YAMAZAKI Yasunori for his guidance and continuous encouragement. I really learned a lot, not only physics. For me, the existence of another professor, Prof.Dr.KOMAKI Ken-ichiro was significant. From him, I got lots of eye-opening suggestions.

Prof.Dr.MOHRI Akihiro, who invented the Multi-ring electrode trap, considerably helped us in designing the ASACUSA trap. I got lots of hints both on physics and techniques.

I gratefully acknowledges Dr.HIGAKI Hiroyuki for helpful discussions and criticism. I also indebted to several other members of the group: to Mr.KUROKI Kenro for his skill in electronics, to Dr.OSHIMA Nagayasu for the preparation of the experiments, to Dr.HORI Masaki for data taking programming, to Dr.YOSHIKI FRANZÉN Ken, Dr.WANG Zhigang, and Mr.ÚJVÁRI Balázs for their participation in the experiment, and to Mr.KURODA Naofumi for making some of the electronics. The former research associate of our laboratory, Prof.Dr.AZUMA Toshiyuki and present research associate, Dr.TORII Hiroyuki A. assisted me in various situations. Ms.ONUMA Michiko and Ms.TOYODA Hisako saved us from tremendous administrative works.

For the incomplete magnet system, we needed to use enormous amount of liquid helium to keep experiments running. We owe people in the cryogenic laboratory, Mr.ODASHIMA Yutaka, Mr.ISHIDA Akinori, Ms.ASHIZAWA Yoshiko for continuous supply of it. Without their continuous support, this work would never be completed.

Former members of the trap group, Mr.MATSUSHIMA Hiroshi and Mr.YAMASHITA Kenya assisted the experiments with a prototype. Before a new project is put on track, piles of works should be done, although they do not necessarily lead to visible achievements. However, it does not mean those works are forgettable. During these experiments with the prototype we settled ourselves in RIKEN, and people there helped us a lot: Dr.KAMBARA Tadashi, Dr.KANAI Yasuyuki, Dr.Kojima Takao M., Dr.NAKAI Youichi, Mr.Oyama Hitoshi, Ms.NISHIDA Masami, and Ms.KURAMOCHI Chikako. A Helmholz magnet was kindly lent to us by Prof.Dr.NISHIYAMA Kusuo at KEK.

Discussion with Prof.Dr.TOTSUJI Hiroo about the centrifugal separation of multi-component plasmas lead me to understand the problem. Theoretical cooperation by

Prof.Dr.ICHIKAWA Yukikazu, Prof.Dr.SHIMAMURA Isao, and Dr.ICHIMURA Jun enriched my study.

I also want to show my thanks to Nichia Kagaku Kogyo K. K. for supplying us with ZnO powder, Asahi Glass Co., Ltd. for ITO screens.

I would like to show my special thanks to my collegues, Dr.ITO Takaomi, Mr.MORISHITA Yuichiro and Mr.TAKAHIRA Toshiyuki. We entered the labratory in the same year, from different places and wiht different backgrounds. It was nice to exchange our knowledges.

I often got enlightened and got encouraged in daily conversations with former lab members Dr.NINOMIYA Shiro, Dr.MAKI Kohske, Mr.TSURUTA Yoshiyuki and present members Mr.IWAI Yoshio, Mr.OKABAYASHI Norio, Mr.TAKABAYASHI Yuichi, Ms.ENDO Atsumi, Mr.MURAKOSHI Dai, Mr.YONEDA Satoshi.

In the end, I want to mention the ceaseless support by my family, especially by my parents, ICHIOKA Shohei and ICHIOKA Yuki. They managed to bring up a dreamy, rather sensitive boy to get a Ph.D. in physics. It is, something.

Appendix A

Charged particle traps

Charged particle traps have been versatile tools in various fields.
Collision experiments[90], magnetic moment[91] or g-factor[92] measurements, comparison of charge-to-mass ratio[6], creation of high density plasma aiming at fusion[93], neutron life time measurements[94], etc. Compared with Paul trap, Kingdon trap, etc., Penning trap has been preferred in the case of mass spectroscopy or antimatter physics. In the case of antiprotons, application of electron cooling technique facilitated the creation of cooled antiprotons inside the trap. The reference by Ghosh[95] includes a well-organized chronological bibliography during the period from 1936(original paper by Penning) to 1993.

A.1 Penning trap

Here, let us specially take a Penning trap[96], which is relevant to later sections. There exists an excellent review by Brown and Gabrielse[97].

A.1.1 Modified cyclotron frequency

Take a configuration of electrodes as in Fig.A.1. The z-axis is the center of evolution of electrodes.

Take a Cartesian coordinate (x, y, z) and consider a particle with charge q in a Penning trap. Electric potential to form a harmonic field in the vicinity of the trap center may be described by

$$\Phi = V_0 \frac{2z^2 - \rho^2}{2L_0^2 + b_0^2} = V_0 \frac{z^2 - \frac{\rho^2}{2}}{2d^2} \tag{A.1}$$

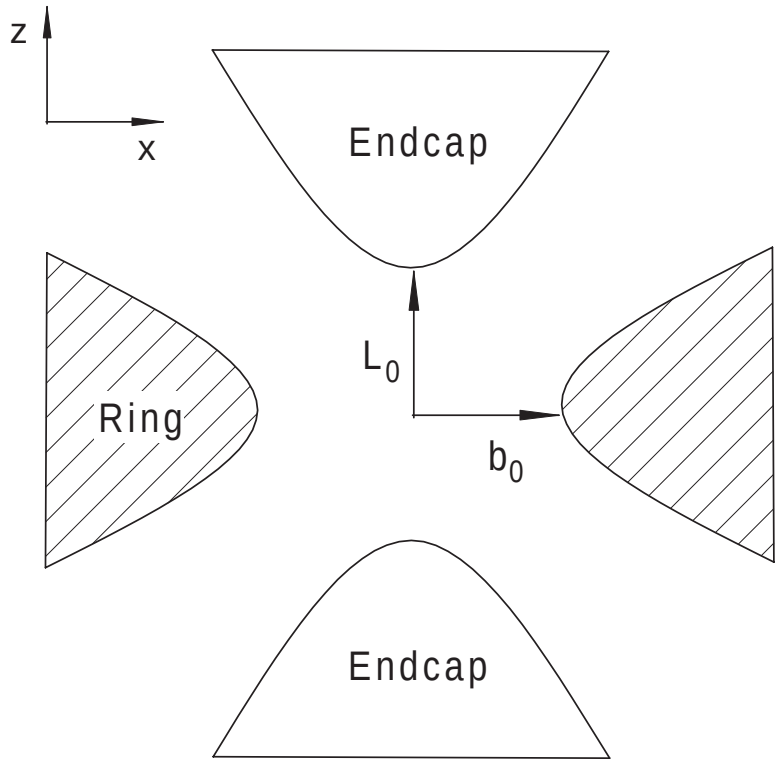

Figure A.1: Electrode configuration of an orthodox Penning trap.

Here, $\rho = (x^2 + y^2)^{\frac{1}{2}}$ and

$$d^2 \equiv \frac{1}{2}\left(L_0^2 + \frac{b_0^2}{2}\right). \tag{A.2}$$

The quantity d is often reffered to as a characteristic length of the trap.

In the non-relativistic case, the Lagrangian of a charged particle in the field can be written

$$\mathsf{L} = \frac{1}{2}mv^2 - q\Phi + q\mathbf{v}\cdot\mathbf{A} \tag{A.3}$$

where A is a vector potential. In the case of a constant magnetic field, we can write

$$\mathbf{A} = \frac{1}{2}\mathbf{B}\times\mathbf{r}. \tag{A.4}$$

Now let us assume that the magnetic field is in the z-direction, $\mathbf{B} = (0, 0, B)$. With Eq.(A.4) we can rewrite the Eq.(A.3) as

$$\begin{aligned} \mathsf{L} &= \frac{m}{2}(\dot{x}^2 + \dot{y}^2 + \dot{z}^2) - q\Phi + q\mathbf{v}\cdot\mathbf{A} && \text{(A.5)} \\ &= \frac{m}{2}(\dot{x}^2 + \dot{y}^2 + \dot{z}^2) - qV_0\frac{2z^2 - x^2 - y^2}{4d^2} + \frac{qB}{2}(x\dot{y} - y\dot{x}). && \text{(A.6)} \end{aligned}$$

Defining $\omega_z^2 \equiv \frac{qV_0}{md^2}$, Euler-Lagrange equation $\frac{d}{dt}\frac{\partial \mathsf{L}}{\partial \dot{q}} - \frac{\partial \mathsf{L}}{\partial q} = 0$ becomes

$$\ddot{x} - \omega_c \dot{y} - \frac{1}{2}\omega_z^2 x = 0 \tag{A.7}$$

$$\ddot{y} + \omega_c \dot{x} - \frac{1}{2}\omega_z^2 y = 0 \tag{A.8}$$

$$\ddot{z} + \omega_z^2 z = 0 \tag{A.9}$$

In z-direction, there is a harmonic potential and the particle oscillates at the frequency ω_z.

Now let us define a new variable $u = x + iy$. By subtracting Eq.(A.8) multiplied by i from Eq.(A.7), we can rewrite these equations into one :

$$\ddot{u} + i\omega_c \dot{u} - \frac{1}{2}\omega_z^2 u = 0. \tag{A.10}$$

By assuming a solution in the form of $u = \rho e^{-i\omega t}$, following characteristic equation is obtained,

$$2\omega^2 - 2\omega_c \omega + \omega_z^2 = 0 \tag{A.11}$$

with the roots

$$\omega_\pm = \frac{1}{2}\left(\omega_c \pm (\omega_c^2 - 2\omega_z^2)^{\frac{1}{2}}\right). \tag{A.12}$$

Here,

$$\tilde{\omega_c} \equiv \omega_+ = \frac{1}{2}\left(\omega_c + (\omega_c^2 - 2\omega_z^2)^{\frac{1}{2}}\right) \tag{A.13}$$

is a modified cyclotron frequency and

$$\omega_m \equiv \omega_- = \frac{1}{2}\left(\omega_c - (\omega_c^2 - 2\omega_z^2)^{\frac{1}{2}}\right) \tag{A.14}$$

is called a magnetron frequency.

In short, because of the existence of radial electric field, centripetal force on the particle is shifted by that amount so that the cyclotron frequency is reduced to

$$\tilde{\omega_c} = \omega_c - \omega_m. \tag{A.15}$$

A.1.2 Invariant theorem

Between the observed three frequencies and a calculated cyclotron frequency, there is a relation

$$\omega_c^2 = \tilde{\omega_c^2} + \omega_z^2 + \omega_m^2. \tag{A.16}$$

This is quite useful to determine a frequency from others or to check the consistency of the experiments. In most of the realistic Penning traps, a hierarchy $\omega_m \ll \omega_z \ll \omega_c$ holds.

A.1.3 Numerical summary

As an example, given below is a numerical summary of the PS200 Penning trap. (TableA.1)

External Parameters	
Trap potential	$V_0 = 80 \sim 120\, V$
Trap size	$d = \sqrt{\frac{1}{2}(L_0^2 + \frac{1}{2}b_0^2)} = 1.605 \times 10^{-2}$ m
Field strength	$B = 3.25$ T

Frequencies		
	For electrons	For antiprotons
Cyclotron	$\omega_c = \frac{eB}{m_e}, \nu_c = \frac{\omega_c}{2\pi} = 90.98$ GHz	$\nu_c = 49.55$ MHz
Axial	$\omega_z = \sqrt{\frac{V_0 q}{m_e d^2}}, \nu_z = 30.70$ MHz	$\nu_z = 715.8$ kHz

Table A.1: Various parameters for the trap. In the case of traps consiste of cylindrical electrodes, V_0 is different from potential difference between the Ring and Endcap. In some papers, used is a geometrical factor which corresponds to a ratio between an applied potential on electrodes and effective potential on the center axis.

Appendix B

Test experiments with a prototype

Construction of a Penning trap and a series of experiments were performed precedent to the main experiments. In this section, reviewed is what we learned from the experiments with that prototype.

B.1 Construction of a Penning trap with cylindrical electrodes

A Penning trap with cylindrical electrodes was constructed on the recipe in the reference by Gabrielse and Mackintosh[98]. In addition to the ring and two endcaps, there are two compensation electrodes to make the potential quadratic. Electrodes were made of phosphor bronze and the surface was gold plated[1].

B.2 Apparatus

A Helmholtz coil was utilized to produce a magnetic field necessary for the radial confinement of particles. The maximum field strength of 480 Gauss was determined by the power supply used. A vacuum chamber which was independently fixed on the floor was located along the axis of field symmetry (Fig.B.1).

As an electron gun, a cathode ray tube for oscilloscope (TOSHIBA ; FM150BT-A4) was used.

[1]The thickness of $2 \sim 3\mu$m was decided from the condition that the coverage should be 100% while there should be no crack. It can be noted that there exists a way of gold-plating with Se to obtain a shiny surface, which we avoided from the vacuum point of view.

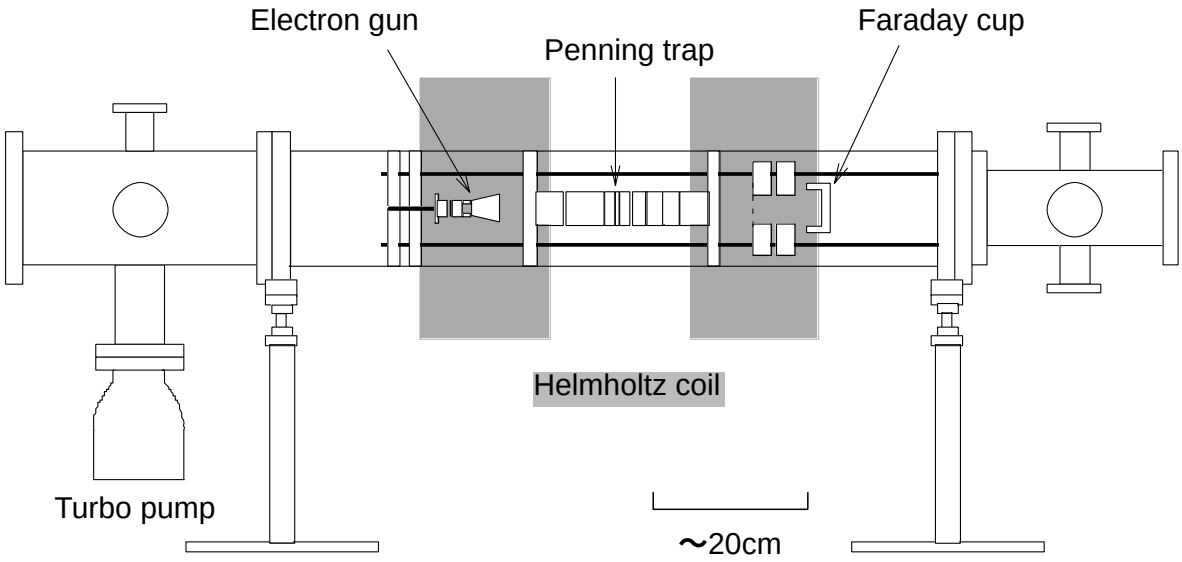

Figure B.1: Apparatus for the experiments with an orthogonalized Penning trap.

B.3 Experiments

B.3.1 Trap alignment against the magnetic field

For the alignment purpose, a thin copper wire of 0.3 mm in diameter was stretched along the trap (mechanical) axis. By making a flow of 50 Hz line current, we forced it to vibrate (See Fig. B.2)[2]. Positioning was done so that the amplitude of that oscillation became smallest and we defined such state to be aligned. From the observation by eye, we believe that the sensitivity to the change in position was as good as the thickness of the wire.

B.3.2 Confinement of electrons

Potential on each electrode was given by dividing the output of a power supply using resistors. Electrons emitted from the electron gun were captured and released after certain time (Fig.B.3). The pressure in the experimental chamber was in the range of 10^{-10}Torr with cold cathode gauge.

In a time range shorter than 1 sec, we observed an increase in the number of trapped electrons. It was attributed to ionization of residual gas by electrons[99].

Fig.B.5 shows the confinement property of the trap in the case of harmonic and cylindrical trap.

[2]Of course we could have resonated the normal mode frequency to 50 Hz by adjusting the tension, but this was not necessarily essential.

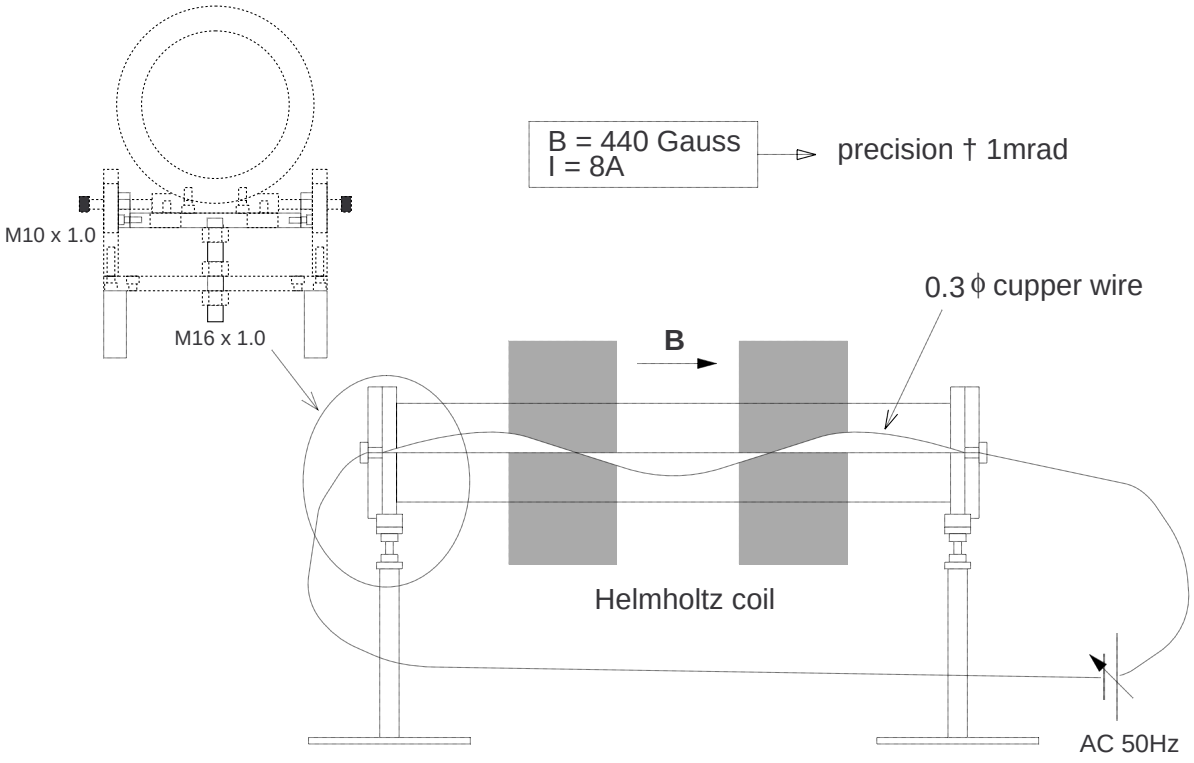

Figure B.2: Alignment of the trap axis to the magnetic field.

B.3.3 Extraction of electrons

Then, pulse extraction of trapped particles was tried. The potential shape was changed in the manner that the bottom of the potential was raised stepwise, as shown in Fig.B.6. Results are given in Fig.B.7. In this case, we reduced the trap potential in twenty steps of 15 ms interval. Here, we clearly observed the collisional cooling of electrons.

B.4 Conclusion

With an anharmonicity-compensated Penning trap consists of five cylindrical electrodes, confinement property was checked. We demonstrated the pulse extraction of trapped electrons.

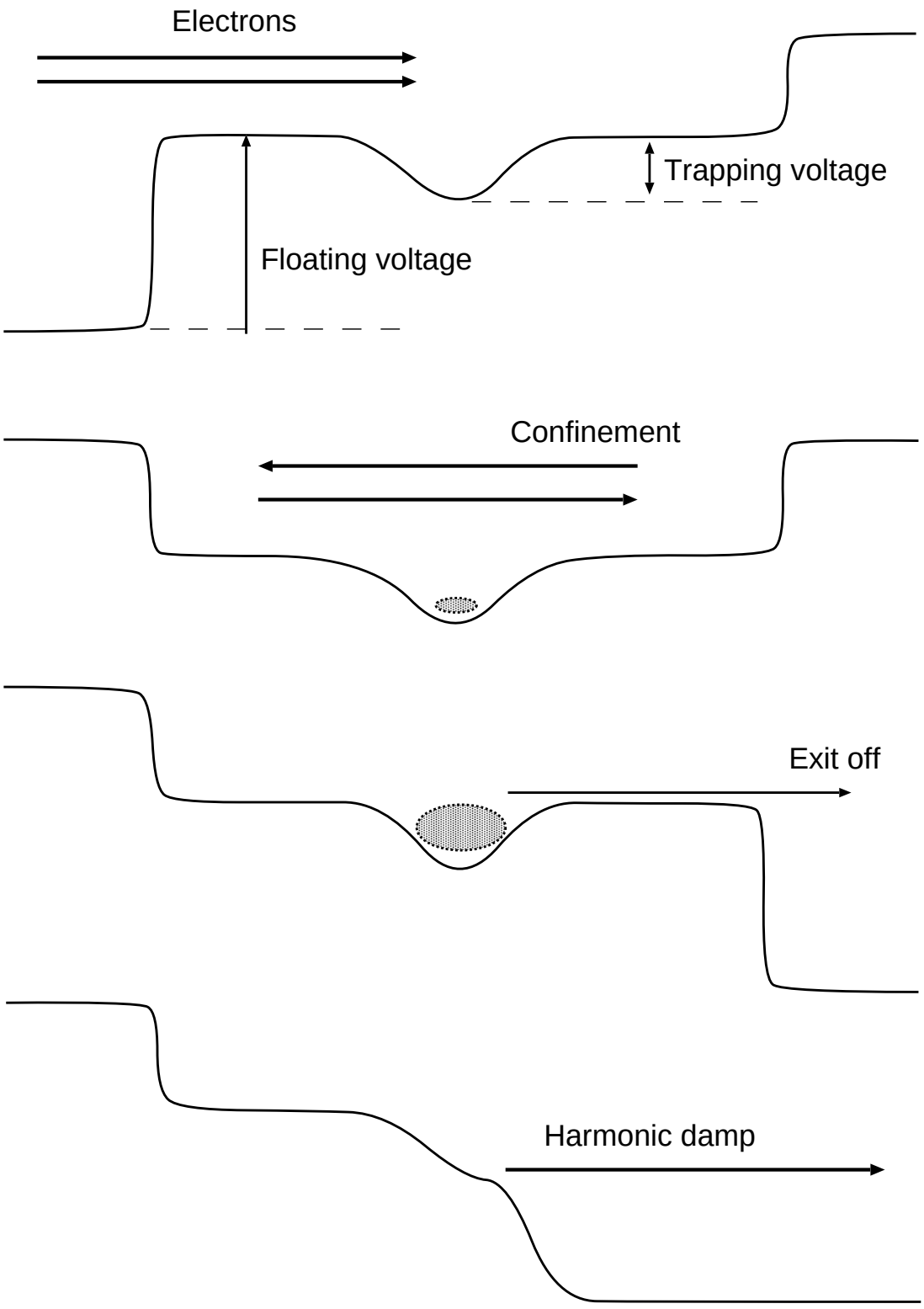

Figure B.3: Cooling of trapped electrons by collisions with residual gas.

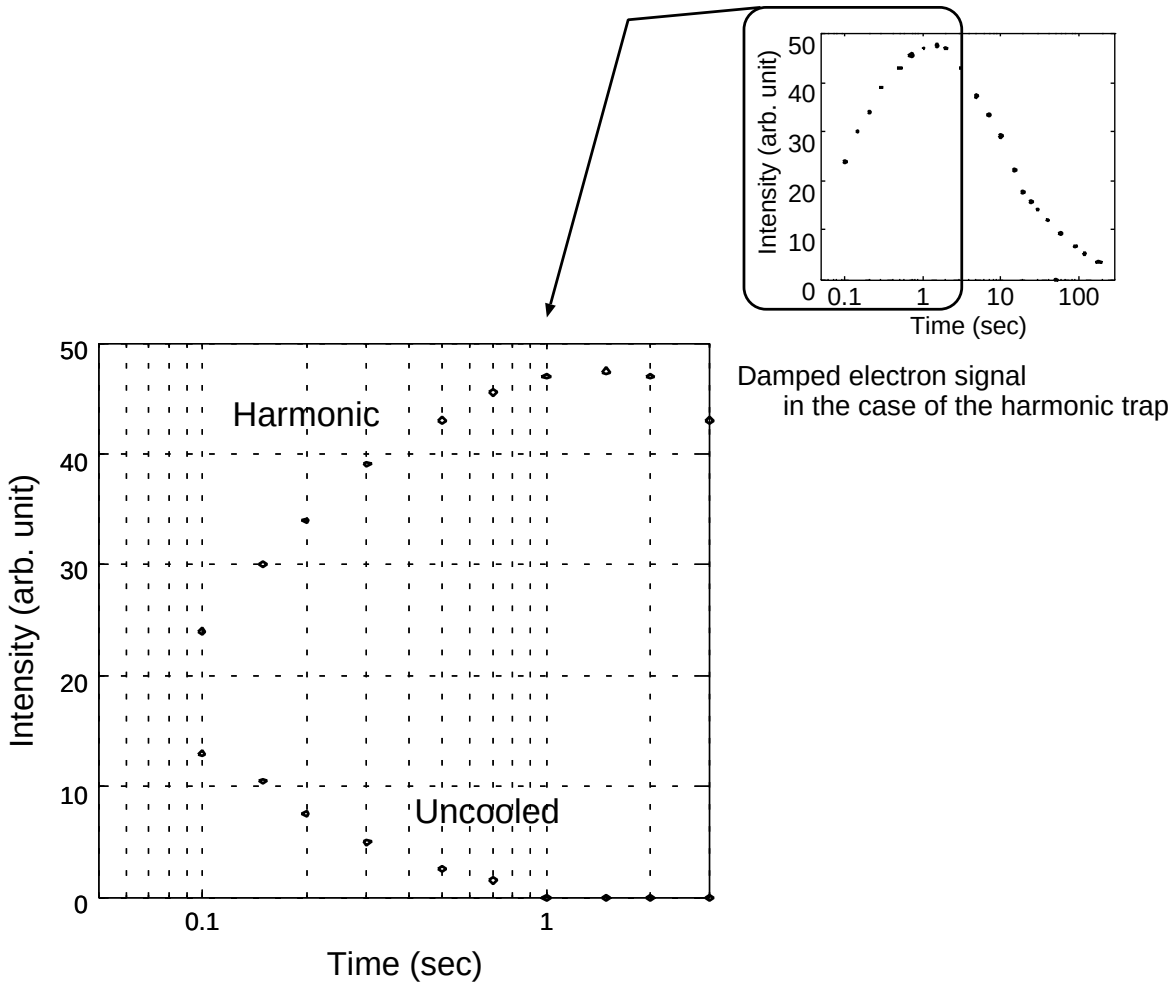

Figure B.4: Cooling of trapped electrons by collisions with residual gas.

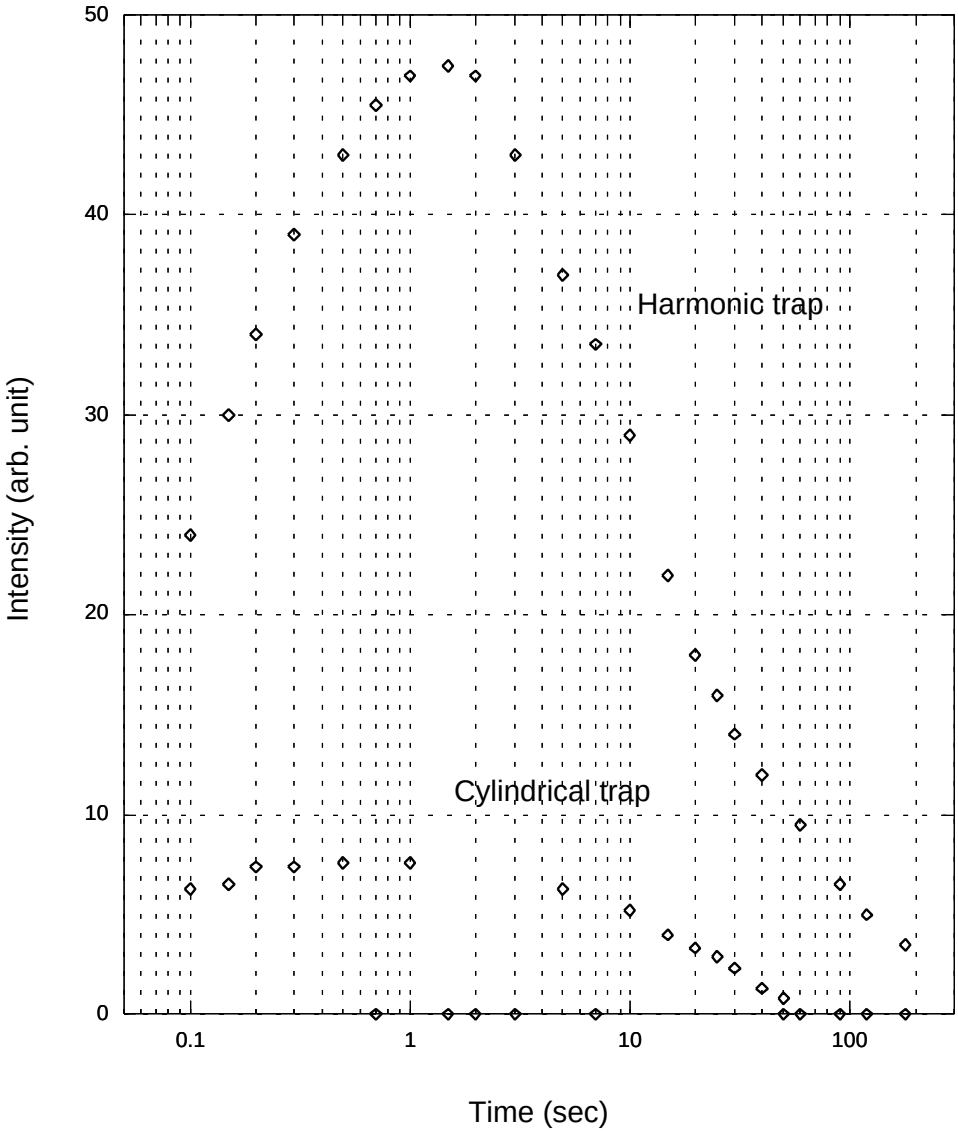

Figure B.5: Confinement of electrons in harmonic or cylindrical trap.

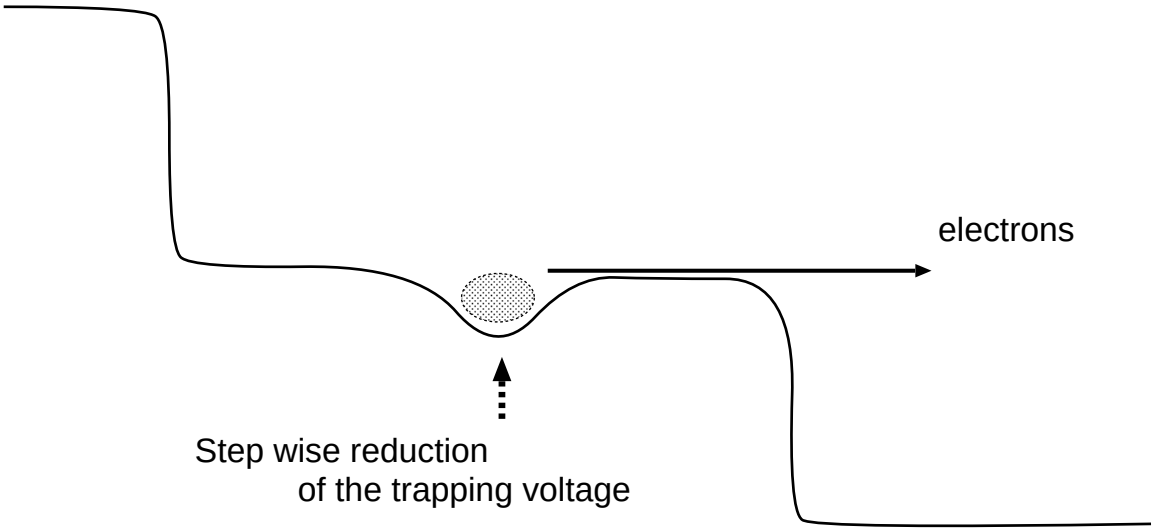

Figure B.6: Pulse extraction of trapped electrons. On top, trigger pulses for stepwise reduction of the trapping potential is shown.

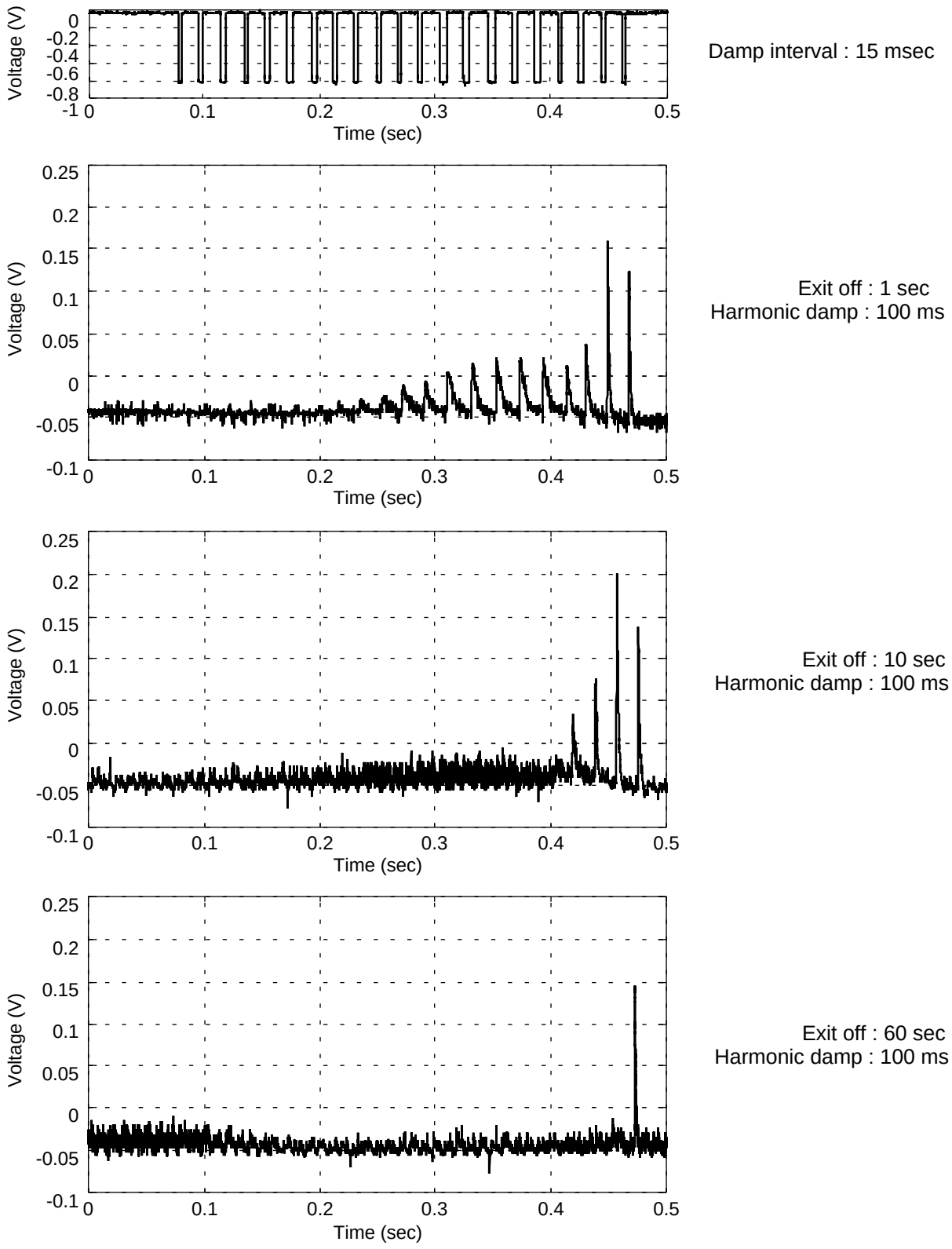

Figure B.7: Pulse extraction of trapped electrons.

Appendix C

Production of a Slow Antihydrogen Beam

Two groups working at AD on antihydrogen spectroscopy, ATHENA and ATRAP introduced in Sec.2.1 are mainly aiming experiments with trapped antihydrogen. As an alternative way to carry experiments with antihydrogen, possibility to produce antihydrogen bean is considered in this Chapter.

C.1 Current situation

⋆ 11 antihydrogen events were reported at the momentum of 2 GeV/c[21].

⋆ Now there are some proposal to make ultra-cold antihydrogens inside a trap and to catch them in a magnetic trap. In this case, antihydrogens should be colder than 1K ($\sim$ 0.1meV).

$$\Downarrow$$

There exists 10^{14} difference in between!

C.2 Why $\overline{\mathrm{H}}$ beam?

⋆ As can be seen from Fig.C.1, it is possible to do some precision measurements using atomic beam.

⋆ Concerning a neutral trap, there still exist some proplems to be solved, e.g., effects of the magnetic field gradient (which will be used to trap $\overline{\mathrm{H}}$) on charged particles in the trap.

⋆ It is easier to make antihydrogen beam than to make them almost at rest.

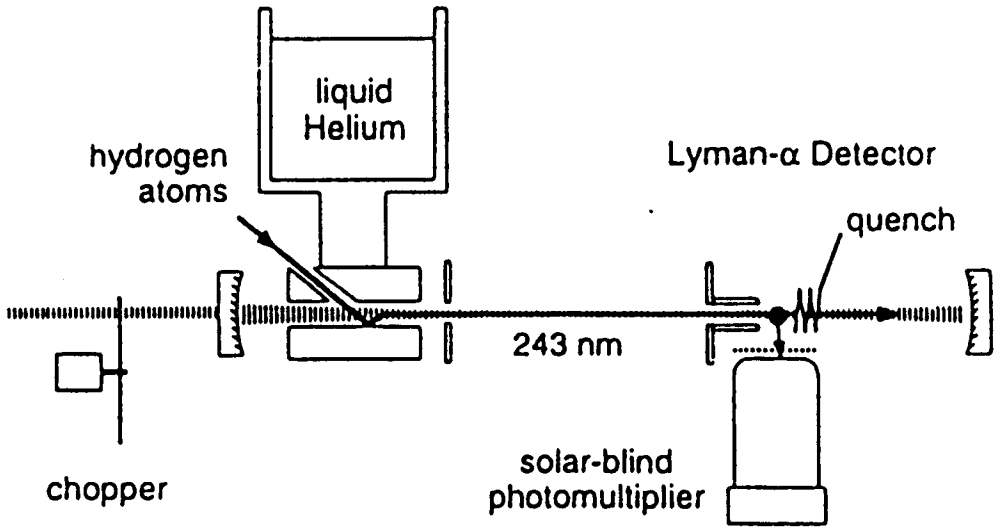

Figure C.1: Apparatus for Doppler-free two-photon spectroscopy of the hydrogen 1S-2S transition in a cold atomic beam[100].

C.3 Production scheme of 1eV $\overline{\mathrm{H}}$ beam

$$
\begin{aligned}
\mathrm{n}_{e^+} &= 10^9\,/\mathrm{cm}^3 \\
\omega_p = \left(\frac{4\pi n_{e^+} e^2}{m_{e^+}}\right)^{\frac{1}{2}} &\simeq 1.8\times 10^9\,\mathrm{Hz} \qquad (\hbar\omega_p \simeq 1\,\mu\mathrm{eV}) \\
\lambda_\mathrm{D} = \left(\frac{k_B \mathrm{T}}{4\pi n_{e^+} e^2}\right)^{\frac{1}{2}} &\simeq 1\times 10^{-3}\,\mathrm{cm} \\
\mathrm{N}_{\overline{\mathrm{p}}} &= 10^7 \\
\mathrm{E}_{\overline{\mathrm{p}}} &= 1\,\mathrm{eV} \\
v_{\overline{\mathrm{p}}} &\simeq 1.4\times 10^6\,\mathrm{cm/s} \qquad \simeq \langle v_{e^+}^2\rangle^{\frac{1}{2}}
\end{aligned}
$$

How many times we can shoot $\overline{\mathrm{p}}$ into the positron clouds?

C.4 Stopping power of 1eV antiprotons in a positron plasma

We need to know how much energy will be deposited to the positron plasma. Let us consider the stopping power of antiprotons in a positron plasma. Arguments below is based on the formalism given in a textbook by Jackson[101].

Electric field issuing from individual particle is screened out within a characteristic length, namely, the Debye length(λ_D).

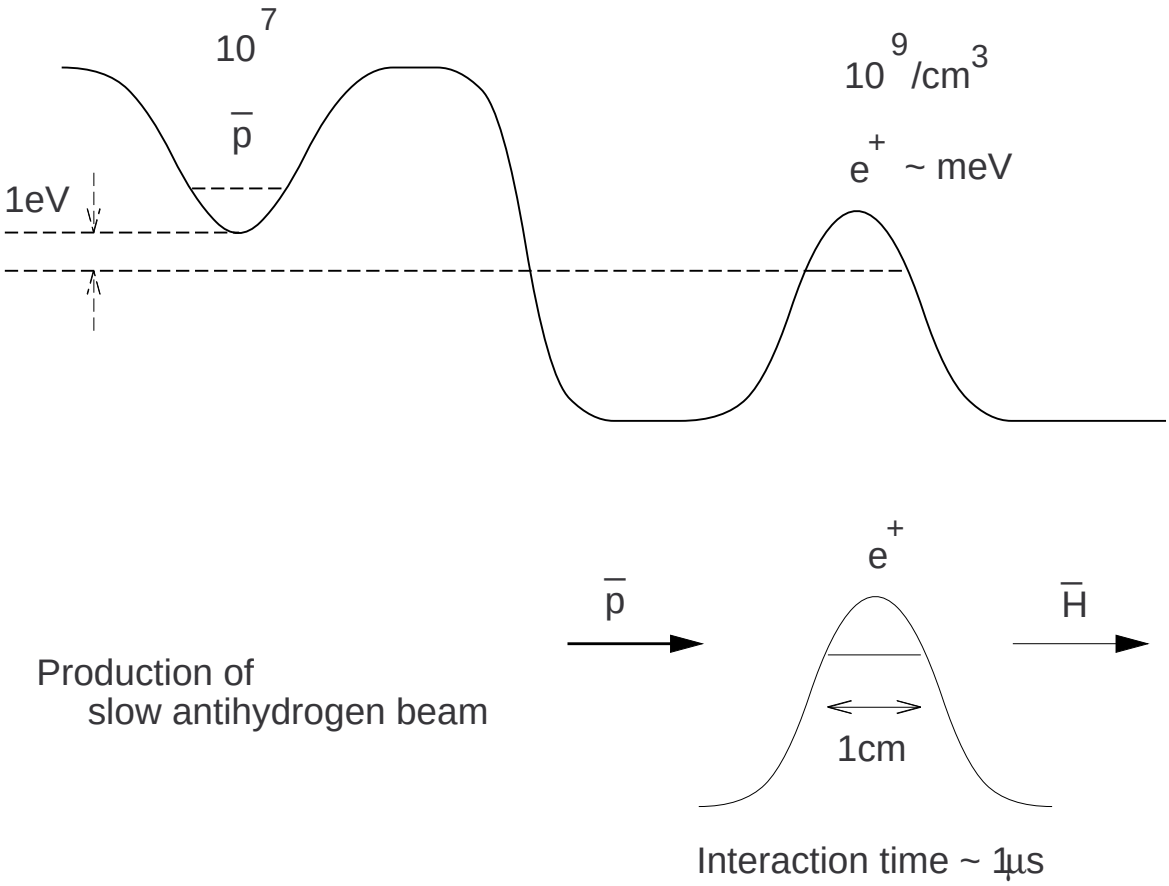

Figure C.2: Conceptual image of potentials for antihydrogen formation.

So, we may treat two regions ($\lambda_D < b$ and $b < \lambda_{\rm D}$) to calculate the energy loss.
In what follows, we use the cgs units and notations as follows :

b	=	Impact parameter
k_B	=	Boltzmann constant
e	=	Electric charge
c	=	Velocity of light
λ_D	=	Debye length of the positron plasma
ω_p	=	Plasma oscillation frequency of the positron plasma
E	=	Relative collision energy
		$\simeq$ Energy of the e^+ in the center-of-mass system
v	=	Relative velosity
		$\simeq$ Velocity of the e^+ in the center-of-mass system
E	=	Electric field caused by the incident $\overline{\rm p}$
J	=	Current density

In the region $\lambda_D < b$

♣ Excitation of collective motion
♣ Calculation using $\epsilon(\omega)$

The power done by the incident particle is

$$\frac{dE}{dt} = \int \boldsymbol{E} \cdot \boldsymbol{J} d^3x' \qquad ; \qquad \boldsymbol{J} = -e\boldsymbol{v}\delta\left(\boldsymbol{x} - \boldsymbol{x}'(t)\right) \tag{C.1}$$

$$\Delta E(b) = \int_{-\infty}^{\infty} dt \int d^3x' \boldsymbol{E} \cdot \boldsymbol{J}$$

Fourier transformation of $\boldsymbol{E}(t)$ and $\boldsymbol{x}(t)$ under the condition that x(t) and E(t) are real, gives

$$\Delta E(b) = 2e \sum_j f_j \,\mathrm{Re} \int_0^{\infty} i\omega \boldsymbol{x}_j(\omega) \cdot \boldsymbol{E}^*(\omega)\, d\omega \tag{C.2}$$

Here, '$*$' means to take complex conjugate.

We can express the sum of dipole moments in terms of the dielectric constant :

$$-e \sum_j f_j \boldsymbol{x}_j(\omega) = \frac{1}{4\pi n_e} \left(\epsilon(\omega) - 1\right) \boldsymbol{E}(\omega)$$

Hence Eq.(C.2) becomes

$$\Delta E(b) = \frac{1}{2\pi n_e} \mathrm{Re} \int_0^\infty -i\omega\epsilon(\omega) |\boldsymbol{E}(\omega)|^2 \, d\omega \tag{C.3}$$

$$\begin{aligned} \left(-\frac{dE}{dx}\right)_{a<b} &= n_e \int_a^\infty \Delta \mathrm{E}(b)\, 2\pi b db \\ &= \frac{2}{\pi} \frac{(ze)^2}{v^2} \mathrm{Re} \int_0^\infty i\omega\lambda^* a \mathrm{K}_1(\lambda^* a) \mathrm{K}_0(\lambda a) \left(\frac{1}{\epsilon(\omega)} - \beta^2\right) d\omega \end{aligned}$$

Here,

$\lambda = \dfrac{\omega^2}{v^2} - \dfrac{\omega^2}{c^2}\left(1 - \beta^2\epsilon(\omega)\right)$, $\quad \mathrm{K}_1, \mathrm{K}_0$: Modified Bessel functions of the second kind

and the quantity '$\beta \equiv \frac{v}{c}$' comes from the Fourier transformation of the electric field. In the case of non-relativistic $\overline{\mathrm{p}}$,

$$\left(-\frac{dE}{dx}\right)_{\lambda_D<b} = \frac{2}{\pi} \frac{e^2}{v^2} \mathrm{Re} \int_0^\infty \frac{i\omega}{\epsilon(\omega)} \frac{\omega\lambda_D}{v} \mathrm{K}_1\left(\frac{\omega\lambda_D}{v}\right) \mathrm{K}_0\left(\frac{\omega\lambda_D}{v}\right) d\omega \tag{C.4}$$

Suppose that

$$\epsilon(\omega) = 1 - \frac{\omega_p^2}{\omega^2 + i\omega\Gamma} \qquad (\Gamma \ll \omega_p)$$

Then,

$$\mathrm{Re}\, \frac{i\omega}{\epsilon(\omega)} = \omega_p^2 \frac{\omega^2\Gamma}{\left(\omega^2 - \omega_p^2\right) + \omega^2\Gamma^2} \tag{C.5}$$

Considering the fact that :

◦ The main contribution to the integral comes from frequencies
$\omega \simeq \omega_p$

◦ In our case, $\frac{\omega_p\lambda_D}{v} \simeq \frac{\langle v_{e^+}^2 \rangle^{\frac{1}{2}}}{v} \simeq 1$

We have

$$\left(-\frac{dE}{dx}\right)_{\lambda_D<b} \simeq \frac{0.48}{\pi} \frac{e^2}{v^2} \omega_p^2 \tag{C.6}$$

Using $v = 1.4 \times 10^6$ cm/s and $\omega_p = 1.8 \times 10^9$ Hz,

$$\begin{aligned} \left(-\frac{dE}{dx}\right)_{\lambda_D<b} &\simeq 5.8 \times 10^{-14}\, \mathrm{erg/cm} \\ &\simeq 40\, \mathrm{meV/cm} \end{aligned}$$

In the region $b < \lambda_D$

♣ Pure Coulomb interaction

♣ Two-body calculation

$$
\begin{aligned}
T &\equiv \text{energy loss per one collision} \\
&= \frac{2e^4}{m_e v^2}\,\frac{1}{b^2 + b_{\min}^2} \qquad ; \qquad b_{\min} = \frac{e^2}{\mu v^2}, \quad \mu = \text{reduced mass}
\end{aligned}
$$

$$
\begin{aligned}
\left(-\frac{dE}{dx}\right)_{b<\lambda_D} &= n_e \int_0^{\lambda_D} T\, 2\pi b db \\
&= n_e\, \frac{2\pi e^4}{m_e v^2}\, \ln \frac{\lambda_D^2 + b_{\min}^2}{b_{\min}^2}
\end{aligned}
$$

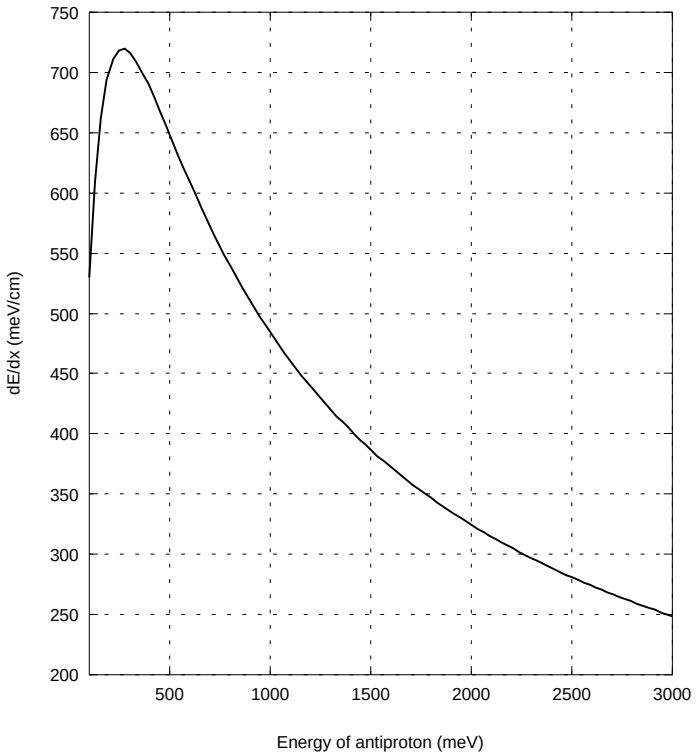

Figure C.3: Energy loss by Coulomb scattering.

For 1 eV antiproton, $b_{\min} = 1.3 \times 10^{-4}$ cm,

$$
\left(-\frac{dE}{dx}\right)_{b<\lambda_D} \simeq 480\,\text{meV/cm}
$$

C.5 Total energy transfer to the positron plasma

$$\begin{aligned}\Delta &= \mathrm{N}_{\overline{\mathrm{p}}} \left\{ \left(-\frac{dE}{dx}\right)_{\lambda_D<b} + \left(-\frac{dE}{dx}\right)_{b<\lambda_D} \right\} \cdot 1\mathrm{cm} \\ &\simeq 5.2 \times 10^6 \mathrm{eV}\end{aligned}$$

Since we have $10^9\, e^+$, energy given to one e^+ is

$$\delta = 5.2 \times 10^{-3}\mathrm{eV} \simeq 5\mathrm{meV}$$

C.5.1 Cooling rate by synchrotron radiation

The energy given to the positron plasma should be carried away by synchrotron radiation.

In the case of positron, we have

$$\frac{\mathrm{T}}{\mathrm{T}_0} = exp\left\{-3.9 \times 10^{-9}\mathrm{B}^2 t\right\}$$

Time needed to lose half of its energy by radiation:

$$\tau \simeq 1.7\,\mathrm{sec} \simeq 2\,\mathrm{sec} \qquad \text{for B } = 10000\,\mathrm{Gauss}$$

C.6 Angular straggling due to collisions

If we use the fact that $\frac{d\sigma}{d\Omega} \propto \sin^{-4}\left(\frac{\theta}{2}\right)$, we can also estimate the angular straggling.

$$\begin{aligned}\langle\theta^2\rangle &= \frac{\int \theta^2 \frac{d\sigma}{d\Omega}\, d\Omega}{\int \frac{d\sigma}{d\Omega}\, d\Omega} = \frac{\int_{\theta_{min}}^{\theta_{max}} \theta^2 \frac{\cos\left(\frac{\theta}{2}\right)}{\sin^3\left(\frac{\theta}{2}\right)}\, d\theta}{\int_{\theta_{min}}^{\theta_{max}} \frac{\cos\left(\frac{\theta}{2}\right)}{\sin^3\left(\frac{\theta}{2}\right)}\, d\theta} \\ &\simeq 2\theta_{min}^2 \ln\frac{\theta_{max}}{\theta_{min}} \qquad (\theta \ll 1)\end{aligned}$$

Since the scattering angle is related with the impact parameter as

$$\tan\frac{\theta}{2} = \frac{e^2}{2E} \cdot \frac{1}{b}$$

(can be derived by considering the momentum transfer at one collision),

$$\begin{aligned}\theta_{min} &= \theta|_{b=b_{max}=\lambda_D} = 1.4\times10^{-4}\,\mathrm{rad}\\ \theta_{max} &= \theta|_{b=b_{min}} = 1.1\times10^{-3}\,\mathrm{rad}\end{aligned}$$

It becomes that

$$\begin{aligned}(\Delta\theta)^2 &= \langle\theta^2\rangle - \langle\theta\rangle^2\\ &= \langle\theta^2\rangle\\ &= 8.2\times10^{-8}\end{aligned}$$

Total angular deflection is given by

$$\begin{aligned}\langle\Theta^2\rangle &= n_{e^+}\sigma\Delta x\Delta\theta\\ &= 10^9\cdot1.4\times10^{-6}\cdot1\cdot8.2\times10^{-8}\\ &\simeq 1.1\times10^{-4}\end{aligned}$$

here was used the value

$$\begin{aligned}\sigma &= \int\frac{d\sigma}{d\Omega}\,d\Omega\\ &= \int_{\theta_{min}}^{\theta_{max}}\sin\theta d\theta\int_0^{2\pi}d\phi\left(\frac{e^2}{2m_{\overline{\mathrm{p}}}v_{\overline{\mathrm{p}}}}\right)^2\frac{1}{\sin^4\frac{\theta}{2}}\\ &\simeq 1.4\times10^{-6}\,\mathrm{cm}^2\end{aligned}$$

Therefore,

$$\begin{aligned}\Delta\Theta &\equiv (\langle\Theta^2\rangle)^{\frac{1}{2}}\\ &\simeq 0.01\mathrm{rad}\\ &= 10\mathrm{mrad}\end{aligned}$$

In these calculations, are <u>not</u> included :

♠ Velocity change (slowing down) during one passage (According to this, energy loss can be larger.)

♠ Existence of B-field (Effect of magnetization *etc.*)

♠ Velocity distribution of positrons

♠ Possibility of instabilities (Can be possibly avoided)

♠ Effect of the trapping potential

C.7 Estimation of $\overline{\mathrm{H}}$ production rate

Here we consider only the spontaneous radiative recombination rate.
The cross section is given by

$$\sigma_{RR} = \frac{E \ln\left(\frac{E}{E_e}\right)}{E_e}$$

where E_e is the energy of the electron, and the recombination rate $\Gamma = \sigma_{RR} v$ is given in Fig.C.4.

Now, recalling that the interaction time is $1\,\mu$sec, we have a number for the production rate of antihydrogen :

$$\begin{aligned} \mathrm{N}_{\overline{\mathrm{H}}} &= \mathrm{N}_{\overline{\mathrm{p}}} \cdot n_{e^+} \cdot \Gamma \cdot t \\ &= 10^7 \cdot 10^9 \cdot 0.1 \times 10^{-9} \cdot 10^{-6} \\ &= 1\,/\text{passage} \end{aligned}$$

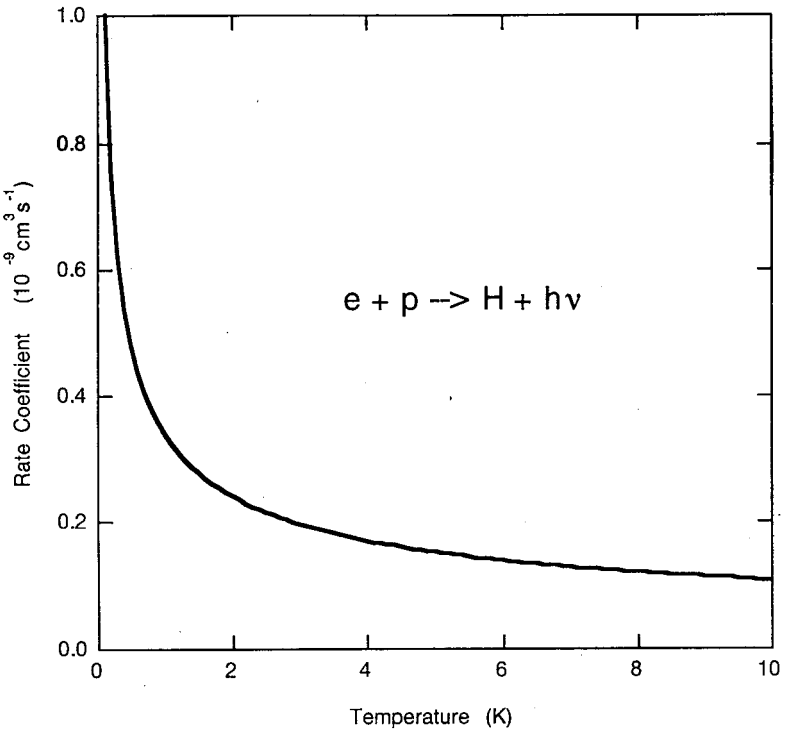

Figure C.4: Rate coefficient for $e^+ + \overline{\mathrm{p}} \rightarrow \overline{\mathrm{H}} + \hbar\nu$. Γ is defined as $\Gamma = \sigma_{RR} v$ and T corresponds to relative collision energy.

C.8 Summary

Supposing 10^7 $\overline{\mathrm{p}}$ s interacts with a positron plasma ($n_{e^+} = 10^9\,/\mathrm{cm}^3$)

* By simple calculation , we have

$$\Delta \simeq 5 \times 10^6 \mathrm{eV}$$

as a total energy loss, which corresponds to energy gain per one positron :

$$\delta \simeq 5\mathrm{meV}$$

* On the other hand, for a positron, time needed to lose half of its energy by radiation is given by

$$\tau \simeq 2\,\mathrm{sec} \qquad \text{for B } = 10000\,\mathrm{Gauss}$$

* Angular straggling due to collisions becomes

$$\Delta\Theta \simeq 10\,\mathrm{mrad}\ /\mathrm{passage}$$

* Antihydrogen production rate is

$$\mathrm{N}_{\overline{\mathrm{H}}} \simeq 1\,/\mathrm{passage}$$

Appendix D

Notations

- Mass of particles

$$m_e = 9.11 \times 10^{-31} \quad [\text{kg}] \quad \text{electron} \tag{D.1}$$
$$m_p = 1.67 \times 10^{-27} \quad [\text{kg}] \quad \text{proton} \tag{D.2}$$

- Permeability of vacuum

$$\epsilon_0 = 8.85 \times 10^{-12} \quad [\text{FK}^{-1}] \tag{D.3}$$

- Boltzmann constant

$$k_B = 1.38 \times 10^{-23} \quad [\text{JK}^{-1}] \tag{D.4}$$

- Bohr magneton

$$\mu_B \equiv \frac{e\hbar}{2m_e c} = 9.27 \times 10^{-24} \quad [\text{JT}^{-1}] \tag{D.5}$$

- Magnetic moment

$$\mu = g\mu_B S \tag{D.6}$$

Appendix E

Useful Formulae

E.1 Single Particle Motions

1. Cyclotron frequency

   For an electron,

$$\omega_{ce}[\mathrm{s}^{-1}] = \frac{eB}{m_e} = 1.76 \times 10^{11} B[\mathrm{T}] \tag{E.1}$$

   For a proton,

$$\omega_{cp}[\mathrm{s}^{-1}] = \frac{eB}{m_p} = 9.58 \times 10^{7} B[\mathrm{T}] \tag{E.2}$$

2. Larmor radius

$$r_L[\mathrm{m}] = \frac{v_{perp}}{\omega_c} = \frac{mv_\perp}{qB} \tag{E.3}$$

3. Thermal velocity

$$v_{th,e}[\mathrm{m} \cdot \mathrm{s}^{-1}] = \left(\frac{k_B T_e}{m_e}\right)^{\frac{1}{2}} = 3.89 \times 10^{3} (T_e[\mathrm{K}])^{\frac{1}{2}} \tag{E.4}$$

$$v_{th,p}[\mathrm{m} \cdot \mathrm{s}^{-1}] = \left(\frac{k_B T_p}{m_p}\right)^{\frac{1}{2}} = 9.09 \times 10^{1} (T_p[\mathrm{K}])^{\frac{1}{2}} \tag{E.5}$$

E.2 (Nonneutral) Plasmas

1. Plasma frequency

$$\omega_{pe}[\mathrm{Hz}] = \left(\frac{ne^2}{\epsilon_0 m_e}\right)^{\frac{1}{2}} \tag{E.6}$$

2. Debye length

$$\lambda_D[\mathrm{m}] = \left(\frac{\epsilon_0 k_B T}{ne^2}\right)^{\frac{1}{2}} = 69\left(\frac{T[\mathrm{K}]}{n}\right)^{\frac{1}{2}} \tag{E.7}$$

3. Thermal de Broglie length

$$\lambda_{th}[\mathrm{m}] = \frac{h}{mv_{th}} \tag{E.8}$$

E.3 Miscellaneous

1. Relation between density (n) and pressure (p)

   Supposing ideal gas of temperature 0°C,

$$n[\mathrm{cm}^{-3}] = 3.5 \times 10^{16} p[\mathrm{Torr}]. \tag{E.9}$$

Bibliography

[1] Chamberlain O., Segrè E., Wiegand C., and Ypsilantis T. Observation of antiprotons. *Phys. Rev.*, 100:947–950, 1955.

[2] Cork B., Lambertson G. R., Piccioni O., and Wenzel W. A. Antineutrons produced from antiprotons in charge-exchange collisions. *Phys. Rev.*, 104:1194–1197, 1956.

[3] Dorfan D. E., Eades J., Lederman L. M., Lee W., and Ting C. C. Observation of antideuterons. *Phys. Rev. Lett.*, 1965.

[4] Chamberlain O., Keller D. V., Mermod R., Segrè E., Steiner H. M., and Ypsilantis T. Experiments on antiprotons : Antiproton-nucleon cross sections. *Phys.Rev.*, 108:1553–1556, 1957.

[5] CPLEAR Collabolation Angelopoulos A., *et al.* First direct observation of time-reversal non-invariance in the neutral-kaon system. *Phys. Lett. B*, 444:43–51, 1998.

[6] Gabrielse G., Khabbaz A., Hall D. S., Heimann C., Kalinowsky H., Jhe W. Precision mass spectroscopy of the antiproton and proton using simultaneously trapped particles. *Phys. Rev. Lett.*, 82:3198 – 3210, 1999.

[7] Gabrielse G. *et al.* First capture of antiprotons in a Penning trap: A kiloelectronvolt sourse. *Phys. Rev. Lett.*, 57:2504–2507, 1986.

[8] Gabrielse G. *et al.* Cooling and slowing of trapped antiprotons below 100mev. *Phys. Rev. Lett.*, 63:1360–1363, 1989.

[9] Holzscheiter M. H. The PS200 catching trap: A new tool for ultralow-energy antiproton physics. *Physics of Atomic Nuclei*, 57:1799–1809, 1994.

[10] Holzscheiter M. H., *et al.* Are antiprotons forever? *Phys. Lett. A*, 214:279–284, 1996.

[11] Ichioka T. An attempt to extract ultracold antiprotons from a Penning trap – As a first step towards the research of initial capturing process of antiprotons into atoms and/or molecules –. Master's thesis, University of Tokyo, 1996.

[12] Knudsen H. and Reading J. F. Ionization of atoms by particle and antiparticle impact. *Phys. Rep.*, 212:107–222, 1992.

[13] Hvelplund P., *et al.* Ionization of helium and molecular hydrogen by slow antiprotons. *J. Phys. B*, 27:925, 1994.

[14] Khayyat Kh., *et al.* Differential cross sections in antiproton - and proton - helium collisions. *J. Phys. B*, 32:L73–, 1999.

[15] Andersen L. H., *et al.* Single and double ionization of helium by fast protons and antiprotons. *Phys. Rev. Lett.*, 57:2147–2150, 1986.

[16] Andersen L. H., *et al.* Multiple ionization of He,Ne,and Ar by fast and slow antiprotons. *Phys. Rev. A*, 36:3612, 1987.

[17] Andersen L. H., *et al.* Further studies of double ionization of He, Ne, and Ar by fast and slow antiprotons. *Phys. Rev. A*, 40:7366, 1989.

[18] Yamazaki Y., *et al.* Measurements of electron spectra in the forward direction in slow-antiproton carbon-foil collisions. *J. Phys. Soc. Japan*, 59(8):2643, 1990.

[19] Nakamura S. N., *et al.* Delayed annihilation of antiprotons in helium gas. *Phys. Rev. A*, 49(6):4457–4465, 1994.

[20] Torii H. A., *et al.* High-precision laser measurements of the density shifts of resonance lines in antiprotonic helium atoms and stringent constraint on the antiproton charge and mass. *Phys. Rev. A*, 1999.

[21] Baur G., *et al.* Production of antihydrogen. *Phys. Lett. B*, 368:251–258, 1996.

[22] Trivelpiece A. W., Pechacek R. E., and Kapetanakos C. A. Trapping of a 0.5-mev electron ring in a 15-kg pulsed magnetic mirror field. *Phys. Rev. Lett.*, 21:1436–1438, 1968.

[23] Davidson R. C. and Krall N. S. Vlasov description of an electron gas in a magnetic field. *Phys. Rev. Lett.*, 22:833–837, 1969.

[24] Bogema, Jr. B. L. and Davidson R. C. Rotor equilibria of non-neutral plasmas. *Phys. Fluids*, 13:2772–2778, 1970.

[25] Daniel H. E. Dubin. Theory of electrostatic fluid modes in a cold spheroidal non-neutral plasma. *Phys. Rev. Lett.*, 66:2076–2079, 1991.

[26] Dubin D. H. and Schiffer J. P. Normal modes of cold confined one-component plasmas. *Phys. Rev. E*, 53:5249–5267, 1996.

[27] Bollinger J. J. *et al.* Electrostatic modes of ion-trap plasmas. *Phys. Rev. A*, 48:525–545, 1993.

[28] Malmberg J. H. and O'Neil T. M. Pure electron plasma, liquid, and crystal. *Phys. Rev. Lett.*, 39:1333–1336, 1977.

[29] Malmberg J. H. and Driscoll C. F. Long-time containment of a pure electron plasma. *Phys. Rev. Lett.*, 44:654–657, 1980.

[30] Surko C. M., Leventhal M., and Passner A. Positron plasma in the laboratory. *Phys. Rev. Lett.*, 62:901–904, 1989.

[31] Surko C. M. and Murphy T. J. Use of the positron as a plasma particle. *Phys. Fluids B*, 2:1372–1375, 1990.

[32] Bollinger J. J. and Wineland D. J. Strongly coupled nonneutral ion plasma. *Phys. Rev. Lett.*, 53:348–351, 1984.

[33] Brewer L. R., Prestage J. D., Bollinger J. J., Itano W. M., Larson D. J., and Wineland D. J. Static properties of a non-neutral $^9be^+$-ion plasma. *Phys. Rev. A*, 38:859–873, 1988.

[34] Driscoll C. F. and Malmberg J. H. Length-dependent containment of a pure electron-plasma column. *Phys. Rev. Lett.*, 50:167–170, 1983.

[35] Fajans J. Lifetime scaling in non-neutral plasmas. *Comm. on Modern Phys.*, 1:123, 1999.

[36] Tinkle M. D., Greaves R. G., Surko C. M., Spencer R. L., Mason G. W. Low-order modes as diagnostics of spheroidal non-neutral plasmas. *Phys. Rev. Lett.*, 72:352–355, 1994.

[37] Weimer C. S., Bollinger J. J., Moore F. L., Wineland D. J. Electrostatic modes as a diagnostic in penning-trap experiments. *Phys. Rev. A*, 49:3842–3853, 1994.

[38] Higaki H. Wall and temperature effects on electrostatic oscillations of spheroidal non-neutral electron plasmas in the multi-ring electrode trap. *Jpn. J. Appl. Phys.*, 36:5300–5305, 1997.

[39] Baird S., *et al.* Design study of the antiproton decelerator: Ad. Technical Report CERN/PS 96-43 (AR), CERN, 1996. Edited by Maury S.

[40] Edited by Wilson E. J. N. Design study of an antiproton collector for the antiproton accumulator(ACOL). Technical Report CERN 83-10, CERN, 1983.

[41] Azuma T., *et al.* Atomic spectroscopy and collisions using slow antiprotons. Technical Report 97-19, CERN/SPSC, 1997.

[42] Yamazaki Y. Production of ultra slow antiprotons, its application to atomic collisions and atomic spectroscopy - ASACUSA project. *NIM B*, 154:174 – 184, 1999.

[43] Yamazaki Y. Trapping, cooling and extraction of cooled antiprotons, and the asacusa project. In Bollinger J. J., *et al.*, editor, *Non-neutral Plasma Physics III*, volume CP498, pages 48–58. AIP, 1999.

[44] Batty C. J. Exotic atoms. *Sov. J. Part. Nucl.*, 1982.

[45] Cohen J. S. and Padial N. T. Initial distributions, cascade, and annihilation of $\overline{\mathrm{p}}\mathrm{p}$ atoms formed in $\overline{\mathrm{p}} + \mathrm{H}^-$ collisions in near vacuum. *Phys. Rev. A*, 41:3460–3468, 1990.

[46] Cohen J. S. Molecular effects on antiproton capture by H_2 and the states of $\overline{\mathrm{p}}\mathrm{p}$ formed. *Phys. Rev. A*, 56:3583–3596, 1997.

[47] Cohen J. S. Multielectron effects in capture of antiprotons and muons by helium and neon. *Phys. Rev. A*, 62, 2000.

[48] Knudsen H. and Reading J. F. Ionization of atoms by particle and antiparticle impact. *Phys. Reports*, 212:107–222, 1992.

[49] Bosser J. *et al.* Feasibility study of a decelerator radio frequency quadrupole system for the antiproton decelerator ad. Technical Report PS/HP Note 97-36, CERN, 1997.

[50] Lombardi A. Private communication.

[51] Theiss A. J., Mahaffey R. A., Trivelpiece A. W. Rigid-rotor equilibria of nonneutral plasmas. *Phys. Rev. Lett.*, 35:1436–1438, 1975.

[52] Davidson Ronald C. *Physics of Nonneutral Plasmas*. Addson-Wesley, 1990.

[53] Larson D. J., Bergquist J. C., Bollinger J. J., Itano Wayne M., and Wineland D. J. Sympathatic cooling of trapped ions: A laser-cooled two-species nonneutral ion plasma. *Phys. Rev. Lett.*, 57:70–73, 1986.

[54] Imajo H., Hayasaka K., Ohmukai R., Tanaka U., Watanabe M., and Urabe S. Spatial separation of ion clouds between sympathatically laser-cooled Cd^+-ion isotopes. *Phys. Rev. A*, 55:1276–1280, 1997.

[55] Brillouin L. A theorem of Larmor and its importance for electrons in magnetic fields. *Phys. Rev.*, 67:260–266, 1945.

[56] Greaves R. G., Tinkle M. D., Surko C. M. Modes of a pure ion plasma at the brillouin limit. *Phys. Rev. Lett.*, 74:90–93, 1995.

[57] Trivelpiece A. W. and Gould R. W. Space charge waves in cylindrical plasma columns. *J. Appl. Phys.*, 30:1784–1793, 1959.

[58] Mohri A., Higaki H., Tanaka H., Yamazawa Y., Aoyagi M., Yuyama T., and Michishita T. Confinement of nonneutral spheroidal plasmas in multi-ring electrode traps. *Jpn. J. Appl. Phys.*, 37:664–670, 1998.

[59] Yamazawa Y., Michishita T., and Mohri A. Damping of diocotron oscillation in a nonneutral electron plasma by excited axisymmetric electrostatic wave. *Jpn. J. Appl. Phys.*, 36:L1612–L1615, 1997.

[60] Kiwamoto Y., Mohri A., Ito K., Sanpei A., and Yuyama T. 2-D interaction of discrete electron vortices. In Bollinger J. J., *et al.*, editor, *Non-neutral Plasma Physics III*, volume CP498, pages 99–105. AIP, 1999.

[61] Kiwamoto Y., Ito K., Sanpei A., Mohri A., Yuyama T., Michishita T. Accelerated merging of electron vortices in background vorticity. *J. Phys. Soc. Jpn.*, 68:3766–3769, 1999.

[62] Kiwamoto Y., Ito K., Sanpei A., and Mohri A. Dynamics of electron-plasma vortex in background vorticity distributions. *Phys. Rev. Lett.*, 85:3173–3176, 2000.

[63] Oshima N., Kambara T., Kanai Y., Kojima T. M., Nakai Y., Oyama H., Yamazaki Y. A new project to produce ultra cold ions using a positron cooling technique. In *Proceedings of the International Workshop on Advanced Techniques of Positron Beam Generation and Control*, 1998.

[64] Huang X.-P, Anderegg F., Hollmann E.M., Driscoll C.F. and O'Neil T.M. Steady-state confinement of non-neutral plasmas by rotating electric fields. *Phys. Rev. Lett.*, 78:875–878, 1997.

[65] Anderegg F., Hollmann E.M., and Driscoll C.F. Rotating field confinement of pure electron plasmas using trivelpiece-gould modes. *Phys. Rev. Lett.*, 81:4875–4878, 1998.

[66] Gabrielse G. *et al.* Open-endcap Penning traps for high precision experiments. *Int. J. Mass Spectrom. and Ion Processes*, 88:319–332, 1989.

[67] Keinigs R. Effect of magnetic field errors on low-frequency waves in a pure electron plasma. *Phys. Fluids*, 24(5):860–863, 1981.

[68] Keinigs R. Field-error induced transport in a pure electron plasma column. *Phys. Fluids*, 27(6):1427–1433, 1984.

[69] Notte J. and Fajans J. The effect of asymmetries on non-neutral plasma confinement time. *Phys. Plasmas*, 1:1123–1127, 1994.

[70] Yu J., Desaintfuscien J. and Plumelle F. Ion density limitation in a penning trap due to the combined effect of asymmetry and space charge. *Appl. Phys. B*, 48:51–54, 1989.

[71] Yoshiki Franzén K. Private communication.

[72] Gilbert S. J., Greaves R. G., and Surko C. M. Positron scattering from atoms and molecules at low energies. *Phys. Rev. Lett.*, 82:5032–5035, 1999.

[73] Lyman Spitzer, Jr. . *Physics of Fully Ionized Gases*. Interscience Publishers Ltd., London, 1956.

[74] O'Neil T. M. Centrifugal separation of a multispecies pure ion plasma. *Phys. Fluids*, 24:1447–1451, 1981.

[75] Totsuji H. Two-dimensional system of charges in cylindrical traps. *Phys. Rev. E*, 47:3784–3786, 1993.

[76] Totsuji H., Tsuruta K., Totsuji C., Nakano K., Kamon K., and Kishimoto T. Two-component nonequilibrium nonneutral plasma in penning-malmberg trap. In Bollinger J. J., *et al.*, editor, *Non-Neutral Plasma Physics III*, pages 77–82. AIP, 1999.

[77] Spindt C. A., *et al.* Field-emitter arrays for vacuum microelectronics. *IEEE Trans. on Elec. Dev.*, 38:2355–2363, 1991.

[78] Tanaka H., Sodekoda T., Maekawa T., Yamaguchi S., Asakawa M., and Terumichi Y. Production of pure electron plasmas using a field emitter array. *Jpn. J. Appl. Phys.*, 39:602–606, 2000.

[79] Kriesel J. M. and Driscoll C. F. Two regimes of asymmetry-induced tranport in non-neutral plasmas. *Phys. Rev. Lett.*, 85:2510–2513, 2000.

[80] Wineland D. J., and Dehmelt H. G. Principles of the stored ion calorimeter. *J. Appl. Phys.*, 46:919–930, 1975.

[81] Feng X., Charlton M., Holzsceiter M., Lewis R. A., and Yamazaki Y. Tank circuit model applied to particles in a Penning trap. *J. Appl. Phys.*, 79(1):8–13, 1996.

[82] Hollmann E. M., Anderegg F., Driscoll C. F. Confinement and manipulation of non-neutral plasmas using rotating wall electric fields. *Phys. Plasmas*, 7:2776–2789, 2000.

[83] Greaves R. G. and Surko C. M. Inward tranport and compression of a positron plasma by a rotating electric field. *Phys. Rev. Lett.*, 85:1883–1886, 2000.

[84] Ichioka T., Higaki H., Hori M., Oshima N., Kuroki K., Mohri A., Komaki K. and Yamazaki Y. Multi-ring trap as a reservoir of cooled antiprotons. In Bollinger J. J., *et al.*, editor, *Non-neutral Plasma Physics III*, volume CP498, pages 59–64. AIP, 1999.

[85] Pollock R. E., Ellsworth J., Muterspaugh M. W., and Todd D. S. Proton beam-electron plasma interactions. In Bollinger J. J., *et al.*, editor, *Non-Neutral Plasma Physics III*, pages 336–344. AIP, 1999.

[86] Tabata T., and Shirai T. Analytic cross sections for collisions of H^+, H_2^+, H_3^+, H, H_2, and H^- with hydrogen molecules. *Atomic Data and Nuclear Data Tables*, 76, 2000.

[87] Nakai Y., Shirai T., Tabata T., and Ito R. Cross sections for charge transfer of hydrogen atoms and ions colliding with gaseous atoms and molecules. *Atomic Data and Nuclear Data Tables*, 37, 1987.

[88] Risley J. S., Geballe R. Absolute H^- detachment cross sections. *Phys. Rev. A*, 9:2485–2495, 1974.

[89] Beck B. R., Fajans, J., Malmberg J. H. Temperature and anisotropic-temperature relaxation measurements in cold, pure-electron plasmas. *Phys. Plasmas*, 3:1250–1258, 1996.

[90] Church D. A. Collision measurements and excited-level lifetime measurements on ions stored in paul, penning and kingdon ion traps. *Physics Reports*, 228:253 – 358, 1993.

[91] Van Dyck, Jr. R. S., Schwinberg P. B., Dehmelt H. G. Electron magnetic moment from geonium spectra: Early experiments and background concepts. *Phys. Rev. D*, 34:722 – 736, 1986.

[92] Werth G. Hyperfine structure and f-factor measurements in ion traps. *Physica Scripta*, T59:206 – 210, 1995.

[93] Schauer M. M., Mitchell T. B., and Holzscheiter M. H. Electron penning trap for the generation of high density non-neutral plasmas. *Rev. Sci. Instrum.*, 68:3340–3345, 1997.

[94] Byrne J., *et al.* Measurement of the neutron lifetime by counting trapped protons. *Phys.Rev.Lett.*, 65:289 – 292, 1990.

[95] Pradip K. Ghosh. *Ion Traps*. International Series of Monographs on Physics. Oxford Science Publications, 1995.

[96] Penning F. M. Die Glimmentladung bei niedrigem druck zwischen koaxialen Zylindern in einem axialen Magnetfeld. *Physica*, III, 1936. In German, with summary in English.

[97] Brown L. S. and Gabrielse G. Geonium theory: Physics of a single electron or ion in a Penning trap. *Rev. of Mod. Phys.*, 58:233 – 311, 1986.

[98] Gabrielse G. and Mackintosh F.C. Cylindrical Penning traps with orthogonalized anharmonicity compensation. *Int. J. Mass Spectrom. and Ion Processes*, 57:1 – 17, 1984.

[99] Shimamura I. Cross sections for collisions of electrons with atoms and molecules. *Scientific Papers of the Institute of Physical and Chemical Research*, 82:1–51, 1989.

[100] Hänsch T. W. and Zimmermann C. Laser spectroscopy of hydrogen and antihydrogen. *Hyp. Int.*, 76:47–57, 1993.

[101] Jackson J. D. *Classical Electrodynamics*. John Wiley & Sons,Inc., third edition, 1999. Chapter 13.